

https://dspace.org/

Defect–engineered lithium titanate anode materials for lithium–ion batteries

Podile, Seromo

2023-10

University of the Witwatersrand, Johannesburg

https://hdl.handle.net/10539/42448

Podile, Seromo. (2023). Defect–engineered lithium titanate anode materials for lithium–ion batteries. [Master's dissertation, University of the Witwatersrand, Johannesburg]. https://hdl.handle.net/10539/42448

Downloaded from a DSpace repository. https://dspace.org/

Defect–engineered lithium titanate anode materials for lithium–ion batteries



UNIVERSITY OF THE
WITWATERSRAND,
JOHANNESBURG

Seromo Podile

A dissertation submitted to the Faculty of Science, University of the Witwatersrand, Johannesburg, in fulfilment of the requirements for the degree of

Master of Science in Chemistry

Supervisor: Prof. Kenneth I. Ozoemena

in Johannesburg

DECLARATION

I solemnly declare that the dissertation, which is hereby submitted at the University of the Witwatersrand, Johannesburg for the Degree of Master of Science is self-reliant, independently studied and has not been submitted before to any other institution of higher learning for examination.



(Signed) Seromo Podile

_____16_____day of

_____October_____20___23_____at____Johannesburg_____

DEDICATION

This work is dedicated to my family. To my mother, Gladys Matlhodi Podile, who spent most of my life being a single mother, molding my life and allowing my curiosity and exploration to take place. To my late father, Elvis Podile, with whom I did not spend much time, but who played an elemental role in the legacy I aim to build. To my siblings, for their unwavering support of my dreams.

A dedication to the kids who aspire to become scientists and have a role in making the world a better place.

ACKNOWLEDGEMENTS

To Prof. Kenneth Ikechukwu Ozoemena, I am delighted to express my heartfelt appreciation for your extensive help and insistence that I embark on the journey of this project, regardless of the funding challenges and delays we experienced. Thank you for offering your time, sharing your immense knowledge and wisdom, and, most importantly, for being patient with all the challenges I faced during the course of this project. I will forever be grateful for your presence and guidance, Professor.

I acknowledge the assistance I received from the Ozoemena Research Group, for being a family, with every member contributing to the success of this project. Special thanks to Itumeleng Seotsanyana-Mokhotsi and Dr. Thapelo Mofokeng for their extensive assistance with the overall work. I am especially appreciative of these two individuals who sacrificed their time and risked their lives to assist with starting the experimental work, even at the beginning of the Covid pandemic, and for remaining actively involved in the work ever since. I also want to express my gratitude to Dr. Aderemi Haruna for his constant support of the project (even beyond its scope), for monitoring the progress, and for utilizing his knowledge and wisdom to contribute to the project's success.

I would like to highly appreciate and acknowledge the National Metrology Institute of South Africa (NMISA) for providing X-ray photoelectron spectroscopy (XPS) and scanning electron microscopy (SEM) analysis of the materials. I am very grateful for the high-resolution transmission electron microscopy (HRTEM) characterizations provided by the Council for Scientific and Industrial Research (CSIR). My thanks go to the Wits Microscopy and Microanalysis Unit (MMU) for providing most of the morphological and structural analyses of the

samples. I am also glad to have been part of the CATMAT group, which contributed to the accumulation of knowledge involving the study of materials and electrochemistry.

I am very grateful to the Indabuko Institute (Energy Solutions) for funding this project and ensuring that my personal well-being is taken care of, making this life-changing opportunity possible.

ABSTRACT

Energy is one of the aspects that plays a central role in moving society forward since it is one of the most important agenda of global economic and energy forums. There is an urgent need to move to clean energy given the environmental and the health benefits resulting from implementing energy systems that utilize green energy. The proposed energy sources in these systems are primarily natural (e.g. wind and solar), which means they are beyond human control and would work better if coupled with energy storage devices (ESDs). From this emerge the importance of energy storage systems (ESSs) which mostly perform based on the materials utilized to assemble the devices.

In this study, we seek to enhance the power and energy densities of two of the prominent energy storage systems, namely lithium-ion batteries (LIBs) and lithium-ion capacitors (LICs), using modified commercial lithium titanate (LTO) materials as anodes. The materials consist of the pristine LTO (LTO-p), LTO coated with cerium fluoride (LTO-CeF_3) and dry and wet irradiated pristine LTO (LTO-p-md and LTO-p-mw) and LTO coated with cerium fluoride (LTO-CeF_3-md and LTO-CeF_3-mw). Microwave irradiation was used to study the possible defect that the radiation can bring to the materials and possibly use the microwave effect to improve their electrochemistry.

The effects of the coated layer of CeF_3 and microwave irradiation on the structure of the commercial LTO were extensively studied using powder X-ray diffractometer (XRD), Raman spectroscopy, transmission electron microscopy (TEM), high resolution transmission electron microscopy (HRTEM), scanning electron microscopy (SEM), Energy-dispersive X-ray spectroscopy (EDS), X-ray photoelectron spectroscopy (XPS), thermogravimetric analysis (TGA) and Brunauer-Emmett-Teller (BET) theory.

Structural investigations of TEM micrographs revealed CeF_3 was present on the surface of the coated LTO materials. Further analysis did show that some portion of the CeF_3 coating layer was co-doped into the LTO nanostructures. The findings from XRD and XPS analyses showed that co-doping promoted a mixed state of Ti^{3+} and Ti^{4+} resulting from charge compensation when Ce^{3+} and F^- possibly substituted Ti^{4+} and O^{2-}. This mixed state of titanium ions allowed the materials to have high electric conductivity than the pristine LTO (LTO-p). The spectrographs obtained from XPS analysis also showed that LTO microwave irradiated materials without coating experienced the same mixed states, which may have originated from oxygen vacancies that allowed for charge compensation when some of the LTO-p Ti^{4+} had to turn to Ti^{3+}. The HRTEM analysis demonstrated changes to the lattice planes spacing of the modified LTO materials and these changes supported the (111) lattice plane shifts observed in the XRD analysis.

The electrochemistry of the lithium-ion battery was studied on all the materials using cycling voltammetry (CV), galvanostatic charge-discharge (GCD) and electrochemical impedance spectroscopy (EIS) techniques. From GCD technique, the results indicated that the modified materials had higher specific capacities than LTO-p at all rates under rate capability studies. All as-prepared materials were stable with coulombic efficiency of almost 100% for 100 cycles using 1 C, with modified materials surpassing LTO-p specific capacity. Cycling at a high rate (5 C) for 1000 cycles, saw LTO-md, LTO-mw, LTO-CeF_3 and LTO-CeF_3-md having high-capacity degradation after 500 cycles. It was also observed that initial capacities were retained up to the 1000th cycle for LTO-CeF_3-mw and LTO-p.

With an aim of comparing LTO-p and LTO-CeF_3 half cells, these two materials were further studied for lithium-ion capacitors (LICs). This choice was based on LTO-CeF_3 having a better charge-discharge profile, high specific capacity and coulombic efficiency than LTO-p. The

improvements resulted from the coating layer (leveraging the high ionic conductivity and chemically inert properties of CeF_3) and the observed defects seen on the XPS studies created by the coating synthesis process. The LTO-CeF_3 anode was paired with a carbon black cathode to construct a full LIC cell. The assembled cell produced a maximal energy density of 107.4 Wh kg^{-1} with an accompanying power density of 2000 W kg^{-1}, and it yielded a power density of 10 000 W kg^{-1} with an energy density of 61.8 Wh kg^{-1}.

TABLE OF CONTENTS

Chapter 1 Introduction **22**

1.1 Background to the study **22**

1.2 Motivation for the study **24**

1.3 Objectives of the study **25**

1.4 Outline of the dissertation **26**

1.5 References **27**

Chapter 2 Literature review **29**

2.1 Energy storage systems **29**

2.2 Brief histories of the studied ESSs devices **31**

2.2.1 Li-ion batteries **31**

2.2.2 Li-ion capacitors **32**

2.3 Working mechanism of the storage devices **33**

2.3.1 Lithium-ion batteries **33**

2.3.2 Lithium-ion capacitors **36**

2.4 Material characterization **38**

2.4.1 X-ray diffractometry (XRD) **38**

2.4.2 Raman spectroscopy **40**

2.4.3 Transmission electron microscopy (TEM) **41**

2.4.4 High-Resolution Transmission electron microscopy (HRTEM) 42

2.4.5 Scanning electron microscopy (SEM) 43

2.4.6 Energy dispersive X-ray spectroscopy (EDS) 43

2.4.7 X-ray photoelectron spectroscopy (XPS) 44

2.4.8 Brunauer-Emmett-Teller analysis (BET) 45

2.4.9 Thermogravimetric analysis (TGA) 46

2.5 Electrochemical analyses 47

2.5.1 Cyclic voltammetry 47

2.5.2 Electrochemical impedance spectroscopy (EIS) 49

2.5.3 Galvanostatic tests 50

2.6 Spinel lithium titanate ($Li_4Ti_5O_{12}$) as an anode in energy systems 53

2.6.1 Spinel $Li_4Ti_5O_{12}$ 53

2.6.2 Lithium diffusion in $Li_4Ti_5O_{12}$ 55

2.6.3 Challenges and mitigation strategies of $Li_4Ti_5O_{12}$ anodes 57

2.7 Cerium fluoride (CeF_3) coating in electrodes 61

2.8 References 64

Chapter 3 Experimental section 76

3.1 Materials and Chemicals 76

3.2 Synthesis of materials 76

3.2.1 Syntheses of electrode materials 76

3.2.2 Modification of anode materials 77

3.3 Material characterization 79

3.3.1 X-ray diffractometry (XRD) 79

3.3.2 Raman spectroscopy 80

3.3.3 Transmission electron microscopy (TEM) 80

3.3.4 Scanning electron microscopy (SEM) 80

3.3.5 Energy dispersive X-ray spectroscopy (EDS) 80

3.3.6 X-ray photoelectron spectroscopy (XPS) 81

3.3.7 Brunauer-Emmett-Teller analysis (BET) 81

3.3.8 Thermogravimetric analysis (TGA) 81

3.4 Electrochemical analyses 82

3.4.1 Cells configuration 82

3.4.2 Cyclic voltammetry 83

3.4.3 Electrochemical impedance spectroscopy (EIS) Electrochemical half-cells 84

3.4.4 Galvanostatic tests 84

3.5 References 85

Chapter 4 Defect-engineered lithium titanate oxide (LTO) anode materials for lithium-ion batteries 86

4.1 Introduction 86

4.2 Results and discussion 88

4.2.1 Material characterization 88

4.2.1.1 Powder X-ray diffraction (PXRD) 88

4.2.1.2 Raman spectroscopy 91

4.2.1.3 Transmission electron microscopy (TEM) 92

4.2.1.4 High-Resolution Transmission electron microscopy (HRTEM) 94

4.2.1.5 Energy dispersive X-ray spectroscopy (EDS) 98

4.2.1.6 X-Ray photoelectron spectroscopy (XPS) 101

4.2.1.7 Brunauer -Emmett-Teller analysis (BET) 105

4.2.1.8 Thermogravimetric analysis (TGA) 106

4.2.1.9 Scanning electron microscopy (SEM) 107

4.2.2 Electrochemical measurements 109

4.2.2.1 Cyclic voltammetry (CV) 109

4.2.2.2 Galvanostatic charge-discharge (GCD) 112

4.2.2.3 Rate capability 120

4.2.2.4 Electrochemical impedance spectroscopy (EIS) 121

4.3 Conclusion 128

4.4 References 129

Chapter 5 CeF_3-coated lithium titanate oxide ($Li_4Ti_5O_{12}$) anode for lithium-ion capacitors 139

5.1 Introduction 139

5.2 Results and discussion 141

5.2.1 Half-cell electrochemistry comparison 141

5.2.1.1 Cyclic voltammetry (CV) 141

5.2.1.2 Galvanostatic charge-discharge (GCD) 143

5.2.1.3 Specific capacity and Coulombic efficiency 145

5.2.1.4 Choosing the anode active material 146

5.2.2 Full cell electrochemistry 146

5.2.2.1 Cyclic voltammetry of LTO-CeF_3 and carbon black super C45 146

5.2.2.2 Cyclic voltammetry (CV) of LTO-CeF_3//CB 148

5.2.2.3 Galvanostatic charge-discharge (GCD) of LTO-CeF_3//CB 149

5.2.2.4 Specific capacitance 150

5.2.2.5 Ragone plot 153

5.3 References 155

Chapter 6 General conclusion 158

6.1 Conclusion 158

6.2 Future work 160

LIST OF FIGURES

Figure 1.1: Ragone plot of numerous storage devices [4]. 23

Figure 2.1: Energy storage systems and their potential applications [6]. 30

Figure 2.2: History of lithium-ion batteries [8]. 31

Figure 2.3: History of lithium-ion capacitors. 33

Figure 2.4: Li-ion battery's schematic [17]. 34

Figure 2.5: Diagrams of LIB, supercapacitor and LIC [28]. 37

Figure 2.6: Storage mechanisms of LICs, (a) electrolyte-consumption and (b) lithium-ion transport [26]..... 38

Figure 2.7: X-ray diffraction schematic of 2 dimensional crystal [32]..... 39

Figure 2.8: Raman scatterings [34]. 41

Figure 2.9: Transmission Electron Microscopy working principle [38]..... 42

Figure 2.10: Working principle depiction of SEM [41]. 43

Figure 2.11: Working mechanism of EDS [45]. 44

Figure 2.12: Photoelectric effect caused by X-rays. 45

Figure 2.13: BET working principle. 46

Figure 2.14: Working principle of TGA. 47

Figure 2.15: (a) Voltage waveform applied in CV, (b) CV curve of potential against current response. 48

Figure 2.16: Nyquist plot and the equivalent Randles circuit. 49

Figure 2.17: (a) Charge and discharge curves, (b) rate capability performance, (c) Coulombic efficiency plot. 52

Figure 2.18: Spinel structure diagram [58]. 53

Figure 2.19: (a) LTO in Spinel structure, (b) LTO in rock-salt structure [67]. 55

Figure 2.20: Further Li-ion insertion from the rock salt structure [71]. 57

Figure 2.21: Solvents and produced gas species of LTO [95]. 60

Figure 2.22: Concentration of decomposed chemical species at different temperatures [95]. 60

Figure 2.23: DSC plots of the bare-$LiCoO_2$ and coated -$LiCoO_2$ cathodes at fully charged state. [103]..... 63

Figure 3.1: Synthesis flow of LTO-CeF_3. 78

Figure 3.2: Syntheses of microwaved materials. 79

Figure 3.3: (a) Coin cell components **[3]**, (b) Schematic of T-type Swagelok cell. 83

Figure 4.1: (a) XRD patterns, (b) 111 peaks of LTO-p, LTO-md, LTO-mw, LTO-CeF_3, LTO-CeF_3-md, and LTO-CeF_3-mw..... 89

Figure 4.2: Raman spectra of the materials. 91

Figure 4.3**:** TEM micrographs of (a) LTO-p, (b) LTO-mw, (c) LTO-CeF_3 and (d) LTO-CeF_3-mw. 93

Figure 4.4: HRTEM image of (a) LTO-p, region and SAED image of (b) LTO (111) and (c) LTO (111) lattice plane on LTO-p. 95

Figure 4.5: HRTEM image of (a) LTO-mw, region and SAED image of (b) LTO (222), (c) LTO (311), (d) LTO (311), and LTO (220) lattice plane on LTO-mw. 95

Figure 4.6**:** HRTEM image of (a) LTO-CeF_3, region and SAED image of (b) TiO_2 anatase (101), (c) CeF_3 (111), (d) CeF_3 (111), and (e) LTO (111) lattice plane on LTO- CeF_3..... 97

Figure 4.7**:** HRTEM image of (a) LTO-CeF3-mw, region and SAED image of (b) LTO (311), (c) LTO (220) (d) TiO_2 anatase (101), and (e) CeF_3 (111) lattice plane on LTO- CeF_3-mw. 97

Figure 4.8: SEM micrographs of (a) LTO-p, with its associated (b) Ti and (c) O elemental mapping. 98

Figure 4.9**:** SEM micrographs of (a) LTO-mw, with its associated (b) Ti and (c) O elemental mapping. 99

Figure 4.10**:** SEM micrograph of (a) LTO-CeF_3, with its associated (b) Ti, (c) O, (d) Ce, and (e) F elemental mapping. 100

Figure 4.11: SEM micrographs of (a) LTO-CeF_3-mw , with its associated (b) Ti, (c) O, (d) Ce, and (e) F elemental mapping. 100

Figure 4.12: XPS spectra of the materials. 101

Figure 4.13: Deconvolution of Ce3d in (a) LTO-CeF_3, (b) LTO-CeF_3-md, (c) LTO-CeF_3-mw and (d) XPS spectra of the materials at 660-700 eV. 102

Figure 4.14**:** Deconvolution of Ti2p on (a) LTO-p, (b) LTO-CeF_3, (c) LTO-md, (d) LTO-CeF_3-md, (e) LTO-mw, and (d) LTO-CeF_3-mw material..... 103

Figure 4.15**:** TGA curves of the samples. 107

Figure 4.16: SEM image of (a) LTO-p, (b) LTO-CeF_3, (c) LTO-md, (d) LTO-CeF_3-md, (e) LTO-mw, and (d) LTO-CeF_3-mw. 108

Figure 4.17**:** CV plots of the materials at 0.1 mVs^{-1} of (a) LTO-p, LTO-CeF_3, (b) LTO-md, LTO-CeF_3, and (c) LTO-mw, LTO-CeF_3-mw. 110

Figure 4.18**:** Charge/discharge of all materials at 1C for 100 cycles..... 113

Figure 4.19**:** Discharge capacity and coulombic efficiency of (a) LTO-p, (b) LTO-CeF_3, (c) LTO-md, (d) LTO-CeF_3-md, (e) LTO-mw, and (f) LTO-CeF_3-mw at 1C for 100 cycles. 115

Figure 4.20**:** Charge/discharge plots of (a) LTO-p, (b) LTO-CeF_3, (c) LTO-md, (d) LTO-CeF_3-md, (e) LTO-mw, and (f) LTO-CeF_3-mw at 5C for 1000 Cycles. 118

Figure 4.21**:** Discharge capacity and coulombic efficiency of (a) LTO-p, (b) LTO-CeF_3, (c) LTO-md, (d) LTO-CeF_3-md, (e) LTO-mw, and (f) LTO-CeF_3-mw at 5C for 1000 Cycles. 119

Figure 4.22**:** Rate capability of the LTO-p, LTO-CeF_3, LTO-md, LTO-CeF_3-md, LTO-mw, and LTO-CeF_3-mw. 121

Figure 4.23: Nyquist plots before and after 1000 cycles of (a) LTO-p, (b) LTO-CeF_3, (c) LTO-md, (d) LTO-CeF_3-md, (e) LTO-mw, and (f) LTO-CeF_3-mw. 123

Figure 4.24**:** Equivalent circuit of the materials (a) before cycling and only after cycling for LTO-p, and (b) After cycling. 124

Figure 5.1: Half-cell CV plots at numerous scan rates: (a) LTO-p, (b) LTO-CeF_3, and (c) comparison of LTO-P and LTO-CeF_3 at 2.5 mVs^{-1}. 142

Figure 5.2: Charge-discharge plots of (a) LTO-p, (b) LTO-CeF_3 at several current densities, (c) LTO-p and LTO-CeF_3 capacities comparison at 1 Ag^{-1}. 144

Figure 5.3: (a) Specific capacity at several current densities, (b) Coulombic efficiency of LTO-p and LTO-CeF_3. 145

Figure 5.4: CV plots of carbon black and LTO-CeF_3. 147

Figure 5.5: CV curves of LTO-CeF_3// CB full cell at various scan rates. 149

Figure 5.6: Charge-discharge of LTO-CeF_3//CB full cell at several current densities. 150

Figure 5.7: Specific capacitance at various current density. 151

Figure 5.8: Specific capacitance and coulombic efficiency observed on 100 cycles. 152

Figure 5.9: Ragone plot for LIC full cell made up of LTO anode and CB cathode, compared with the literature. 154

LIST OF TABLES

Table 4.1: Comparison of peak intensity ratios. 90

Table 4.2: Nitrogen gas adsorption analysis of the materials. 105

Table 4.3: CV redox reaction parameters for the samples. 111

Table 4.4: Specific capacities at 1^{st} and 100^{th} cycles. 114

Table 4.5: Specific capacities for 5C cycling. 117

Table 4.6: EIS parameters for materials before 1000 electrochemical cycling experiments. 125

Table 4.7: EIS parameters for materials after 1000 electrochemical cycling experiments. 127

LIST OF ABBREVIATIONS

BET:	Brunauer-Emmett-Teller
CB	Carbon black
CV:	Cyclic voltammetry
DEC:	Diethyl carbonate
CeF_3:	Cerium fluoride
DMC:	Dimethyl carbonate
EDLC:	Electric double layer capacitor
EC:	Ethylene carbonate
EV:	Electric vehicle
EIS:	Electrochemical impedance spectroscopy
ESSs:	Energy storage systems
GCD:	Galvanostatic charge-discharge
HRTEM:	High resolution transmission electron microscope
Li:	Lithium
LIB:	Lithium-ion battery
LIC:	Lithium-ion capacitor
LTO ($Li_4Ti_5O_{12)}$):	Lithium titanate oxide

md:	Microwave dry
mw:	Microwave wet
OVs:	Oxygen vacancies
p:	Pristine
PXRD:	Powder X ray diffraction
SEM:	Scanning electron microscopy
TEM:	Transmission electron microscope
TGA:	Thermal gravimetry analysis
V:	Volt
XPS:	X ray photoelectron spectroscopy

Chapter 1
Introduction

1.1 Background to the study

Energy is one of the crucial enabling factors to advance science, technology, and industrialization in the world. But the present ways of harnessing and utilizing energy through the use of fossil fuels (coal, oil and gas) are detrimental to the future of life on earth. They contribute to increasingly experienced problems posed by global warming and environmental pollution. As a result, attention has been devoted to looking for alternative power sources that can provide clean energy with high efficiency and reduce the emissions of greenhouse gases.

Solar and wind power are at the forefront of recommended renewable energy sources for providing power to the electrical grid and for carrying out the load levelling. Also, the automobile industry is aiming to shift to electric vehicles (EVs) [1] to reduce CO_2 emissions offered by their gasoline counterparts. To implement these strategies successfully, energy storage systems (ESSs) having high energy density, elevated power density, excellent safety, cost-effective production, and maintenance must be deployed.

The currently viable electrochemical energy storage devices meeting these qualities are lithium-ion batteries (LIBs) and supercapacitors. Figure 1.1 illustrates the Ragone plot for the most important energy storage systems. LIBs exhibit energy density in the range 150-200 Wh Kg^{-1}, lifespan of < 10^{-3} times, great safety, environmental benignity, and reasonable cost [2, 3]. These qualities are the ones that led them to their commercialization in portable electronic machines like

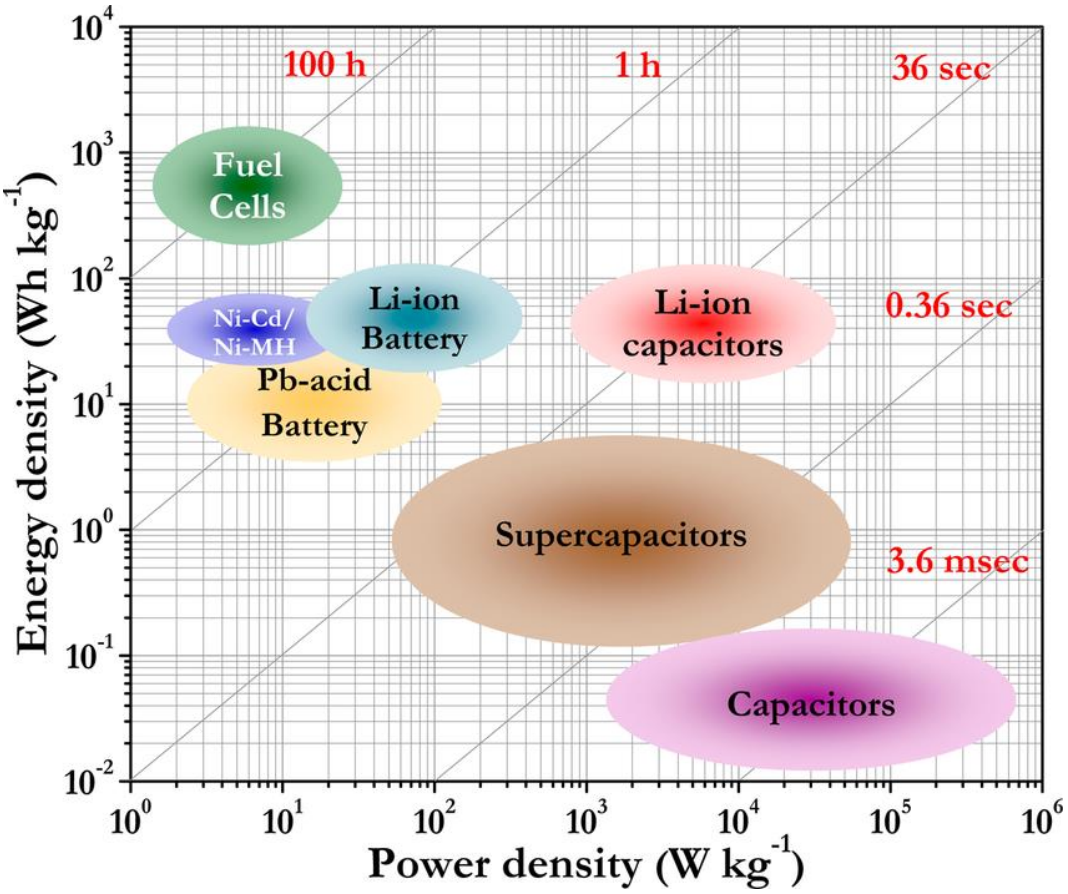


Figure 1.1: Ragone plot of numerous storage devices [4].

laptops and mobile phones. On the other hand, supercapacitors hold success in applications that require a fast charge supply momentarily. They are able to achieve this because of their high-power density ($> 10^3$ W kg^{-1}) and high cycle life (> 100 000 cycles)[3, 5]. In spite of these, supercapacitors suffer from low energy density (< 10 Wh kg^{-1}) [6].

The new class of supercapacitors, called lithium-ion capacitors (LICs) mitigate the challenges met by both supercapacitors and batteries for future applications of energy storage systems by employing a hybrid system that borrows structural constituents from LIBs and supercapacitors [7].

LICs possess elevated power density than LIBs and have greater energy density than supercapacitors [5]. The current performances of both LIBs and LICs are not enough for some future requirements, which introduce a new set of demands on storage devices pertaining to their lifetime, power, and energy density.

1.2 Motivation for the study

This study is dedicated to developing LIBs and LICs that can surmount the challenges inherent in the current ones. LIBs and LICs were chosen because of their promising extensive use in future practical applications of ESSs. The qualities of each of these storage devices are ascribed to their working mechanism, with LIBs using Faradaic reactions in both electrodes for generating energy and LICs utilizing Faradaic reactions at the anode and non-Faradaic reactions in the cathode [5]. To achieve the desired performance of these storage devices, a significant amount of study must be focused on identifying electrode materials that will maximize their electrochemical performance.

Lithium titanate ($Li_4Ti_5O_{12}$) is categorized as a suitable candidate for electrochemical power sources for future sustainable and renewable systems [8]. This is because of its small volumetric change (about 0.2 %) during the intercalation/deintercalation of Li^+ ions, high plateau voltage at 1.55 V (vs Li/Li^+), long cycle life and outstanding safety [9, 10]. Additionally, the zero-strain property of $Li_4Ti_5O_{12}$ promotes better cycling performance by maximizing structural stability and minimizing the possibility of dendrite growth. The high potential plateau of 1.55 V prevents the electrolyte decomposition and hence, hinders the emergence of solid-electrolyte interface (SEI) layer. These electrochemical valuables lead to outstanding capacity retention, lifetime, and safety of systems that use LTO as an anode electrode. Even with these appealing qualities, LTO fails to

be employed in practical applications due to its low electronic conductivity, diffusion coefficient, theoretical capacity (175 mAh/g), and the experienced generations of gases at elevated temperatures [1, 11].

The ongoing scientific and engineering research targets to remedy these problems as they are critical for the urgently needed clean and sustainably powered world. The proposed solutions for overcoming these shortfalls include using nanostructured LTO, introducing conductive coating to the LTO surface, doping LTO with conductive elements, and creating LTO composite materials with conductive agents [9]. In this work, commercial LTO is modified with CeF_3 surface coating for enhanced electrochemical activities, the choice was motivated by the elevated ionic conductivity and the chemical stability of CeF_3. Microwave irradiation is also adapted for faster heat rates, saving energy, and for improving the electrochemical processes of the materials.

1.3 Objectives of the study

Aim: This dissertation aims to modify commercial LTO by the use of surface coating using cerium fluoride CeF_3 and microwave-assisted synthesis for enhanced electrochemical performance for LIBs and LICs.

Objectives:

1. To coat pristine LTO with 2 wt% CeF_3.
2. To use microwave-assisted method to synthesize LTO-md, LTO-mw, LTO-CeF_3-md and LTO-CeF_3-mw.
3. To investigate the effect of coating and microwave irradiation on the synthesized anode materials using XRD, Raman, TEM, HRTEM, SEM, EDS, XPS, BET and TGA.

4. To investigating the electrochemical performance of the prepared materials using coin type Li-ion cells and LIC t-type Swagelok cell.

1.4 Outline of the dissertation

Chapter 1 (Introduction): This section offers the motivation, objective, and the scope of the dissertation.

Chapter 2 (Literature review): This chapter reviews the progress and current work of LTO anode in Li-ion batteries and Li-ion capacitors.

Chapter 3 (Experimental section): This chapter outline the synthesis and the analytical techniques used in this study.

Chapter 4 (Results and discussion): This part of the dissertation presents and offers discussions on the attained results of studying pristine, CeF_3 coated, and microwave irradiated LTO materials for Li-ion batteries.

Chapter 5 (Results and discussion): This segment offers the results and the uncovered electrochemical insights of pristine LTO and CeF_3-coated LTO in the Li-ion capacitors study.

Chapter 6 (General conclusions): This section concludes on the results and presents recommendations for possible future work.

1.5 References

[1] Yoon, J.K., Nam, S., Shim, H.C., Park, K., Yoon, T., Park, H.S. & Hyun, S. 2018. Highly-stable Li4Ti5O12 anodes obtained by atomic-layer-deposited Al2O3. *Materials,* 11**,** 803.

[2] Wang, H., Zhu, C., Chao, D., Yan, Q. & Fan, H.J. 2017. Nonaqueous hybrid lithium-ion and sodium-ion capacitors. *Advanced materials,* 29**,** 1702093.

[3] Balamurugan, J., Nguyen, T.T., Aravindan, V., Kim, N.H. & Lee, J.H. 2018. Flexible solid-state asymmetric supercapacitors based on nitrogen-doped graphene encapsulated ternary metal-nitrides with ultralong cycle life. *Advanced Functional Materials,* 28**,** 1804663.

[4] Aravindan, V., Gnanaraj, J., Lee, Y.S. & Madhavi, S. 2014. Insertion-type electrodes for nonaqueous Li-ion capacitors. *Chemical reviews,* 114**,** 11619-11635.

[5] Li, B., Zheng, J., Zhang, H., Jin, L., Yang, D., Lv, H., Shen, C., Shellikeri, A., Zheng, Y. & Gong, R. 2018. Electrode materials, electrolytes, and challenges in nonaqueous lithium-ion capacitors. *Advanced materials,* 30**,** 1705670.

[6] Han, P., Xu, G., Han, X., Zhao, J., Zhou, X. & Cui, G. 2018. Lithium ion capacitors in organic electrolyte system: scientific problems, material development, and key technologies. *Advanced Energy Materials,* 8**,** 1801243.

[7] Zou, K., Cai, P., Cao, X., Zou, G., Hou, H. & Ji, X. 2020. Carbon materials for high-performance lithium-ion capacitor. *Current Opinion in Electrochemistry,* 21**,** 31-39.

[8] Liu, W., Wang, Y., Jia, X. & Xia, B. 2013. The characterization of lithium titanate microspheres synthesized by a hydrothermal method. *Journal of Chemistry,* 2013.

[9] Yang, X., Huang, Y., Wang, X., Jia, D., Pang, W.K., Guo, Z. & Tang, X. 2014. High rate capability core–shell lithium titanate@ ceria nanosphere anode material synthesized by one-pot co-precipitation for lithium-ion batteries. *Journal of Power Sources,* 257**,** 280-285.

[10] Babu, B., Lashmi, P. & Shaijumon, M. 2016. Li-ion capacitor based on activated rice husk derived porous carbon with improved electrochemical performance. *Electrochimica Acta,* 211**,** 289-296.

[11] Yu, Y. & Guo, Y. 2019. Cerium oxide-modified lithium chromium titanate as high-performance anode material for lithium-ion battery. *Ionics,* 25**,** 367-371.

Chapter 2
Literature review

2.1 Energy storage systems

The aim for ease and better everyday life and rapid economic development introduces an emergency need for applications that require an increase in energy storage systems coupled with better storage technologies and chemistry. ESSs are at the heart of almost every application. Their usage range from portable electronic applications to hybrid and electric cars in the transportation sector and are coupled with renewable energy sources for storing the renewable power [1]. Some of the common ESSs and their respective potential applications are shown in Figure 2.1. The multitude of applications introduced different classes of storage chemistries and mechanisms in ESSs devices.

The two important storage devices in practical applications are secondary batteries and supercapacitors or electrical double-layer capacitors (EDLCs). Secondary batteries are utilised in applications that require high energy density, while supercapacitors are utilized in applications with high power output [2]. These storage systems have been intensely studied in literature and widely utilized in commercial applications. Regardless of their current success, the increasing energy demand gives the need to further explore newer technologies, improve upon the existing ones, thereby extending their capacities and applications [3]. Heavy-duty applications usually require both higher energy and power density. In these kinds of applications, hybrid energy storage systems such as Li-ion capacitors are used to consolidate the qualities of batteries and supercapacitors [4, 5]. The successive sections of this chapter will discuss some critical aspects of

the studied ESSs systems in this dissertation, which are the LIBs and LICs. The discussion will revolve around the use of LTO in these systems, with their brief histories, their working mechanisms, the movement of Li^+ into the spinel LTO, the challenges and mitigation strategies meant to promote the use of LTO.

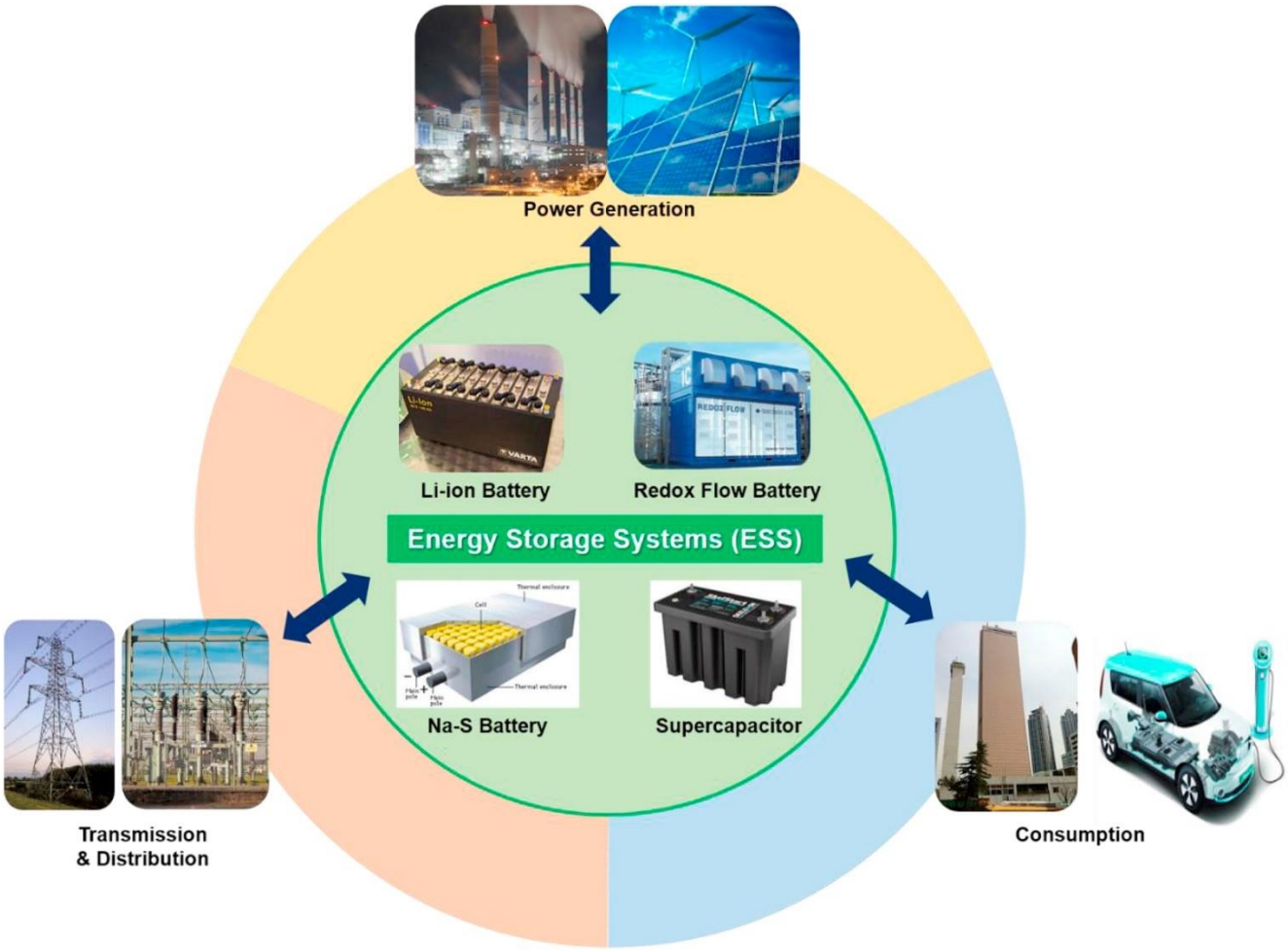


Figure 2.1: Energy storage systems and their potential applications [6].

2.2 Brief histories of the studied ESSs devices

2.2.1 Li-ion batteries

The inception of batteries span from 1800 when Alessandro Volta introduced the first battery [7]. Then this was followed by the invention of Lead-acid battery around 1860, which in 1880 was offered to the market [8]. Several battery technologies were explored and invented, which led to the exploration of Li-ion batteries as demonstrated on Figure 2.2. During the 1970s oil crisis, Stanley Whittingham looked for a battery that might lead to fossil-free energy and recharge on its own [9].

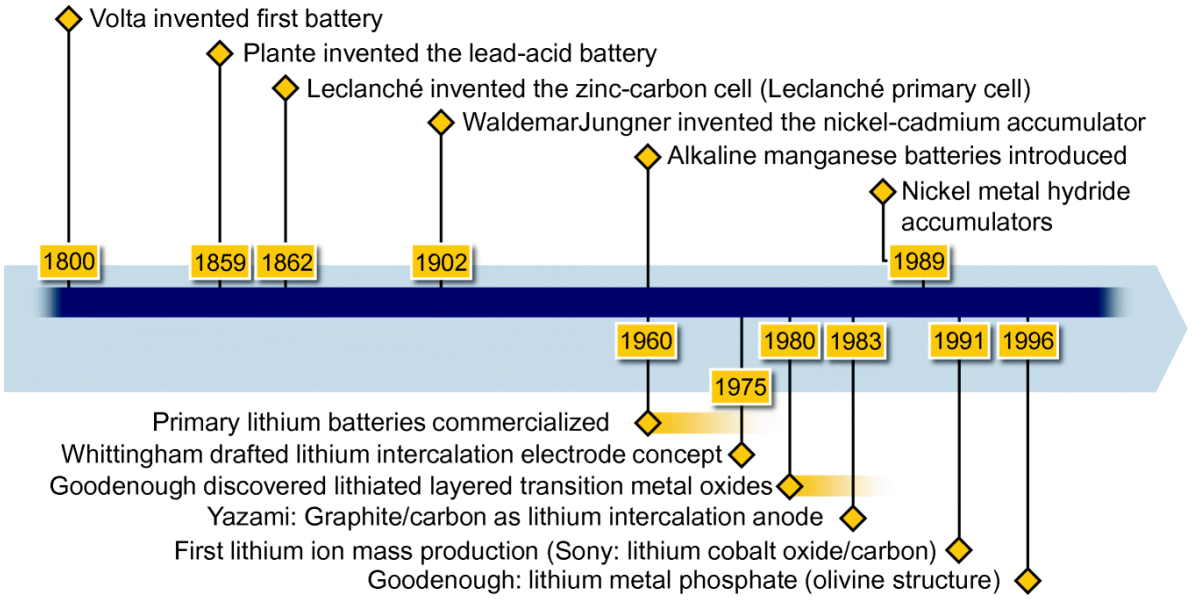


Figure 2.2: History of lithium-ion batteries [8].

In 1976, Whittingham together with Michel Armand, and Robert Huggins attempted to combine titanium disulfide (TiS_2) cathode with a lithium metal anode, the battery suffered from dendrite

growths and caught fire as a result of a short circuit [10]. These safety concerns led Exxon to terminate further experimentation. Then in the 1980s, a safer and stable battery which substituted titanium disulfide cathode with two-layered lithium cobalt and consisting of carbonaceous petroleum coke anode was created. Sony Corporation was first to offer first lithium-ion mass production with commercialization of a battery that consisted of $LiCoO_2$ cathode and carbon anode in 1991 [11, 12]. LTO was proposed as an anode material in the 1990s, which was used to substitute graphite in LICs when high-power density was needed.

2.2.2 Li-ion capacitors

LICs are reported to originate from the study of polyacenic semiconductive (PAS) in 1987 by Dr. Yamabe, in collaboration with Dr. Yata [13], where they noticed the insertion of lithium into PAS. Then two years later, in 1989, a coin type capacitor utilizing PAS as a cathode and anode material, was put on the market by Shizukuni Yata [13, 14]. In 1992, the prelithiation approach was first applied on PAS to increase the working voltage of PAS capacitors to 3.3 V. Following these studies, a hybrid capacitor made up of graphite anode and activated carbon (AC) cathode immersed in an organic electrolyte, was constructed by Morimoto, T., in 1999 [15]. Around 1999-2001, a hybrid capacitor made up of LTO anode and AC cathode, was initiated by the Amatucci's group [16]. Figure 2.3 outlines this history of LIC systems.

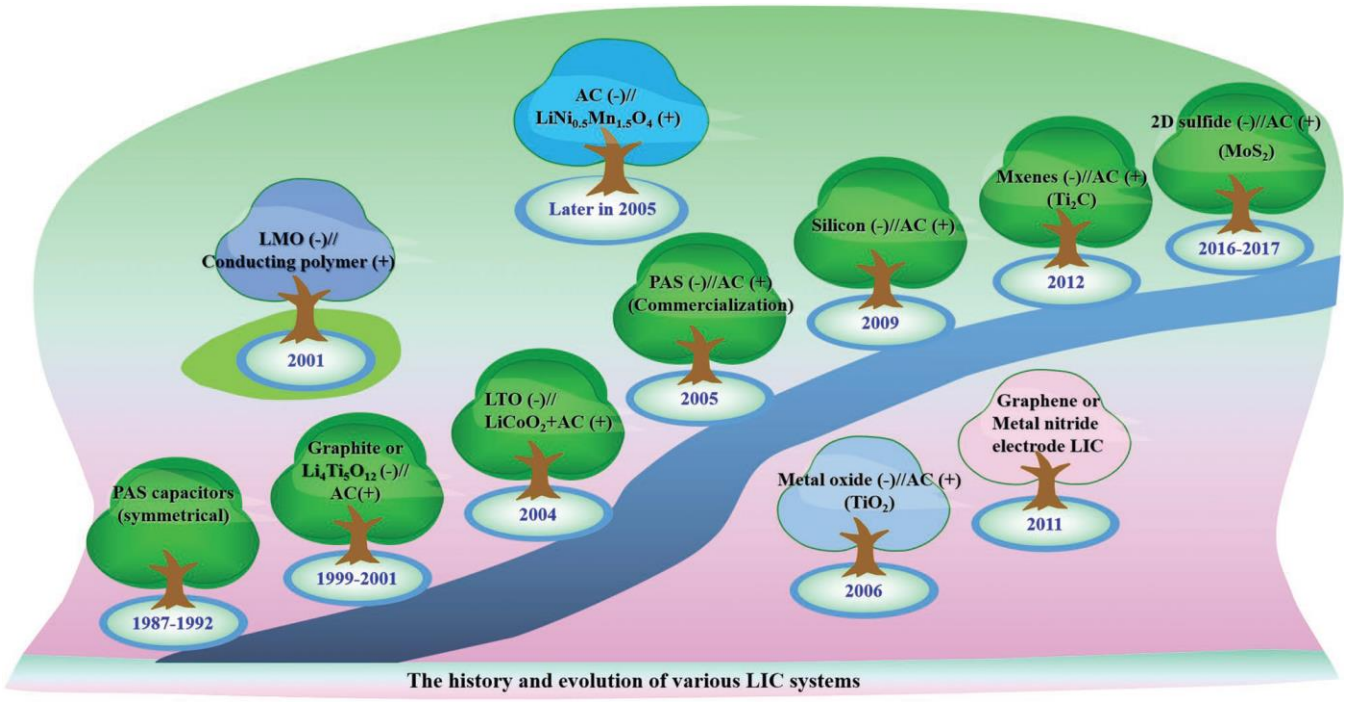


Figure 2.3**:** History of lithium-ion capacitors.

2.3 Working mechanism of the storage devices

2.3.1 Lithium-ion batteries

LIBs are electrochemical storage devices that utilize redox reactions for storing and retrieving energy. Redox reactions involve a transfer of electrons between species that undergo a change in oxidation states, resulting in oxidation and reduction processes. In a battery, these two processes are mechanically separated and connected via an external circuit. The oxidation site in this device is commonly known as an anode, and the reduced site is called the cathode, with the schematic configuration of the Li-ion battery in Figure 2.4.

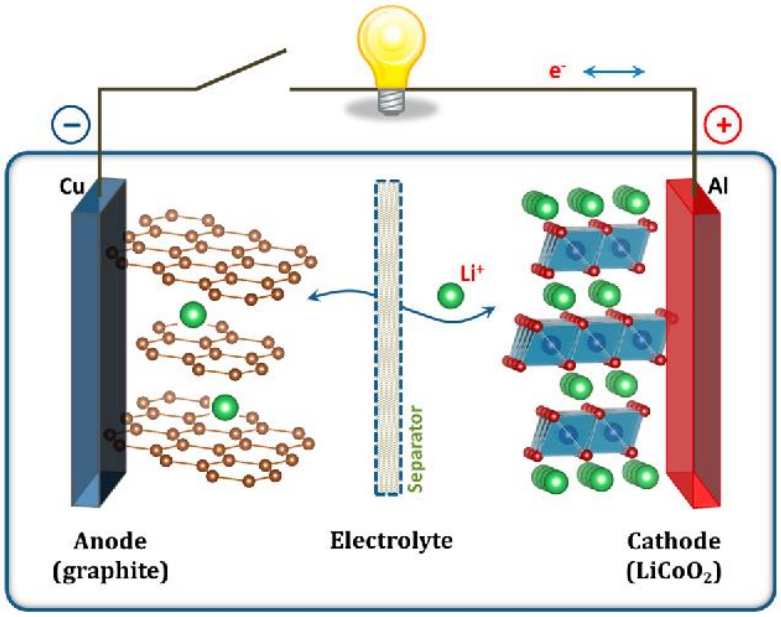


Figure 2.4: Li-ion battery's schematic [17].

Anodes are made up of active materials that can store lithium-ions reversibly, while cathodes usually consist of Li-containing metal oxides [18]. An electronically insulating and ionically conductive electrolyte separate the electrodes, as shown in Figure 2.4. The electrolyte facilitates the movement of the ions between electrodes [19], but it is not sufficient for mechanically separating the electrodes from conduct that might result in a device short circuit; therefore, a microporous polymer membrane separator soaked with the electrolyte is utilized in preventing a possible diversion of the current [20]. Current collectors, which typically consist of aluminium foil in the cathode and copper foil at the anode, connect the electrodes to the external circuit. To charge Li-ion battery, an external electric supply device gets connected to the electrodes. During charging, cathode's Li^+ ions migrate towards the anode via the electrolyte and the separator [21]. The cathode is oxidized (loss of electrons) in this process. The electrons travel via the external circuit and reduce (gain of electrons) the anode. When all the ions and the electrons are received at the anode,

the battery is fully charged. Hence, the external energy is now stored electrochemically by the device. The chemical processes are depicted by equations 2.1 and 2.2 below.

$$\text{Cathode: } LiCoO_2 \underset{\text{Charge [Oxidation]}}{\overset{\text{Discharge [Reduction]}}{\rightleftharpoons}} Li_{1-x}CoO_2 + xLi^+ + xe^- \quad (2.1)$$

$$\text{Anode: } C_y + xLi^+ + xe^- \underset{\text{Charge [Reduction]}}{\overset{\text{Discharge [Oxidation]}}{\rightleftharpoons}} Li_xC_y \quad (2.2)$$

When the battery is in discharging process, the anode gets oxidized while the cathode undergoes reduction. The ions travel via the same path to the cathode and the electrons use the outer circuit through a load to the cathode [22]. Therefore, an overall operating mechanism of a battery depends on the back-and-forth movement of Li^+ ions on the cell constituent during the charge and discharge processes.

2.3.2 Lithium-ion capacitors

Capacitors store energy using static charge as opposed to an electrochemical reaction. Capacitors are comprised of two electrodes split by a dielectric material [23]. Applying a potential across these electrodes induces positive and negative charged electrode surfaces, which results in opposite charges moving towards the surface with opposite polarity. Supercapacitors (SCs) employ the same cell construction in a battery, where the two electrodes are submerged in an electrolyte. The materials utilized in SCs possess high surface area, which allows SCs to have higher capacitance [24]. SCs usually employ a symmetric device structure with activated carbon used in both electrodes.

To account for both the desirable energy output of the LIBs and SCs, LICs utilize the same components as the LIBs, the only difference is that LICs have a battery-type cathode and an anode of a capacitive material, as shown in the diagram in Figure 2.5 [25]. The assembly consist of adsorption/desorption at the cathode surface and intercalation/de-intercalation of lithium occurring at the anode structure [26]. Several operating mechanisms found in LICs depend on whether the electrolyte is consumed or not. The first one is the well-known lithium-ion transport mechanism, where the cathode is the Li-ion source, and the anode consists of a capacitive active material. During charging process, the lithium-ions originating from the cathode material enter the electrolyte, while the Li-ions from the electrolyte migrate to the anode [27]. Then during discharge, the Li-ions escape the electrolyte and move back to the cathode. Examples of this kind of system include assemblies like AC/$LiMn_2O_4$ [27].

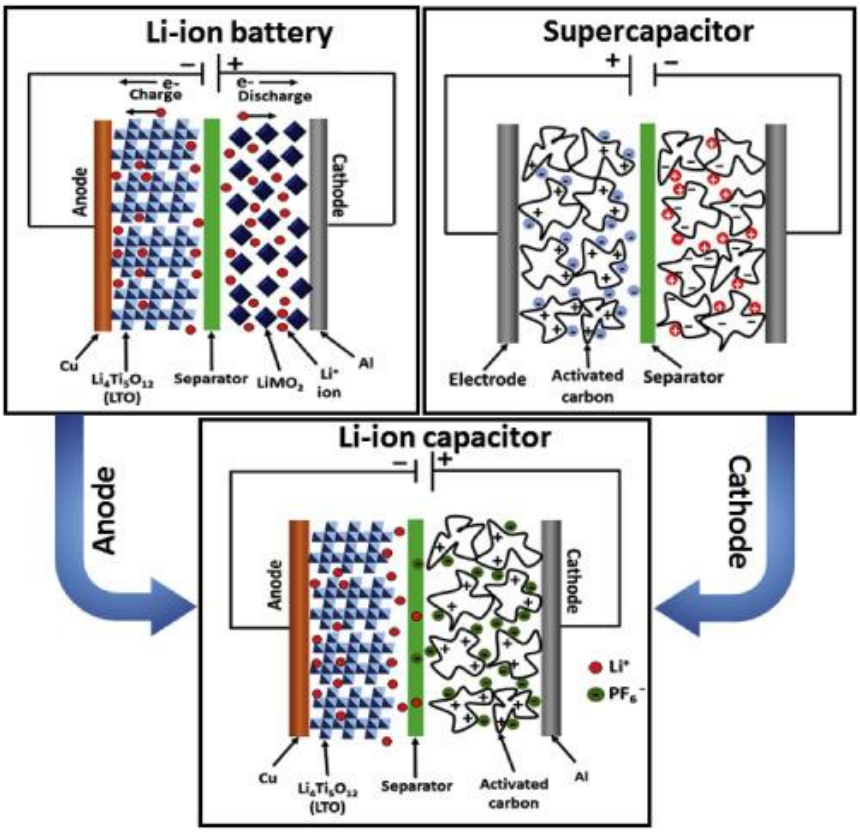


Figure 2.5: Diagrams of LIB, supercapacitor and LIC [28].

The second mechanism, which is the one used by the LIC investigated in this study, is known as the electrolyte-consumption mechanism. To achieve this mechanism, the LIC is fabricated using a metal oxide anode ($Li_4Ti_5O_{12}$) and a capacitive active material as a cathode (Activated carbon) [27]. During charge operation, the electrolyte anions LiP_6^- move to the cathode surface and the Li^+ ions are inserted into the negative electrode [28, 29]. During discharge, the anions from the cathode migrate back to the electrolyte and the Li^+ ions de-insert, move back to the electrolyte for charge balance. The final working mechanism of LIC devices involves the use of mixed materials on the

assembly, which may be $Li_4Ti_5O_{12}$/(AC+ $LiMn_2O_4$.) [27]. The examples of cell assembly of these mechanisms are shown in Figure 2.6.

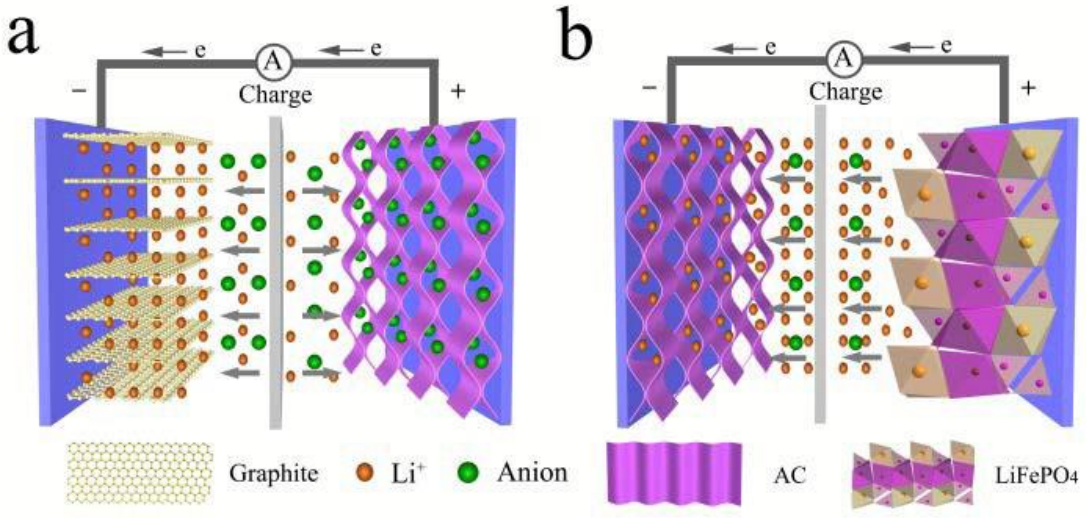


Figure 2.6: Storage mechanisms of LICs, (a) electrolyte-consumption and (b) lithium-ion transport [26].

2.4 Material characterization

2.4.1 X-ray diffractometry (XRD)

X-ray diffractometry (XRD) is a characterization technique utilized to obtain information of the chemical and physical composition of crystalline material [30]. This is achieved by studying crystallographic information arising from a coherent scattering of X-rays caused by crystalline materials. Atomic separations in a crystal lattice are usually in the order of X-ray wavelength (10^{-10} m), and this allows the creation of a diffraction pattern when X-rays interact with crystalline material. When an X-ray beam gets pointed to a crystalline sample, parallel incident rays (two for

instance) from an angle θ with the crystal plane. When these rays are reflected, constructive interference occurs if the total distance travelled ($2d \sin \theta$) by the rays is a whole number multiple of the X-ray wavelengths (λ). That is, when these rays are in phase [31].

The part of the incident beam that is deflected by angle 2θ having constructive interference gets registered as a spot on an interference pattern. The concept is indicated in Figure 2.7. The intensity of the created peaks and their corresponding positions on the interference pattern are unique to each material. Therefore, this allows the technique to be used in identifying material properties and for curating a fingerprint database system for materials.

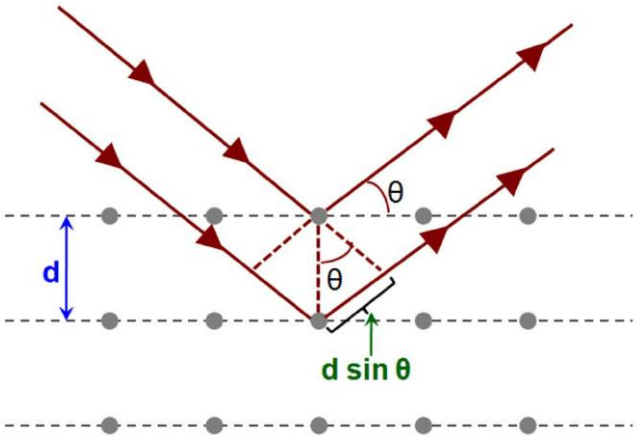


Figure 2.7: X-ray diffraction schematic of 2 dimensional crystal [32].

2.4.2 Raman spectroscopy

Raman spectroscopy is a characterization method obtained from observing low-frequency modes such as vibrational and rotational modes in a system, resulting from an interaction of a monochromatic light with sample's chemical bonds. When photons of the incoming light interact with the molecular vibrations of a sample, they get scattered, and their energy gets altered (increases or decreases). This process leaves the sample with different vibrational states. The energy changes of the scattered beam curate a profile about the vibrational modes of the sample and allow unique identification of samples. This is possible since vibrational frequencies of a sample are specific to the chemical bonds and symmetries within the sample.

Raman spectroscopy consist of different scattering, with one the sample having the same vibrational state before and after the virtual state called Rayleigh scattering is observed, Stokes Raman scattering observed when a system has higher vibrational state after the virtual state and Anti-Stokes scattering occurring when the sample has lower vibrational state than the ground state after virtual state, shown in Figure 2.8 [33].

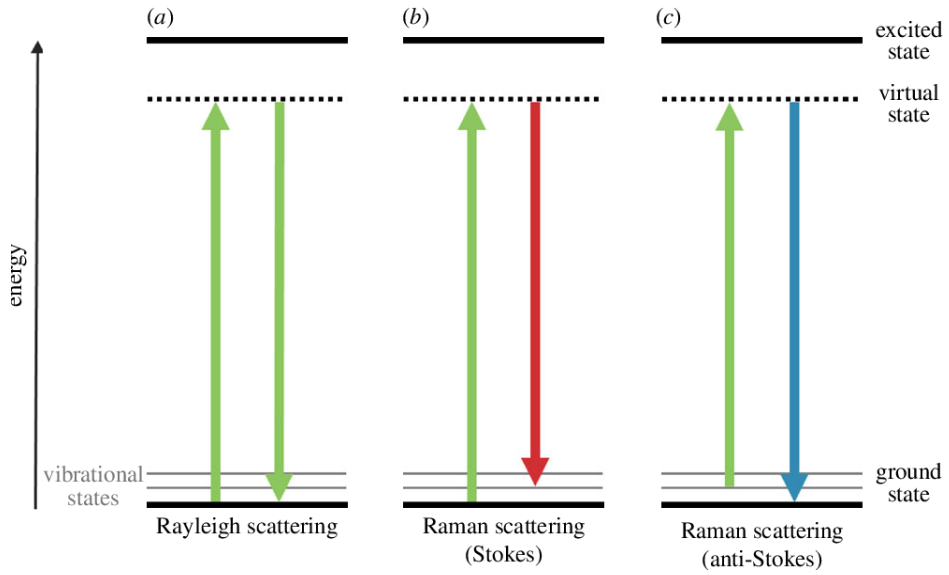


Figure 2.8: Raman scatterings [34].

2.4.3 Transmission electron microscopy (TEM)

Transmission electron microscopy (TEM) forms an image of an ultra-thin sample through the transmitted electrons when there is an incident electron beam [35]. The objective lens of a TEM instrument focuses the beam that penetrate the sample and the projector lens magnify the image onto an image device such as fluorescent screen or couple-charged device (CCD) camera [36]. The common produced images of TEM are called bright field images and are formed by the transmitted electrons. Darker appearing regions formed by reflected or high angle scattered electrons possess higher atomic number or density, and the bright part of the field are formed by the transmitted electrons [37].

2.4.4 High-Resolution Transmission electron microscopy (HRTEM)

High resolution transmission electron microscopy (HRTEM) is a TEM instrument that uses high magnifications and phase difference in electron waves to generate contract, which together allow possibility of observing lattice spacing and grain boundaries of samples. The TEM diagram is displayed in Figure 2.9.

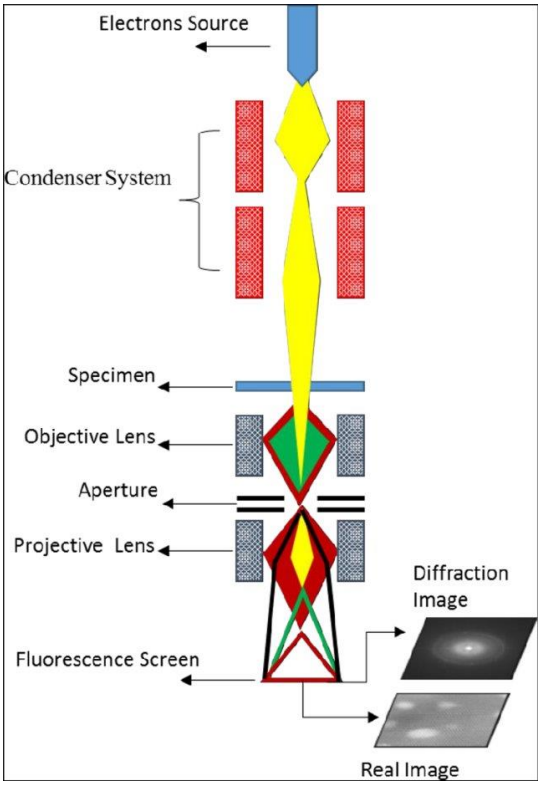


Figure 2.9: Transmission Electron Microscopy working principle [38].

2.4.5 Scanning electron microscopy (SEM)

The scanning electron microscopy technique is utilized for evaluating the morphology of a sample by scanning the sample surface with electrons of relatively low energy. Electron beam interact with the atoms of the sample at a different depth and return secondary and backscattered electrons, which hold insights of the morphology and surface topography of a sample [39]. Figure 2.10 depicts the working principle of SEM imaging. SEM is capable of magnifying samples at 4 - 0.4 mm depth of field and 1 - 10 nm resolution, resulting in 10 - 300 000 times magnification of detailed grey images [40].

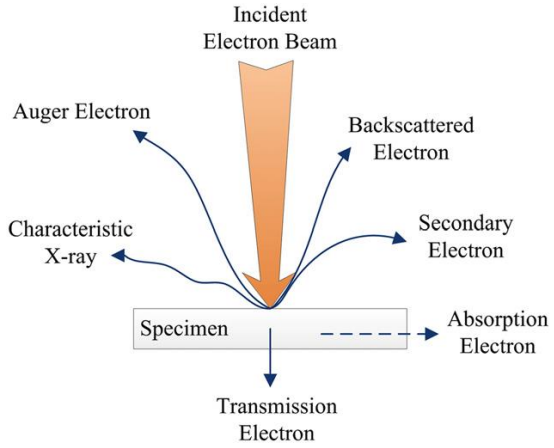


Figure 2.10: Working principle depiction of SEM [41].

2.4.6 Energy dispersive X-ray spectroscopy (EDS)

In a SEM instrument, upon interplay of the electron beam with a sample, the sample gets ionized, and emits X-rays [42]. The produced x-rays reach a crystal (usually Silicon Drift Detector (SDD))

contained at the EDS detector and the detector measure the number of produced x-rays against their energies. The energies of these X-rays form part of the characteristics of the elements that produced them. By calculating the energies of the x-rays, elements contained on the sample can be determined [43]. This calculation forms the qualitative analysis part of the EDS systems. The rate of detection of the characteristics X-rays is utilized for determining the amounts of elements present on the sample and this offers the quantitative analysis part of the EDS [43]. By sweeping electron beam over an area of the sample, X-ray maps of spatial variation of elements in the sample can be determined by the EDS [44]. The EDS working principle is displayed on Figure 2.11.

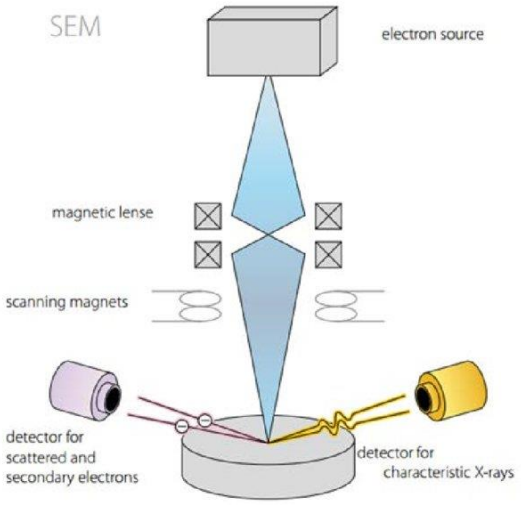


Figure 2.11**:** Working mechanism of EDS [45].

2.4.7 X-ray photoelectron spectroscopy (XPS)

X-ray photoelectron spectroscopy (XPS) is an analytical technique obtained by irradiating a sample with a monochromatic light and observing the resulting photoelectrons emitted from the sample. By focusing an X-ray on a sample, the electrons on the sample's bulk get excited by the

absorbed photons of the X-ray and some of these electrons escape the sample surface, as displayed in Figure 2.12. The valence and types of elements available on the sample can be established by quantifying the kinetic energy of the escaped electrons and calculating their binding energies.

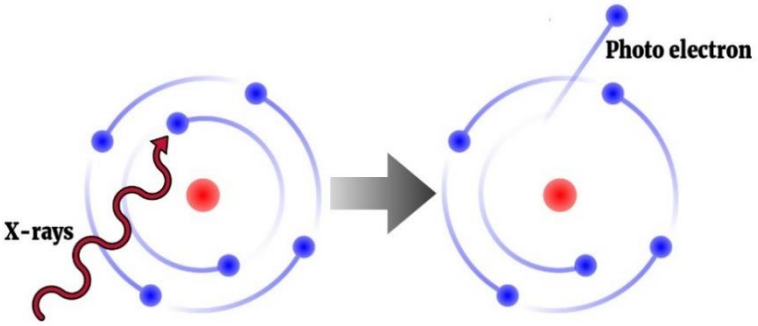


Figure 2.12: Photoelectric effect caused by X-rays.

The XPS spectra of samples is given by plotting the intensity of the emitted electrons against their binding energies [46]. Every element creates a unique set of XPS peaks at characteristic binding energies and this allows XPS to be used for elemental mapping of samples.

2.4.8 Brunauer-Emmett-Teller analysis (BET)

Brunauer-Emmett-Teller analysis (BET) uses physical adsorption of gas to acquire the pore size, pore volume, specific surface area and surface nature of a material. This is achieved by exposing a sample to nitrogen (N_2) gas at different pressures in a cryogenic temperature of liquid nitrogen or argon gas. Increasing the surrounding pressure on the sample forces the N_2 molecules to adsorb on the sample's surface and this process is illustrated on Figure 2.13. By using the pressure that establishes adsorption equilibrium, universal gas law can be employed for calculating the amount

of N_2 gas adsorbed on the sample and for obtaining an adsorption isotherm. Desorption isotherms are obtained by decreasing the surrounding pressure. The resulting adsorption and desorption isotherms from these processes are then used to acquire information about the surface of the sample.

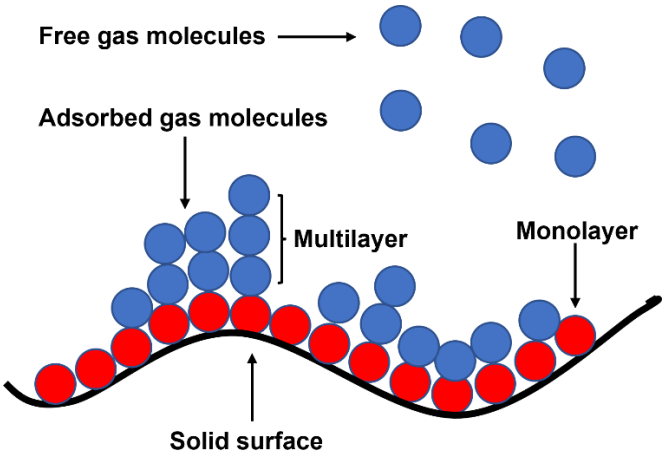


Figure 2.13: BET working principle.

2.4.9 Thermogravimetric analysis (TGA)

Thermogravimetric analysis (TGA) is a method used to evaluate thermal stability and volatile components of a sample by monitoring the weight changes the sample experiences when subjected to a controlled heating rate [47]. Because when exposed to a gaseous environment, many solids react to produce gaseous by-products, an inert gas atmosphere is used in TGA studies, and the resulting gaseous by-products are continually removed. The sample's mass is measured continually in this process, as shown in Figure 2.14. The analysis of the temperature and the associated weight changes offer insights about the thermal decomposition, absorption/desorption and phase transitions [48].

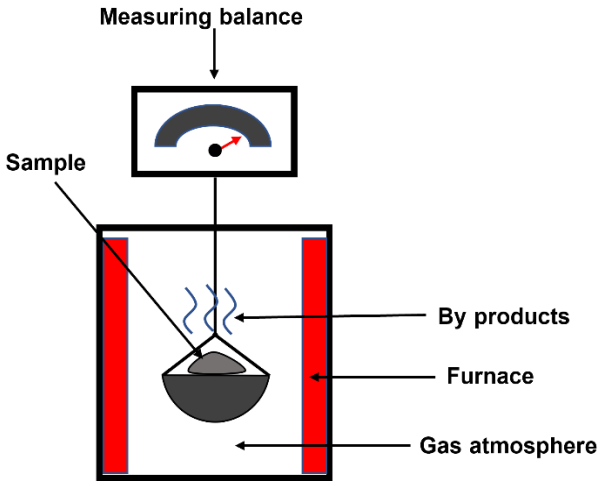


Figure 2.14: Working principle of TGA.

2.5 Electrochemical analyses

2.5.1 Cyclic voltammetry

Potentiostatic techniques consist of using of potential sources (potentiostat) to maintain the potential resulting between reference and counter electrodes, which is subsequently used to control the potential between the working and reference electrode [49]. A common potentiostatic technique used in electrochemical testing is cyclic voltammetry (CV). CV is obtained by cycling the potential of an electrode and then evaluating the resulting current response. The potential difference of the working and reference electrodes during this cycling can be considered as an excitation signal with a triangular waveform seen on Figure 2.15 (a), with the potential varying linearly with time. On the waveform, the potential sweeps between two values are known as switching potentials [50]. The potential on signal increases from an initial value to a peak to complete a forward scan, then switched back to the initial value with a negative slope for the

reverse scan. The commonly observed current response when this potential scan is applied to the electrode is in Figure 2.15 (b).

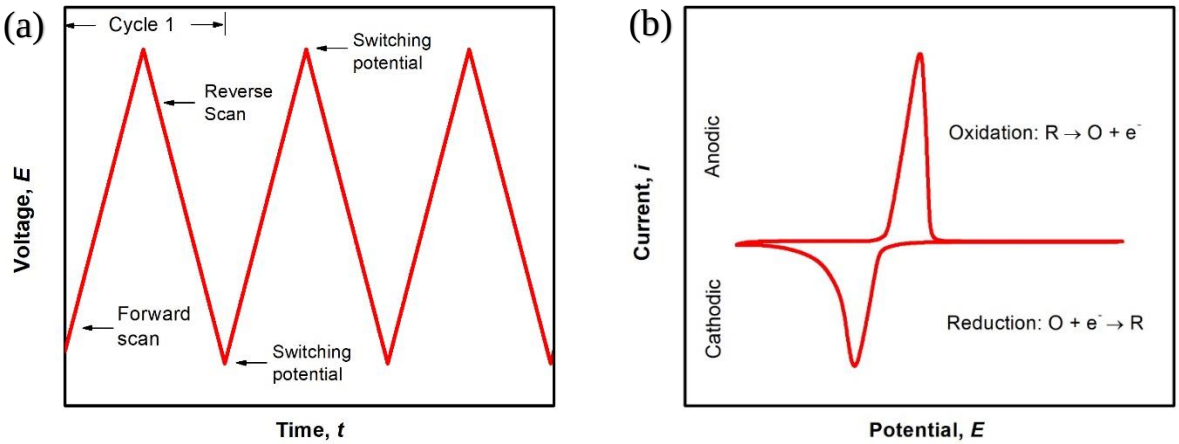


Figure 2.15: (a) Voltage waveform applied in CV, (b) CV curve of potential against current response.

In this figure, when potential increases, the oxidation reaction takes place at the electrode surface, and the anodic current increases. This takes place until the oxidized species run out near the electrode surface, which results in the current reaching the maximum. The current decreases as no further oxidation reaction occurs, and this process completes the forward scan. For the reverse sweep, the reduction reaction occurs, and the cathodic current decreases until all the reduced species at the electrode surface are depleted. The important parameters to extract from the CV voltammogram are: (i) peak-to-peak separation voltage (ΔE_{pp} / V) to study electron transfer kinetics of cells; (ii) the heights of the anodic (I_{pa} / mA) and cathodic (I_{pc}/mA) peak current, which represent the mass transport and redox kinetics, and (iii) the peak current ratio (I_{pa}/I_{pc}), for reversibility of the redox chemistry or the Coulombic efficiency [51].

2.5.2 Electrochemical impedance spectroscopy (EIS)

Electrochemical impedance spectroscopy (EIS) is obtained by applying an alternating voltage in a specific frequency range to an electrode and observing the established alternating current signal. Impedance is then acquired by taking the ratio of the applied AC voltage to the corresponding current response. Impedance can be seen as a frequency-dependent resistance [52]. When AC perturbation is applied to an energy storage system, the individual reaction inside the system possesses different time constants and appears at different frequencies on EIS spectra [53]. This allows the reactions in the system to be separated and modelled using equivalent circuits.

A common Nyquist plot (EIS plot) and the corresponding Randles circuit (equivalent circuit) can be seen in Figure 2.16. This figure contains information about the internal resistance observed at high frequencies with its value obtained from the initial value of the semi-circle. The charge transfer resistance is found at the low frequencies (at the diameter of the semi-circle). The straight line in the low frequencies attributes to a diffusion (Warburg) impedance and if the slope equals to 45° a battery-like behaviour of an electrode is observed, and 90° slope indicates a capacitive behaviour.

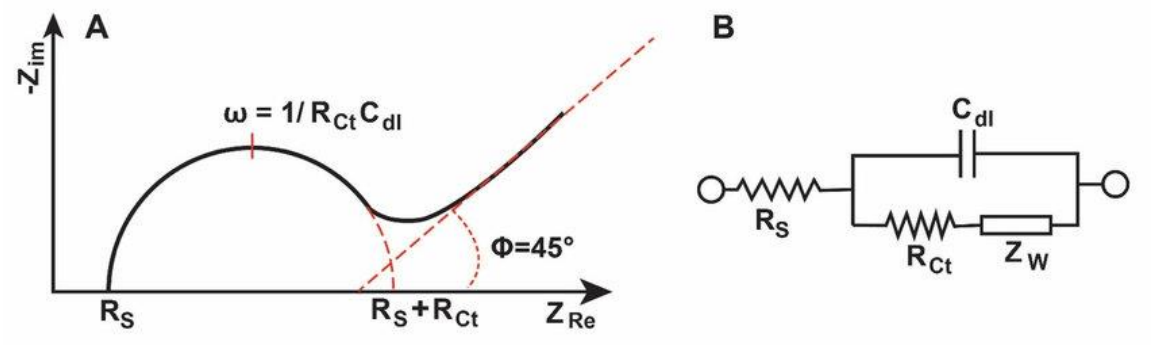


Figure 2.16: Nyquist plot and the equivalent Randles circuit.

2.5.3 Galvanostatic tests

Galvanostatic techniques consist of a galvanostat instrument meant for controlling the current between the working and counter electrode, with a purpose of measuring the resulting potential difference on the working and reference electrode [49]. One of these techniques is galvanostatic charge and discharge (GCD), which comprises of observing a voltage response of an electrode under a constant applied current. To measure GCD, a terminal voltage indicating where the current will be inverted must be determined, and generally, the potential used to sweep the CV voltammograms is utilized for this case. Applied current used in GCD studies of LIBs and LICs is usually quantified with C-rates, where 1C amounts to a current needed to charge/discharge a device to its maximum capacity in an hour. Figure 2.17 (a) demonstrates a common GCD profile of electrode voltage against capacity. Usually, the charge/discharge plateau of GCD curves corresponds to the anodic/cathodic peaks observed on the CV voltammogram.

The number of available charge carriers in a system is limited and observing how they are consumed by side reactions in repeated charge-discharge cycles offers a detailed view of the electrochemical performance. Running charge-discharge cycles several times provides further information about the rate capability, capacity retention , lifespan and stability of an electrode [54]. A rate capability of an electrode is evaluated by subjecting the electrode to different currents at a suitable range. By increasing the current or the C-rate, the capacity of electrodes decreases because of polarization or potential loss, and the observation of this process is seen on Figure 2.17 (b). It is from this interplay between the current and the corresponding electrode's capacity that power and energy outputs of an electrode can be calculated. Electrodes with high-rate capability exhibit

high power performance and ones with low-rate capability have higher energy output. These correlations aid in categorizing the applications for which an electrode is suitable.

In evaluating the coulombic efficiency of an electrode, from the quantity obtained from the charge capacity to discharge capacity ratio, one can assess the electrode's cycle life and stability. Coulombic efficiency (CE) plot is demonstrated in Figure 2.17 (c). Because of the many reactions involved in an energy storage device, CE decreases with time, and the number of cycles obtained until a certain accepted CE percentage can be used to quantify a lifespan and stability of an electrode. Another quantity used to measure the lifetime and stability of an electrode is capacity retention. The number of cycles required to bring the capacity down to 80% of the initial capacity is used to quantify how long an electrode will be efficient in applications.

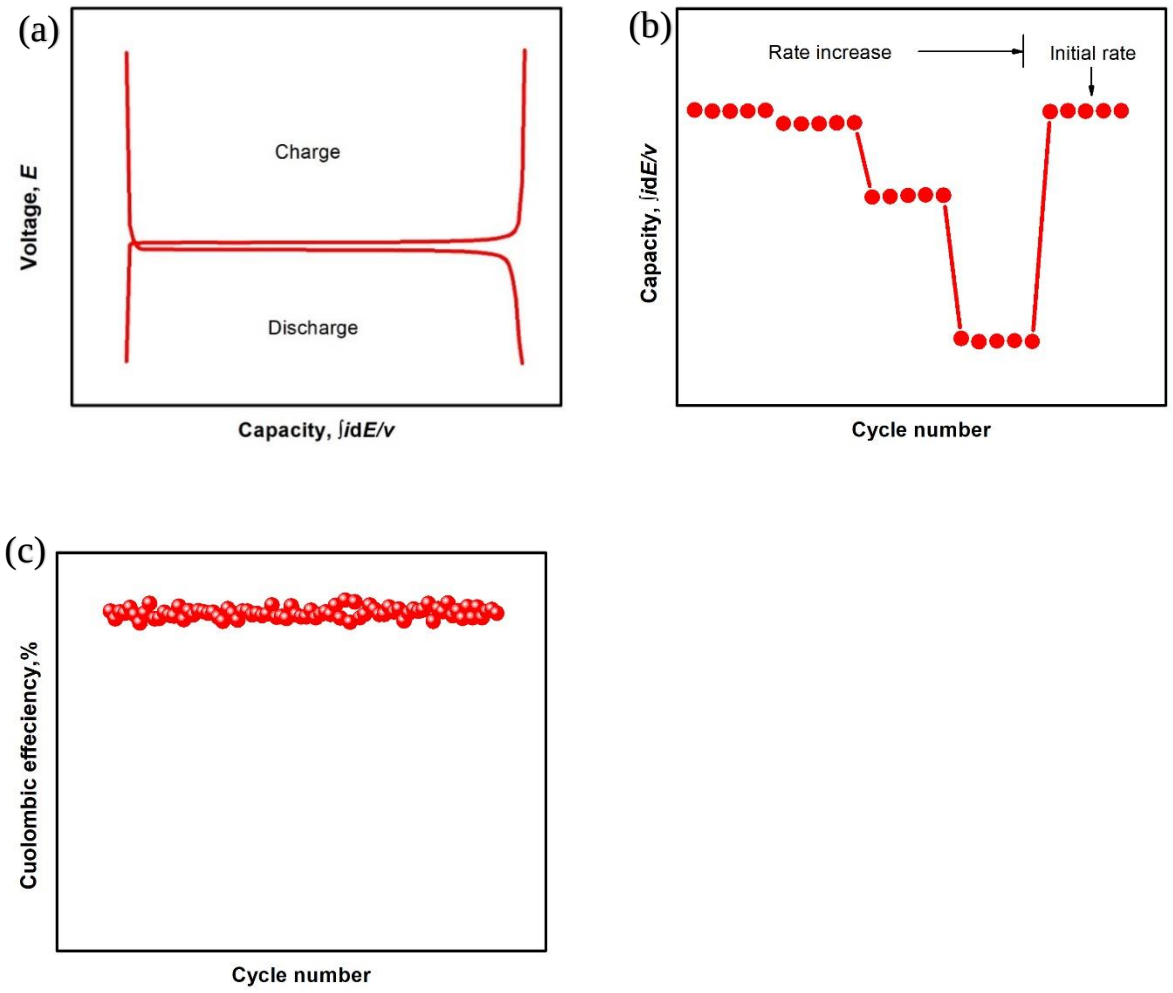


Figure 2.17: (a) Charge and discharge curves, (b) rate capability performance, (c) Coulombic efficiency plot.

2.6 Spinel lithium titanate ($Li_4Ti_5O_{12}$) as an anode in energy systems

2.6.1 Spinel $Li_4Ti_5O_{12}$

The state-of-the art LIBs used in commercial applications such as portable electronic devices use layered structured materials, namely, lithium cobalt oxide ($LiCoO_2$) and graphite. These kinds of materials exhibit high energy density, but the future application of ESSs aims to diversify into elavated power density and long-life cycle. Alternative materials meant to satisfy this diversity of ESSs have been explored and insertion materials have emerged as alternatives. One of the alternatives involves the use of lithium insertion materials having a spinel structure framework. Oxide spinel has the general chemical composition AB_2O_4 where A and B are not crystallographic sites but the constituents, as shown in Figure 2.18 [55, 56]. This chemical formula consists of a cubic close-packed (CCP) arrangement, and one-eight of the A sites (tetrahedral interstices) is filled by oxygen anions while half of B sites (octahedral interstices) is inhabited by cations [57].

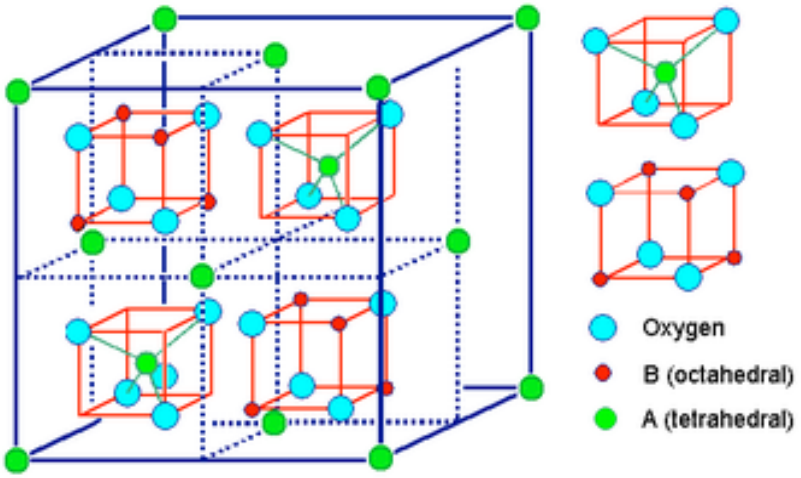


Figure 2.18: Spinel structure diagram [58].

Spinel structures are capable of exhibiting A ions on the octahedral 16(d) sites, filling only one-half of the sites. B ions on the remaining 1/2 of the octahedral 16(d) sites and on all the tetrahedral 8(a) sites. This configuration of ions is called the inverse spinel structure [59] and the formula of $B[AB]O_4$ is used for the representation of this structure. The lithium transition metal oxides with a normal spinel framework are recommended for lithium-ion technology as opposed to the ones with inverse spinel structures. The reason being that the normal spinel consists of 3D channels made up of 1D tunnels of empty octahedral sites, which permit transportation of lithium ions all through the solid matrix, as opposed to the transition metal ions at tetrahedral 8(a) sites of the inverse spinel which block the lithium-ion movement within the structure.

Lithium titanate has a spinel structure with cubic symmetry and an Fd3m space group with 0.8364 nm lattice constant [60]. The Li^+ ions hold the tetrahedral 8a sites, and 1/6 of them are found in the octahedral 16d sites [61]. The Ti^{4+} ions reside in the remaining octahedral sites, with the ratio of Li: Ti being 1:5. And the O^{2-} ions are situated in 32e sites, which means spinel LTO can be described by $Li_{3(8a)}\ [LiTi_5{}^{4+}]_{(16d)}O_{12(32e)}$ in space notation [62]. The vacant sites of the crystal structure are the octahedral 16c, tetrahedral 8b and 48f sites. It is these structural qualities that allow this material to manage to diffuse Li^+ and successfully be an active material of ESSs. The lithium-ion insertion process of the spinel LTO will be discussed in the following section.

2.6.2 Lithium diffusion in $Li_4Ti_5O_{12}$

The $[TiO_6]$ of the LTO spinel structure provides a framework for lithium insertion and extraction. During lithium insertion, when LTO is exposed to voltage range 1-3 V, 3 Li^+ located in 8a sites migrate to the 16c sites and the 3 inserted Li^+ reach the 16c sites using the 8a sites [63, 64]. The 3 Li^+ are extracted out of the LTO framework from 16c using the 8a, and the other 3 migrate back to the 8a sites. During the same process, a redox reaction of Ti^{4+}/Ti^{3+} on the octahedral sites is observed and the occurring phase transition process is shown in equation 2.3 [65]. The process gives rise to a change of spinel $Li_4Ti_5O_{12}$ to a rock structured $Li_7Ti_5O_{12}$ [66], with the structural changes shown in Figure 2.19.

$$Li_{3(8a)}\,[LiTi_5{}^{4+}]_{(16d)}O_{12(32e)} + 3e^- + 3Li^+ \leftrightarrow Li_{6(16c)}\,[LiTi_3{}^{3+}Ti_2{}^{4+}]_{(16d)}O_{4(32e)} \qquad (2.3)$$

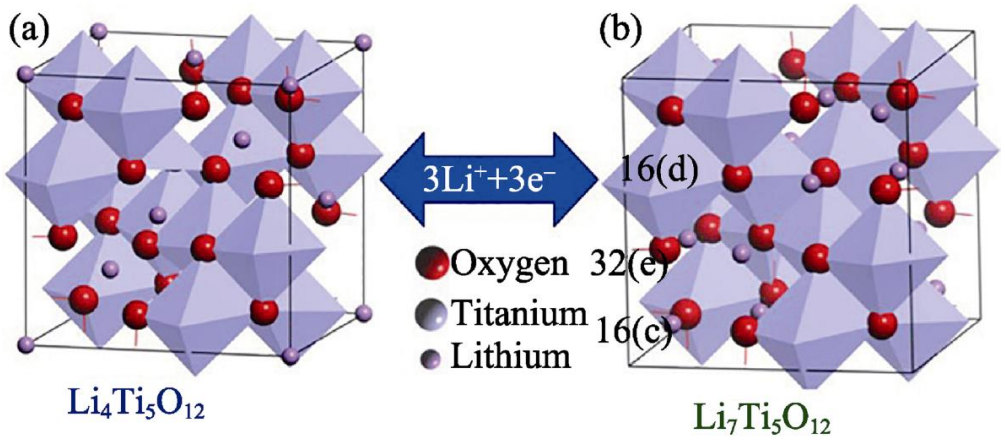


Figure 2.19: (a) LTO in Spinel structure, (b) LTO in rock-salt structure [67].

The change of the phase is distinguished by the voltage plateau at around 1.55 V [62], which is greater than the reduction potential of most electrolytes (0.8 .vs Li^+/Li). This allows LTO electrodes to avoid the emergence of the solid electrolyte interface (SEI) layer. During changes of spinel LTO to rock-salt structure, the material experienced a 0.2-0.3% volume increase and a

0.8364 nm to 0.8353 nm lattice constant decrease [68, 69]. This highlight why the material is considered a zero-strain material. With three Ti^{4+} reduced to Ti^{3+} and a theoretical capacity of 175 $mAhg^{-1}$, throughout the lithium insertion and extraction, the spinel structure remains stable because of the covalent bonds found between Ti and O atoms. Both the exceptional stable structure and minor volume expansion of LTO during lithiation/delithiation, eliminates the capacity degradation and particle fracture.

The studies of LTO are usually conducted above the potential of 1.0 V, but it has been reported that on 1.0–0.01 V (vs. Li^+/Li) range, the rock-salt structure of LTO can insert more Li-ions. It turns out that the octahedral or tetrahedral sites of LTO pose no limit to the lithium intercalation, but the number of tetravalent titanium ions does. This is observed when LTO is cycled in the voltage window 2.5 - 0.01 V. The corresponding theoretical capacity in this range is reported to be 293 $mAhg^{-1,}$ and it is made possible by the rock-salt LTO further accepting 2 mol of Li-ions as result of the two-remaining tetravalent $Ti_2{}^{4+}$ supporting further reduction as shown in Figure 2.20 and illustrated by equation 2.4 [70]. This opens further explorations of using LTO in a high capacity requiring applications.

$$Li_{6(16c)}\,[LiTi_3{}^{3+}Ti_2{}^{4+}]_{(16d)}O_{4(32e)} + 3e^- + 3Li^+ \leftrightarrow Li_{2(8a)}\,Li_{6(16c)}\,[LiTi_3{}^{3+}]_{(16d)}O_{4(32e)} \qquad (2.4)$$

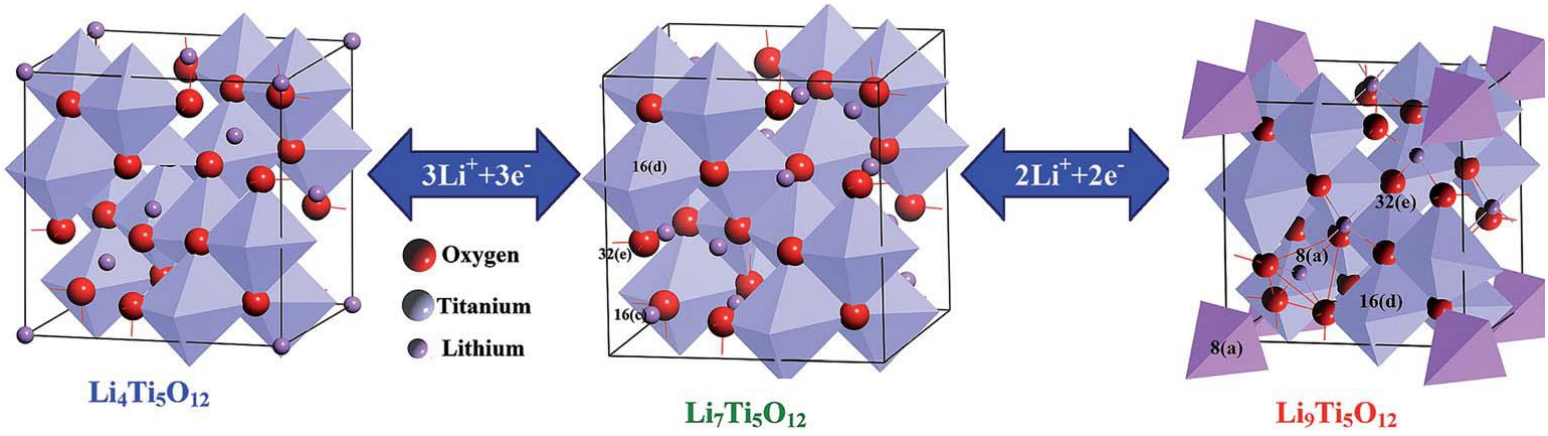


Figure 2.20: Further Li-ion insertion from the rock salt structure [71].

2.6.3 Challenges and mitigation strategies of $Li_4Ti_5O_{12}$ anodes

The potential of LTO being a prominent anode active material for commercial application is still halted by some challenges. LTO has intrinsic kinetic problems emanating from its moderate electronic conductivity and diffusion coefficient [72]. Electronic conductivity refers to the ability of electrode materials to conduct electric current through the movement of electrons and diffusion coefficient measures how quickly lithium ions can move through the electrode materials. These problems hamper the high-rate capabilities of LTO in high power LIBs and LICs meant for large scale applications [73], as these kinds of applications, like EVs, require fast charging and discharging processes [74]. This also hinders its capability as viable anode material in LICs since they are using cathodes made up of capacitive active materials with fast kinetics through adsorption and desorption [75]. The theoretical capacity of 175 $mAhg^{-1}$ (when cycled on 1-3V voltage range) is also a limiting factor to the use of LTO in future applications that requires an anode with a high specific capacity [76].

The solutions to these problems include morphology control, element doping, fast ion conductor modification and surface modification. Morphology controls involve the use of one-dimensional LTO nanorods, nanofiber and nanowires, which have a large surface area and migration pathway of lithium-ions and electrons, which promote better rate and cyclability [73]. Another morphology alteration technique is seen through the utilization of two-dimensional LTO nanosheets, which are more favourable to transfer electrons and Li-ions than 1D nanostructures. A 3D structure is also used to ensure the tight contact between particles and, in turn, effectively restrain the capacity fade. The element doping technique is employed for increasing the inherent electronic conductivity of LTO with the use of dopants such as Na^{+} [77], Mg^{2+} [78], Ca^{2+} [79], Cu^{2+} [80], Sr^{2+} [81], Zn^{2+} [82], Al^{3+} [83], Ce^{3+} [84],Cr^{3+} [85], Zr^{4+} [86], F^{-} [87] and Br^{-} [88] among others.

Fast ion conductor modification involves the creation of LTO composite with materials which have rapid lithium transfer abilities, materials like lithium lanthanum titanates ($Li_{3x}La_{(2/3-x)}TiO_3$) [89] and lithium aluminium oxide ($LiAlO_2$). Surface modification include introduction of carbonaceous materials to increase the conductivity [90, 91], metal oxides to improve cycle performance and specific capacity of LTO [92], and the use of conductive polymers due to their high electrical conductivity, impressive mechanical flexibility and excellent chemical stability [93, 94].

Regardless of the mentioned improvements, LTO still suffers from gas evolutions with gases like carbon monoxide (CO) and hydrogen gas (H_2) produced in LIBs. There is no common conclusion on the cause of this gassing problem in literature, and some researchers attribute this issue to possible trace amount of water found on the cell components (electrodes and electrolyte) and the subsequently formed PF_6 [95]. A plausible explanation behind this postulate is that the working potential of batteries utilizing LTO is adequate for water splitting reactions that produce H_2 gas

[96, 97]. Another postulate linked to the trace of water entails that LTO might be a photocatalyst that promote the water splitting reaction occurring during the production of H_2 [98]. And some found that the trace amount of water promote the hydrolysis of $LiPF_6$ found in the electrolyte, which is in turn reactive to the electrolyte solvents [99].

Others propose that the moisture found in the electrolyte and electrode cannot explain the huge gasses generated. They base this problem on the high catalytic activity of titanium oxides surface that reduces the carbonates found in electrolyte solvents and, in turn, decomposes the electrolyte, which results in gas generation [100]. Most researchers link these hypotheses to the lack of the SEI layer. This absence promotes the occurrence of unwanted reactions on the interface found between LTO and the electrolyte. The common generated gases promoted by these catalyzed interfacial reactions are shown in Figure 2.21. Belharouak et al. [97] quantified the concentrations of these gases by evaluating calendar and cycle life of LMO/LTO cells using 30 °C, 45 °C, and 60 °C for five months, and the results are shown in Figure 2.22.

One of the prominent solutions to this problem involves the use of fluorides for surface modification to limit oxygen evolution reactions, resulting in reduced electrolyte decomposition. Even when the gassing studies of LTO are beyond the scope of this study, the materials utilized for enhancing electrochemical performance of LTO in this study also hold great potential for gassing remedy studies, and the next section will outline cases where these materials enhance the electrochemical performance of various electrodes.

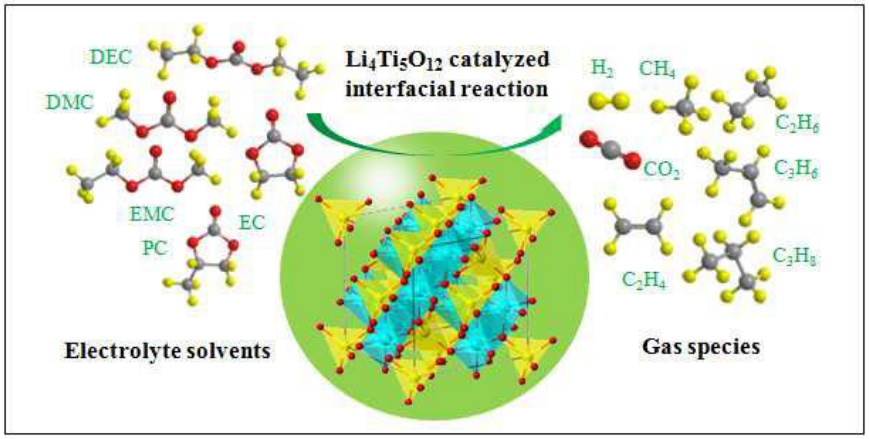


Figure 2.21: Solvents and produced gas species of LTO [95].

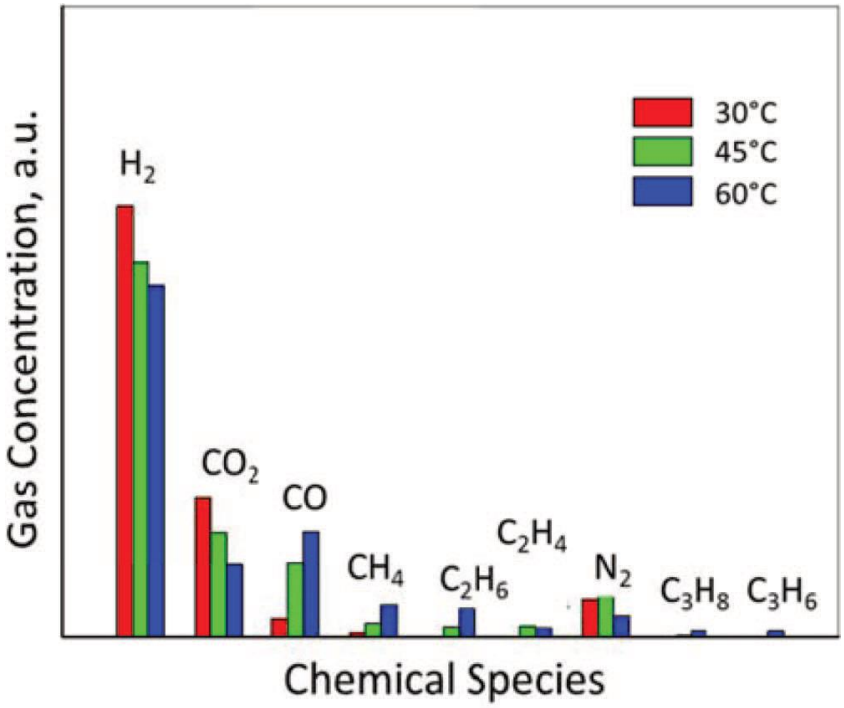


Figure 2.22: Concentration of decomposed chemical species at different temperatures [95].

2.7 Cerium fluoride (CeF_3) coating in electrodes

The demand for energy storage and supply, altogether with whole new applications of ESSs in large scale applications, leads to ESSs being used in applications that utilize many circles, fast charge and discharge, and harsher thermal operating conditions than portable electronic devices conditions. These conditions may lead to unwanted reactions that might damage the device components. For instance, increasing the capacity of cathode material often requires the cathode to be used at a cutoff potential, and this usually leads to oxidative decomposition of electrode and dissolution of active material into the electrolyte comprising of HF [101].

Cycling LTO at elevated temperature results in gas evolutions inside ESS devices. One of the solutions proposed for mitigating these problems includes putting a safeguarding layer on the electrodes surface. A common surface coating or modification technique with the purpose of improving the electrochemistry and stabilizing the surface of electrodes involves the use of metal oxides. But it turns out that metal oxides produce a stable metal fluoride and H_2O, the produced water react with the $LiPF_6$ salt and produces HF which leads to side reactions. Therefore, alternative surface coating materials are needed, and metal fluorides hold great consideration as a result of their electrochemical stability.

To our knowledge, surface modification of electrodes with cerium fluoride (CeF_3) has not been explored much in the literature, especially for anodes. CeF_3 has been used in surface modification of cathode materials for better electrochemistry. Cerium fluoride is utilized in this study because of its high ionic conductivity at room temperature, being chemically inert at high temperature and being stable in an acidic environment. In the work of Lu et al., [102], surface coating $Li_{1.2}Mn_{0.54}Ni_{0.13}Co_{0.13}O_2$ with 2 wt.% of CeF_3 was used to get a high specific capacity of 103.1

mAh g^{-1} compared to 82.2 mAh g^{-1} of the pristine material at a 5 C rate. An elevated capacity retention of 91.7% (about 223 mAh g^{-1} to 204.5 mAh g^{-1}) was obtained after 50 cycles, while pristine material was 82.1% (229.0 mAh g^{-1} to 188.1 mAh g^{-1}). The enhanced performance of the electrode was accredited to the successful suppression of electrolytic corrosion of the electrode by CeF_3 layer.

Another case of successful implementation of CeF_3 modification comes from CeF_3-coated $LiCoO_2$ having achieved a capacity of 160 mAh g^{-1} at 4.6 V vs Li^+/Li cut-off potential compared to the bare and the AlF_3-coated ones with 105 mAh g^{-1} and 155 mAh g^{-1}, respectively, under the same conditions [103]. Under the same study, another observation through the differential scanning calorimetry (DSC) in Figure 2.23 indicates that the MF_3-coated cathode materials (M=Al, Ce) had significantly fewer exothermic activity and a decreased heat production at a high delithiated state, which let them to be more desirable for safety purpose than pristine $LiCoO_2$. These findings were reported to have been as a result of the coated nano-film ability to block the interface reactions between the cathode and the electrolyte.

Xie, Y., *et al.* [104] reported a CeF_3(1 wt%)-coated $LiNi_{1/3}Co_{1/3}Mn_{1/3}O_2$, which delivered a reversible capacity of 107.1 mAh g^{-1} at 5 C rate, compared to pristine with 57.3 mAh g^{-1}. The impedance studies of the pristine, 1 wt.% and 3wt.%-coated NCM, presented a charge transfer resistance of 72.52, 9.18 and 32.19 Ω, respectively at 50 cycles. And charge transfer resistance of 161.50, 41.74 and 69.40 Ω, respectively at 100 cycles. The observed less increase in resistance on the coated materials proved that CeF_3 does offer a safeguarding layer and manages to suppress HF attacks to the cathode active material. The $3.37\times10^{-12}\ cm^2\ s^{-1}$ and $1.02\times10^{-11}\ cm^2\ s^{-1}$ lithium

diffusion coefficients of the pristine and 1wt.% coated NCM indicated the co-doping of either Ce or F into the NCM structure, which promotes a faster Li^+ diffusion.

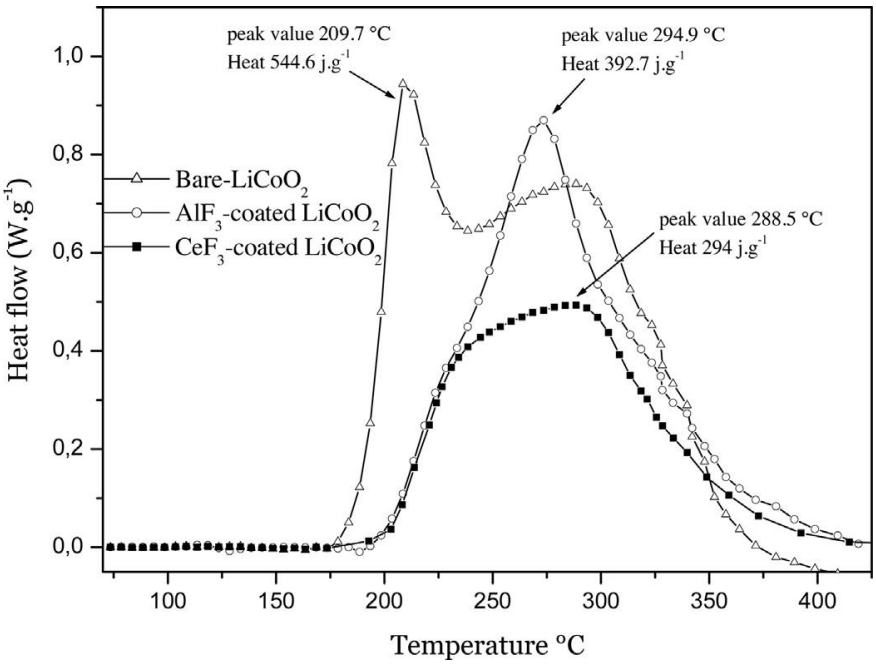


Figure 2.23: DSC plots of the bare-$LiCoO_2$ and coated -$LiCoO_2$ cathodes at fully charged state. [103].

2.8 References

[1] Hemmati, R. & Saboori, H. 2016. Emergence of hybrid energy storage systems in renewable energy and transport applications–A review. *Renewable Sustainable Energy Reviews,* 65**,** 11-23.

[2] Baig, M.M., Gul, I.H., Baig, S.M. & Shahzad, F. 2021. The complementary advanced characterization and electrochemical techniques for electrode materials for supercapacitors. *Journal of Energy Storage,* 44**,** 103370.

[3] Scrosati, B. 2000. Recent advances in lithium ion battery materials. *Electrochimica Acta,* 45**,** 2461-2466.

[4] Karimi, D., Khaleghi, S., Behi, H., Beheshti, H., Hosen, M.S., Akbarzadeh, M., Van Mierlo, J. & Berecibar, M. 2021. Lithium-Ion Capacitor Lifetime Extension through an Optimal Thermal Management System for Smart Grid Applications. *Energies,* 14**,** 2907.

[5] Jin, L., Gong, R., Zhang, W., Xiang, Y., Zheng, J., Xiang, Z., Zhang, C., Xia, Y. & Zheng, J.P. 2019. Toward high energy-density and long cycling-lifespan lithium ion capacitors: a 3D carbon modified low-potential Li 2 TiSiO 5 anode coupled with a lignin-derived activated carbon cathode. *Journal of materials chemistry A,* 7**,** 8234-8244.

[6] Sasikala, S.P., Jeong, G.H., Yun, T. & Kim, S.O.J.E.S.M. 2019. A perspective on R&D status of energy storage systems in South Korea. 23**,** 154-158.

[7] Brenni, P., Galdi, R., Pietra, F. & Savini, A. From Volta onwards: A variety of electrical batteries in the Pavia Museum of Electrical Technology. 2012 Third IEEE HISTory of ELectro-technology CONference (HISTELCON), 2012. IEEE, 1-6.

[8] Woehrle, T. 2018. Lithium-ion cell. *Lithium-ion batteries: Basics and applications.* Springer.

[9] Whittingham, M.S. & Gamble Jr, F.R. 1975. The lithium intercalates of the transition metal dichalcogenides. *Materials research bulletin,* 10**,** 363-371.

[10] Manthiram, A. 2020. A reflection on lithium-ion battery cathode chemistry. *Nature communications,* 11**,** 1-9.

[11] Tarascon, J.M. & Armand, M. 2011. Issues and challenges facing rechargeable lithium batteries. *Materials for sustainable energy: a collection of peer-reviewed research review articles from Nature Publishing Group***,** 171-179.

[12] Wang, Y., Yi, J. & Xia, Y. 2012. Recent progress in aqueous lithium-ion batteries. *Advanced Energy Materials,* 2**,** 830-840.

[13] Afif, A., Rahman, S.M., Azad, A.T., Zaini, J., Islan, M.A. & Azad, A.K. 2019. Advanced materials and technologies for hybrid supercapacitors for energy storage–A review. *Journal of Energy Storage,* 25**,** 100852.

[14] Han, P., Xu, G., Han, X., Zhao, J., Zhou, X. & Cui, G. 2018. Lithium ion capacitors in organic electrolyte system: scientific problems, material development, and key technologies. *Advanced Energy Materials,* 8**,** 1801243.

[15] Dong, S., Lv, N., Wu, Y., Zhu, G. & Dong, X. 2021. Lithium-Ion and Sodium-Ion Hybrid Capacitors: From Insertion-Type Materials Design to Devices Construction. *Advanced Functional Materials,* 31**,** 2100455.

[16] Amatucci, G.G., Badway, F., Du Pasquier, A. & Zheng, T. 2001. An asymmetric hybrid nonaqueous energy storage cell. *Journal of the Electrochemical Society,* 148**,** A930.

[17] Goodenough, J.B. & Park, K.S. 2013. The Li-ion rechargeable battery: a perspective. *Journal of the American Chemical Society,* 135**,** 1167-1176.

[18] Nzabahimana, J., Liu, Z., Guo, S., Wang, L. & Hu, X. 2020. Top-down synthesis of silicon/carbon composite anode materials for lithium-ion batteries: mechanical milling and etching. *ChemSusChem,* 13**,** 1923-1946.

[19] Lochala, J.A., Zhang, H., Wang, Y., Okolo, O., Li, X. & Xiao, J. 2017. Practical Challenges in Employing Graphene for Lithium-Ion Batteries and Beyond. *Small Methods,* 1**,** 1700099.

[20] Lagadec, M.F., Zahn, R. & Wood, V. 2019. Characterization and performance evaluation of lithium-ion battery separators. *Nature Energy,* 4**,** 16-25.

[21] Wang, Q., Mao, B., Stoliarov, S.I. & Sun, J. 2019. A review of lithium ion battery failure mechanisms and fire prevention strategies. *Progress in Energy Combustion Science,* 73**,** 95-131.

[22] Chawla, N., Bharti, N. & Singh, S. 2019. Recent advances in non-flammable electrolytes for safer lithium-ion batteries. *Batteries,* 5**,** 19.

[23] Sarjeant, W.J., Zirnheld, J., Macdougall, F.W., Bowers, J., Clark, N., Clelland, I., Price, R., Hudis, M., Kohlberg, I. & Mcduff, G. 1999. Capacitors—past, present, and future. *Handbook of Low and High Dielectric Constant Materials and Their Applications.* Elsevier.

[24] Madabattula, G. & Kumar, S. 2018. Insights into charge-redistribution in double layer capacitors. *Journal of The Electrochemical Society,* 165**,** A636.

[25] Li, G., Yang, Z., Yin, Z., Guo, H., Wang, Z., Yan, G., Liu, Y., Li, L. & Wang, J. 2019. Non-aqueous dual-carbon lithium-ion capacitors: a review. *Journal of Materials Chemistry A,* 7**,** 15541-15563.

[26] Wang, X., Liu, L. & Niu, Z. 2019. Carbon-based materials for lithium-ion capacitors. *Materials Chemistry Frontiers,* 3**,** 1265-1279.

[27] Li, B., Zheng, J., Zhang, H., Jin, L., Yang, D., Lv, H., Shen, C., Shellikeri, A., Zheng, Y. & Gong, R. 2018. Electrode materials, electrolytes, and challenges in nonaqueous lithium-ion capacitors. *Advanced materials,* 30**,** 1705670.

[28] Jagadale, A., Zhou, X., Xiong, R., Dubal, D.P., Xu, J. & Yang, S. 2019. Lithium ion capacitors (LICs): Development of the materials. *Energy Storage Materials,* 19**,** 314-329.

[29] Wang, H., Zhu, C., Chao, D., Yan, Q. & Fan, H.J. 2017. Nonaqueous hybrid lithium-ion and sodium-ion capacitors. *Advanced materials,* 29**,** 1702093.

[30] Bunaciu, A.A., Udriştioiu, E.G. & Aboul-Enein, H.Y. 2015. X-ray diffraction: instrumentation and applications. *Critical reviews in analytical chemistry,* 45**,** 289-299.

[31] Chatterjee, A.K. 2000. X-ray diffraction. *Handbook of analytical techniques in concrete science and technology***,** 275-332.

[32] Baskaran, S. 2010. *Structure and regulation of yeast glycogen synthase.* Doctoral dissertation.

[33] Lyon, L.A., Keating, C.D., Fox, A.P., Baker, B.E., He, L., Nicewarner, S.R., Mulvaney, S.P. & Natan, M.J. 1998. Raman spectroscopy. *Analytical Chemistry,* 70**,** 341-362.

[34] Moura, C.C., Tare, R.S., Oreffo, R.O. & Mahajan, S. 2016. Raman spectroscopy and coherent anti-Stokes Raman scattering imaging: prospective tools for monitoring skeletal cells and skeletal regeneration. *Journal of The Royal Society Interface,* 13**,** 20160182.

[35] Ma, H., Shieh, K.J. & Qiao, T.X. 2006. Study of transmission electron microscopy (TEM) and scanning electron microscopy (SEM). *Nat Sci,* 4**,** 14-22.

[36] Ayub, B., Wani, H., Shoukat, S., Para, P.A., Ganguly, S. & Ali, M. 2017. Specimen preparation for electron microscopy: an overview. *Journal of Environment Life Sciences,* 2**,** 85-88.

[37] Loos, J., Sourty, E., Lu, K., De With, G. & V. Bavel, S. 2009. Imaging Polymer Systems with High-Angle Annular Dark Field Scanning Transmission Electron Microscopy (HAADF− STEM). *Macromolecules,* 42**,** 2581-2586.

[38] Flemban, T.H. 2017. *High quality zinc oxide thin films and nanostructures prepared by pulsed laser deposition for photodetectors.*

[39] Zhou, W. & Wang, Z.L. 2007. *Scanning microscopy for nanotechnology: techniques and applications*, Springer science & business media.

[40] Hidayanti, F. & Harnovan, A.A. APPLICATION OF SCANNING ELECTRON MICROSCOPY: A REVIEW.

[41] Zhu, F.Y., Wang, Q.-Q., Zhang, X.S., Hu, W., Zhao, X. & Zhang, H.X. 2014. 3D nanostructure reconstruction based on the SEM imaging principle, and applications. *Nanotechnology*, 25**,** 185705.

[42] Wirth, R. 2009. Focused Ion Beam (FIB) combined with SEM and TEM: Advanced analytical tools for studies of chemical composition, microstructure and crystal structure in geomaterials on a nanometre scale. *Chemical Geology*, 261**,** 217-229.

[43] Bergstrom, J.S. 2015. *Mechanics of solid polymers: theory and computational modeling*, William Andrew.

[44] Vzorcev, R.S.I.S.D.J.M.I.T. 2019. DO THE LATEST SCANNING ELECTRON MICROSCOPES WITH A VARIETY OF ANALYTICAL AND IMAGING TECHNIQUES PROVIDE US WITH REALISTIC IMAGES AND COMPOSITIONS? 53**,** 929-936.

[45] Piccinotti, D. 2018. *Chalcogenide platforms for photonic metamaterials*. University of Southampton.

[46] Sudhanshu, R. X-RAY PHOTOELECTRON SPECTROSCOPY (XPS) TECHNOLOGY.

[47] Rajisha, K., Deepa, B., Pothan, L. & Thomas, S. 2011. Thermomechanical and spectroscopic characterization of natural fibre composites. *Interface Engineering of Natural Fibre Composites for Maximum Performance***,** 241-274.

[48] Netzsch. *Thermogravimetric Analysis (TGA)* [Online]. Available: https://www.netzsch-thermal-analysis.com/es/industrias-sectores/methods/thermogravimetric-analysis/ [Accessed].

[49] Bansod, B., Kumar, T., Thakur, R., Rana, S. & Singh, I. 2017. A review on various electrochemical techniques for heavy metal ions detection with different sensing platforms. *Biosensors and Bioelectronics,* 94**,** 443-455.

[50] Elgrishi, N., Rountree, K.J., Mccarthy, B.D., Rountree, E.S., Eisenhart, T.T. & Dempsey, J.L. 2018. A practical beginner's guide to cyclic voltammetry. *Journal of chemical education,* 95**,** 197-206.

[51] Haruna, A.B. 2020. *Rational design synthesis and optimization of manganese-based cathode materials for lithium-ion batteries.*

[52] Günter, F.J., Habedank, J.B., Schreiner, D., Neuwirth, T., Gilles, R. & Reinhart, G. 2018. Introduction to electrochemical impedance spectroscopy as a measurement method for the wetting degree of lithium-ion cells. *Journal of The Electrochemical Society,* 165**,** A3249.

[53] Ratnakumar, B., Smart, M. & Surampudi, S. Electrochemical impedance spectroscopy and its applications to lithium ion cells. Seventeenth Annual Battery Conference on Applications and Advances. Proceedings of Conference (Cat. No. 02TH8576), 2002. IEEE, 273-277.

[54] Yang, X. & Rogach, A.L. 2019. Electrochemical techniques in battery research: a tutorial for nonelectrochemists. *Advanced Energy Materials,* 9**,** 1900747.

[55] Bosi, F., HåLenius, U. & Skogby, H. 2009. Crystal chemistry of the magnetite-ulvospinel series. *American Mineralogist,* 94**,** 181-189.

[56] Spivakov, A.A., Lin, C.R., Lin, E.S., Chen, Y.Z. & Tseng, Y.T. 2021. Preparation and Magnetic Properties of Cobalt-Doped FeMn2O4 Spinel Nanoparticles. *Nanoscale Research Letters,* 16**,** 1-7.

[57] Gao, H., Ma, C. & Sun, B. 2014. Preparation and characterization of NiMn 2 O 4 negative temperature coefficient ceramics by solid-state coordination reaction. *Journal of Materials Science: Materials in Electronics,* 25**,** 3990-3995.

[58] Mulder, M. 2016. *Synthesis of LiNi0. 5Mn1. 5O4 nanofibers by electrospinning.* University of Twente.

[59] Reusser, E., Gieré, R. & Lumpkin, G.R. 2001. Geikielite exsolution in spinel. *American Mineralogist,* 86**,** 1435-1446.

[60] Li, X.Y., Chen, Q.L., Yang, M., Li, Y.N. & Ma, J.B. 2019. Recent Developments in the Effects of Different Dopants on the Structure and Property of Lithium Titanate Material. *Nano,* 14**,** 1930002.

[61] Julien, C. & Zaghib, K. 2004. Electrochemistry and local structure of nano-sized Li4/3Me5/3O4 (MeMn, Ti) spinels. *Electrochimica acta,* 50**,** 411-416.

[62] Yan, H., Zhang, D., Duo, X. & Sheng, X. 2021. A review of spinel lithium titanate (Li4Ti5O12) as electrode material for advanced energy storage devices. *Ceramics International,* 47**,** 5870-5895.

[63] Chiu, H.C., Lu, X., Zhou, J., Gu, L., Reid, J., Gauvin, R., Zaghib, K. & Demopoulos, G.P. 2017. Capacity fade mechanism of Li4Ti5O12 nanosheet anode. *Advanced Energy Materials,* 7**,** 1601825.

[64] Kataoka, K., Takahashi, Y., Kijima, N., Hayakawa, H., Akimoto, J. & Ohshima, K.I. 2009. A single-crystal study of the electrochemically Li-ion intercalated spinel-type Li4Ti5O12. *Solid State Ionics,* 180**,** 631-635.

[65] Li, C. & Mao, J. 2021. Ex-situ study on the structure changes of Li4Ti5O12-based anode materials under different lithium insertion amounts. *Journal of Solid State Chemistry,* 296**,** 121974.

[66] Verde, M.G., Baggetto, L., Balke, N., Veith, G.M., Seo, J.K., Wang, Z. & Meng, Y.S. 2016. Elucidating the phase transformation of Li4Ti5O12 lithiation at the nanoscale. *ACS nano,* 10**,** 4312-4321.

[67] Yi, T. & Bing, X. 2018. Research progress on lithium titanate as anode material in lithium-ion battery. *Journal of Inorganic Materials,* 33**,** 475-482.

[68] Ohzuku, T., Ueda, A. & Yamamoto, N. 1995. Zero-strain insertion material of Li [Li1/3Ti5/3] O 4 for rechargeable lithium cells. *Journal of the Electrochemical Society,* 142**,** 1431.

[69] Ma, J., Wang, C. & Wroblewski, S. 2007. Kinetic characteristics of mixed conductive electrodes for lithium ion batteries. *Journal of Power Sources,* 164**,** 849-856.

[70] Krajewski, M., Hamankiewicz, B., Michalska, M., Andrzejczuk, M., Lipinska, L. & Czerwinski, A. 2017. Electrochemical properties of lithium–titanium oxide, modified with Ag–Cu particles, as a negative electrode for lithium-ion batteries. *RSC advances,* 7**,** 52151-52164.

[71] Yi, T.F., Yang, S.Y. & Xie, Y. 2015. Recent advances of Li 4 Ti 5 O 12 as a promising next generation anode material for high power lithium-ion batteries. *Journal of Materials Chemistry A,* 3**,** 5750-5777.

[72] Khan, F., Oh, M. & Kim, J.H. 2019. N-functionalized graphene quantum dots: Charge transporting layer for high-rate and durable Li4Ti5O12-based Li-ion battery. *Chemical Engineering Journal,* 369**,** 1024-1033.

[73] Yi, T.F., Wei, T.T., Li, Y., He, Y.B. & Wang, Z.B. 2020. Efforts on enhancing the Li-ion diffusion coefficient and electronic conductivity of titanate-based anode materials for advanced Li-ion batteries. *Energy Storage Materials,* 26**,** 165-197.

[74] Deng, J., Bae, C., Denlinger, A. & Miller, T. 2020. Electric vehicles batteries: requirements and challenges. *Joule,* 4**,** 511-515.

[75] Zou, K., Cai, P., Wang, B., Liu, C., Li, J., Qiu, T., Zou, G., Hou, H. & Ji, X. 2020. Insights into enhanced capacitive behavior of carbon cathode for lithium ion capacitors: the coupling of pore size and graphitization engineering. *Nano-micro letters,* 12**,** 1-19.

[76] Li, D., Zhang, X., Miao, X., Liu, Y., Chen, S., Chen, Y., Wang, W. & Zhang, Y. 2019. Solid-state synthesized Li4Ti5O12 for ultrafast lithium ion storage enabled by carbon-coating induced particle size tailoring. *Journal of Alloys Compounds,* 797**,** 1258-1267.

[77] Kim, H.K. & Lee, S.H.J.E. 2016. Enhanced electrochemical performances of cylindrical hybrid supercapacitors using activated carbon/Li4-xMxTi5-yNyO12 (M= Na, N= V, Mn) electrodes. 109**,** 506-511.

[78] Cho, H., Son, H., Kim, D., Lee, M., Boateng, S., Han, H., Kim, K.M., Kim, S., Choi, H. & Song, T. 2017. Impact of Mg-doping site control in the performance of Li4Ti5O12 Li-ion battery anode: first-principles predictions and experimental verifications. *The Journal of Physical Chemistry C,* 121**,** 14994-15001.

[79] Zhang, Q. & Li, X. 2013. Improving the Energy Density of Ca-Doped Li4Ti5O12 Through Discharging to 0 V Cut-off Voltage. *Int. J. Electrochem. Sci,* 8**,** 9734-9740.

[80] Deng, X., Li, W., Zhu, M., Xiong, D. & He, M. 2021. Synthesis of Cu-doped Li4Ti5O12 anode materials with a porous structure for advanced electrochemical energy storage: Lithium-ion batteries. *Solid State Ionics,* 364**,** 115614.

[81] Wu, H., Chang, S., Liu, X., Yu, L., Wang, G., Cao, D., Zhang, Y., Yang, B. & She, P. 2013. Sr-doped Li4Ti5O12 as the anode material for lithium-ion batteries. *Solid State Ionics*, 232**,** 13-18.

[82] Ji, X., Lu, Q., Guo, E., Li, D., Yao, L., Liu, H. & Li, X. 2018. Bamboo-shaped Zn2+-doped Li4Ti5O12 nanofibers: one-step controllable synthesis and high-performance lithium-ion batteries. *Journal of The Electrochemical Society,* 165**,** A534.

[83] Sohib, A., Priyono, S., Widayatno, W.B., Subhan, A., Sari, S.N., Wismogroho, A.S., Hudaya, C. & Prihandoko, B. 2020. Electrochemical performance of low concentration Al doped-lithium titanate anode synthesized via sol-gel for lithium ion capacitor applications. *Journal of Energy Storage,* 29**,** 101480.

[84] Ji, X., Li, D., Lu, Q., Guo, E. & Yao, L. 2017. Electrospinning preparation of one-dimensional Ce 3+-doped Li 4 Ti 5 O 12 sub-microbelts for high-performance lithium-ion batteries. *Journal of Nanoparticle Research,* 19**,** 1-13.

[85] Gong, S.H., Lee, J.H., Chun, D.W., Bae, J.H., Kim, S.C., Yu, S., Nahm, S. & Kim, H.S. 2021. Effects of Cr doping on structural and electrochemical properties of Li4Ti5O12 nanostructure for sodium-ion battery anode. *Journal of Energy Chemistry,* 59**,** 465-472.

[86] Hou, L., Qin, X., Gao, X., Guo, T., Li, X. & Li, J. 2019. Zr-doped Li4Ti5O12 anode materials with high specific capacity for lithium-ion batteries. *Journal of Alloys Compounds,* 774**,** 38-45.

[87] Ma, Y., Ding, B., Ji, G. & Lee, J.Y. 2013. Carbon-encapsulated F-doped Li4Ti5O12 as a high rate anode material for Li+ batteries. *ACS nano,* 7**,** 10870-10878.

[88] Du, G., Sharma, N., Peterson, V.K., Kimpton, J.A., Jia, D. & Guo, Z. 2011. Br-doped Li4Ti5O12 and composite TiO2 anodes for Li-ion batteries: Synchrotron X-ray and in situ neutron diffraction studies. *Advanced Functional Materials,* 21**,** 3990-3997.

[89] Yi, T.F., Yang, S.Y., Tao, M., Xie, Y., Zhu, Y.R. & Zhu, R.S.J.E.A. 2014. Synthesis and application of a novel Li4Ti5O12 composite as anode material with enhanced fast charge-discharge performance for lithium-ion battery. 134**,** 377-383.

[90] Cheng, L., Li, X.L., Liu, H.J., Xiong, H.M., Zhang, P.W. & Xia, Y.Y. 2007. Carbon-coated Li4Ti5O12 as a high rate electrode material for Li-ion intercalation. *Journal of the Electrochemical Society,* 154**,** A692.

[91] Ding, S., Jiang, Z., Gu, J., Zhang, H., Cai, J. & Wang, D. 2021. Carbon-coated lithium titanate: effect of carbon precursor addition processes on the electrochemical performance. *Frontiers of Chemical Science Engineering,* 15**,** 148-155.

[92] Jin, Y., Yu, H., Gao, Y., He, X., White, T.A. & Liang, X. 2019. Li4Ti5O12 coated with ultrathin aluminum-doped zinc oxide films as an anode material for lithium-ion batteries. *Journal of Power Sources,* 436**,** 226859.

[93] Lu, H., Hagberg, J., Lindbergh, G. & Cornell, A. 2017. Li4Ti5O12 flexible, lightweight electrodes based on cellulose nanofibrils as binder and carbon fibers as current collectors for Li-ion batteries. *Nano Energy,* 39**,** 140-150.

[94] Islam, J., Chowdhury, F.I., Raza, W., Qi, X., Rahman, M.R., Das, J., Uddin, J. & Zabed, H.M. 2021. Toward polymer composites based and architectural engineering induced flexible electrodes for lithium-ion batteries. *Renewable Sustainable Energy Reviews,* 148**,** 111302.

[95] Han, C., He, Y.B., Liu, M., Li, B., Yang, Q.H., Wong, C.P. & Kang, F. 2017. A review of gassing behavior in Li 4 Ti 5 O 12-based lithium ion batteries. *Journal of Materials Chemistry A,* 5**,** 6368-6381.

[96] Bernhard, R., Meini, S. & Gasteiger, H.A. 2014. On-line electrochemical mass spectrometry investigations on the gassing behavior of Li4Ti5O12 electrodes and its origins. *Journal of the Electrochemical Society,* 161**,** A497.

[97] Belharouak, I., Koenig, G.M., Tan, T., Yumoto, H., Ota, N. & Amine, K. 2012. Performance degradation and gassing of Li4Ti5O12/LiMn2O4 lithium-ion cells. *Journal of the electrochemical society,* 159**,** A1165.

[98] Khan, S.U., Al-Shahry, M. & Ingler Jr, W.B. 2002. Efficient photochemical water splitting by a chemically modified n-TiO2. *science,* 297**,** 2243-2245.

[99] Verma, P., Maire, P. & Novák, P.J.E.A. 2010. A review of the features and analyses of the solid electrolyte interphase in Li-ion batteries. 55**,** 6332-6341.

[100] Ghosh, A. & Ghamouss, F. 2020. Role of Electrolytes in the Stability and Safety of Lithium Titanate-Based Batteries. *Frontiers in Materials,* 7**,** 186.

[101] Wagner, R., Streipert, B., Kraft, V., Reyes Jiménez, A., Röser, S., Kasnatscheew, J., Gallus, D.R., Börner, M., Mayer, C. & Arlinghaus, H.F.J.a.M.I. 2016. Counterintuitive role of magnesium salts as effective electrolyte additives for high voltage lithium-ion batteries. 3**,** 1600096.

[102] Lu, C., Wu, H., Zhang, Y., Liu, H., Chen, B., Wu, N. & Wang, S. 2014. Cerium fluoride coated layered oxide Li1. 2Mn0. 54Ni0. 13Co0. 13O2 as cathode materials with improved electrochemical performance for lithium ion batteries. *Journal of Power Sources,* 267**,** 682-691.

[103] Aboulaich, A., Ouzaouit, K., Faqir, H., Kaddami, A., Benzakour, I. & Akalay, I. 2016. Improving thermal and electrochemical performances of LiCoO2 cathode at high cut-off charge potentials by MF3 (M= Ce, Al) coating. *Materials Research Bulletin,* 73**,** 362-368.

[104] Xie, Y., Gao, D., Zhang, L., Chen, J., Cheng, S. & Xiang, H. 2016. CeF3-modified LiNi1/3Co1/3Mn1/3O2 cathode material for high-voltage Li-ion batteries. *Ceramics International,* 42**,** 14587-14594.

Chapter 3

Experimental section

3.1 Materials and Chemicals

Lithium titanium oxide (LTO) and styrene-butadiene rubber (SBR) were supplied by Gelon LIB group (China). Cerium nitrate hexahydrate ($Ce(NO_3)_3 \cdot 6H_2O$, 99%) and ammonium fluoride (NH_3F, ≥ 98%) were purchased from Sigma-Aldrich (South Africa). Lithium hexafluorophosphate ($LiPF_6$), diethyl carbonate (DEC) $OC(OCH_2CH_3)_2$, dimethyl carbonate (DMC) $OC(OCH_3)_2$ and ethylene carbonate (EC) $(CH_2O)_2CO$ were purchased from Dongguan Shanshan Battery Materials Co. Ltd (China). Pure argon (Ar, 99.998 %) was supplied by Afrox (South Africa), Carbon black (Timical Super C45) was purchased from MTI Corp, carboxymethyl cellulose (CMC) was purchased from China, and grade GD 1UM 47 mm whatman paper. All the chemicals were used as received.

3.2 Synthesis of materials

3.2.1 Syntheses of electrode materials

The LTO anodes were constructed with active material, carbon black super C45, CMC and SBR of 85, 10, 2.5 and 2.5 wt%, respectively. A blend of an active material and carbon black C45 powder was crushed into a fine powder and slowly added to a liquid thickening agent in piles. A liquid thickening agent was made by stirring CMC and SBR in a 60 °C heated distilled water. The resulting slurry was subsequently pasted on a copper foil and dried at 105 °C for 12 h, in a vacuum oven. The carbon black C45 cathodes were prepared using the same procedure used for the LTO

anodes but with proportions of 95: 2.5: 2.5 wt% for active materials, CMC and SBR, respectively. The cathode slurry was coated on an aluminium foil and left to dry for 12 h at 60 °C, inside a vacuum oven.

3.2.2 Modification of anode materials

Ammonium fluoride NH_3F and cerium nitrate hexahydrate $Ce(NO_3)_3\ 6H_2O$ were each dissolved in distilled water. Thereafter LTO powder transferred into the cerium nitrate hexahydrate solution and stirred. The NH_3F solution was steadily poured to the resulting mixture of LTO and cerium nitrate hexahydrate solution. After a constant stir for 5 h at 80 °C, the resulting solid residue was filtered using a centrifuge and properly rinsed with distilled water. The filtered powder was then calcinated at 400 °C for 5 h in an argon atmosphere. This method of synthesis is illustrated in Figure 3.1. The added contents were such that the ammonium fluoride and cerium nitrate hexahydrate made a stoichiometric molar ratio of Ce^{3+}/F^{-}=1/3 with the amount of CeF_3 corresponding to 2 wt% of the LTO powders [1, 2].

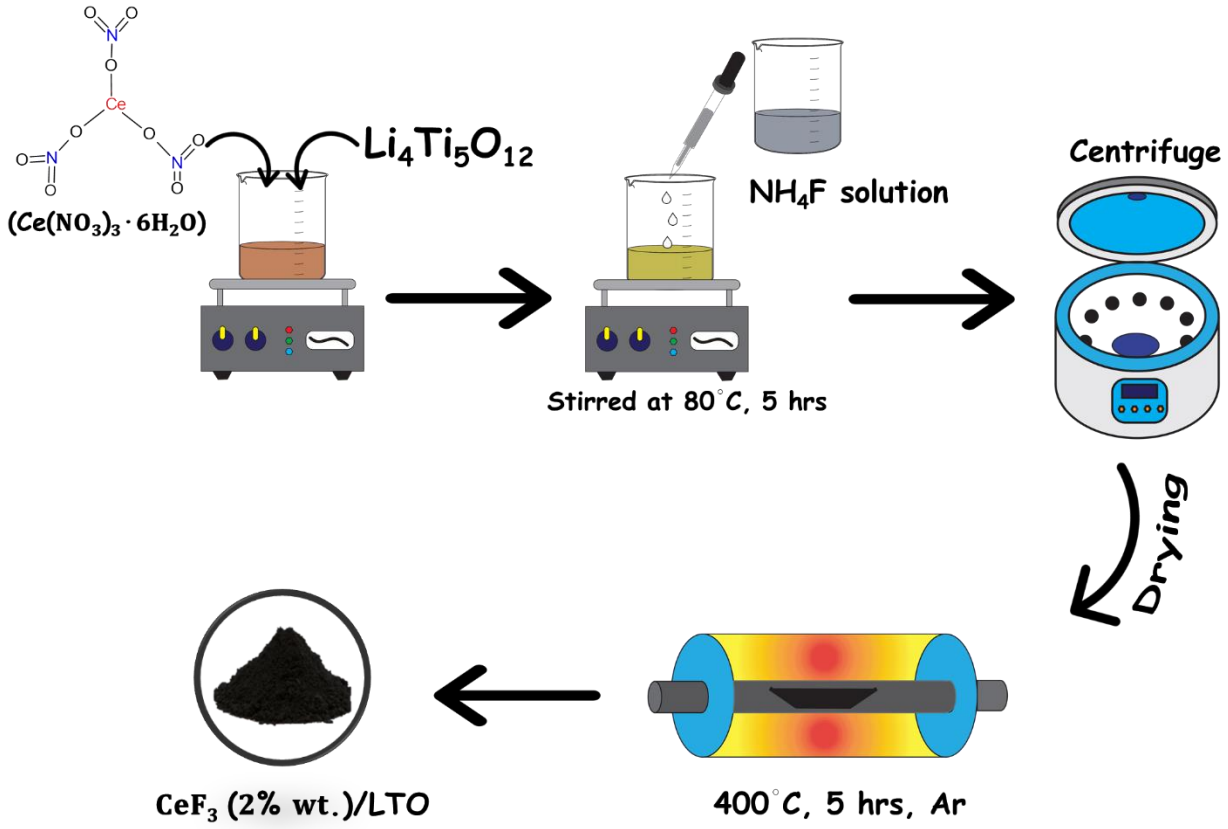


Figure 3.1: Synthesis flow of LTO-CeF_3.

To synthesize microwaved materials, the LTO-p and CeF_3 coated LTO were subjected to microwave radiation at 600 watts for 20 min. Two samples were created from each LTO material (either from a pristine or coated material), with one being exposed to the radiation in a powdered form and the other mixed with distilled water prior to the exposure, as shown in Figure 3.2.

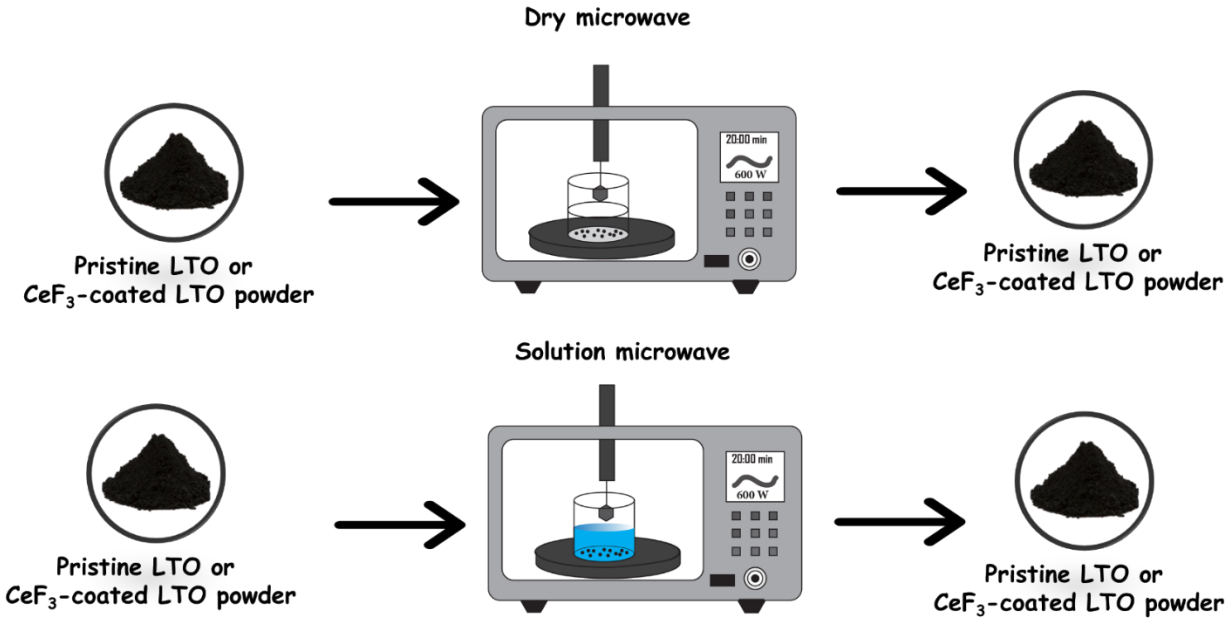


Figure 3.2: Syntheses of microwaved materials.

3.3 Material characterization

3.3.1 X-ray diffractometry (XRD)

The XRD patterns of the materials used in this study were determined using a Bruker D2 Phaser, with Cu-Kα radiation at 30 kV and 10 mA. The samples were prepared by grinding them into a powder using an agate mortar and pestle. Subsequently, they were mounted onto a sample holder and flattened using a glass plate. The XRD patterns were obtained in the range of 10° to 90° 2θ, with a step size of 0.026°.

3.3.2 Raman spectroscopy

A Raman spectrometer (micro-Raman mode; Jobin-Yvon T64000, λ = 532 nm) was employed to create the Raman plots of the materials studied in this dissertation.

3.3.3 Transmission electron microscopy (TEM)

The surface morphology of the materials was characterized using an FEI Spirit 120 kV TEM instrument. For enhanced visualization of the materials, high-resolution transmission electron (HRTEM) analyses were carried out with a JEOL JEM 2100 instrument operating at 200 kV. Sample preparation involved dispersing a small amount of powder on a specula tip in ethanol, followed by ultrasonication for 3 minutes. The resulting suspension was then drop-cast onto a carbon-coated copper grid and allowed to dry at room temperature before measurement. The HRTEM analyses were conducted at the Council for Scientific and Industrial Research (CSIR).

3.3.4 Scanning electron microscopy (SEM)

To study the morphology and elemental composition of the materials, an LEO 1525 SEM instrument operating at an accelerating voltage (EHT) of 10 kV was employed. Sample preparation involved coating the powder samples on a sticky carbon tape affixed to an aluminium specimen stud. The SEM analyses were carried out at the National Metrology Institute of South Africa (NMISA).

3.3.5 Energy dispersive X-ray spectroscopy (EDS)

The elemental composition of the materials in this study was determined using Energy Dispersive X-ray Spectroscopy (EDS). A LEO 1525 SEM instrument, equipped with an OXFORD INCA

EDS detector, was employed for this analysis. The EDS analyses were performed at the National Metrology Institute of South Africa (NMISA).

3.3.6 X-ray photoelectron spectroscopy (XPS)

XPS measurements were carried out at NMISA using a Thermo ESCAlab 250Xi with monochromatic Al K α (1486.7 eV), 300 W (X-ray power), 900 μm(X-ray spot size), 100 eV (Pass energy survey), 20 eV (Pass energy Hi-res) at < 10 -8 mBar. The sample preparation was achieved by scattering the sample powders onto carbon tape.

3.3.7 Brunauer-Emmett-Teller analysis (BET)

Micromeritics Tristar 3000 BET instrument was used to measure pore sizes of the materials studied on this dissertation. The materials were outgassed at 150 °C for 4 h with gas adsorption performed in liquid nitrogen (-195 °C). Before the measurements, the samples were pre-treated at 80 ºC temperature in a N_2 flow in order to eliminate any adsorbed water or other contaminants.

3.3.8 Thermogravimetric analysis (TGA)

A Thermogravimetric Analyzer (Perkin Elmer 6000) was employed to assess the stability and versatility of the materials under investigation. In this analysis, 10 mg samples were heated in an alumina cup within an argon atmosphere, and the temperature was increased gradually, ranging from 32 °C to 900 °C.

3.4 Electrochemical analyses

3.4.1 Cells configuration

Coin type cells assembled inside a glove box of an argon atmosphere were used to conduct the tests on LTO as an anode material for LIB. The cells comprised of the as-prepared working electrode, lithium foil as a counter electrode and grade GD 1UM 47 mm whatman paper as a separator. The electrolyte used was a 1M $LiPF_6$ solution comprising of ethylene carbonate (EC), diethyl carbonate (DEC), ethyl methylcarbonate (EMC) of a 1:1:1 volume ratio. The assembly is contained in Figure 3.3 (a). The coin cells were left in the glovebox overnight before carrying out the electrochemical tests. BioLogic system (BCS8xx series) was utilized to perform the electrochemical measurements: CV, GCD and EIS. BT-Lab program was used for data acquisition and analysis.

The LIC test were conducted using a T-type Swagelok cell illustrated in Figure 3.3 (b). The half-cell for LIC employed the same chemicals, materials, and electrode (of the same composition) used in the LIBs. The full LIC cell was constructed using LTO materials as an anodes and carbon black C45 as a positive electrode, with all other cell components being the ones utilized in the half cells. The full cell was also constructed inside argon-filled glove box and left overnight before the electrochemical tests. Electrochemical techniques were recorded using BioLogic SP-300 operating on an EC-Lab 11.3.

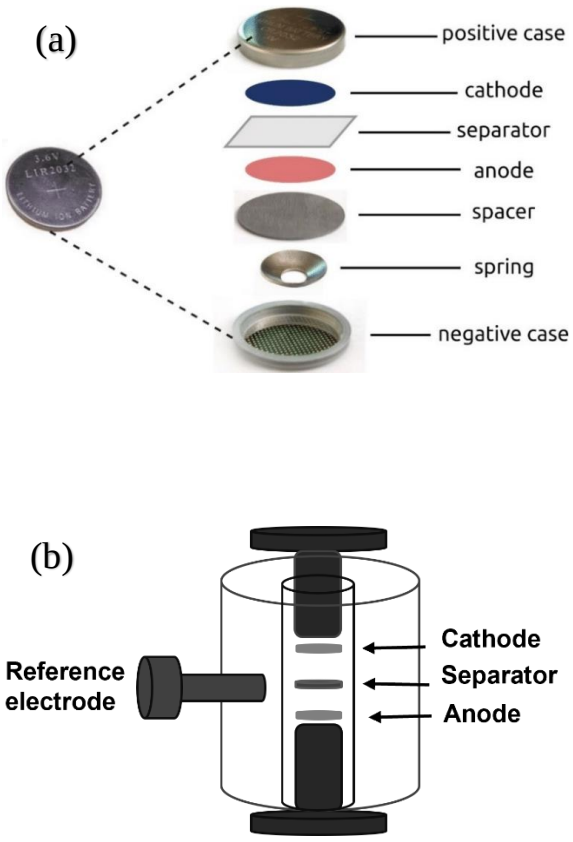


Figure 3.3: (a) Coin cell components **[3]**, (b) Schematic of T-type Swagelok cell.

3.4.2 Cyclic voltammetry

Electrochemical measurements for Li-ion batteries were performed at room temperature within a voltage window of 1.0–2.5 V versus Li/Li^+ at a scan rate of 0.1 mVs^{-1}. The measurements for LTO and LTO-CeF_3 half cells in Li-ion capacitors were conducted within a voltage window of 1.0–2.5 V versus Li/Li^+ at various scan rates, including 0.5, 1.0, 2.5, 5.0, and 10.0 mVs^{-1}. For the LTO-CeF_3//carbon black capacitor measurements, the experiments were carried out at scan rates of 2.0, 5.0, 10.0, and 20.0 mVs^{-1}, within a voltage window of 1.0–3.0 V.

3.4.3 Electrochemical impedance spectroscopy (EIS) Electrochemical half-cells

The electrochemical impedance spectroscopy measurements were carried out on a frequency ranging from 100 kHz to 0.1 Hz.

3.4.4 Galvanostatic tests

The electrochemical measurements for Li-ion batteries were conducted at a rate of 1C for 100 cycles and at a rate of 5C for 1000 cycles. The measurements for LTO and LTO-CeF3 half cells in Li-ion capacitors were carried out at various current densities, including 1.0, 2.0, 3.0, 4.0, and 5.0 Ag^{-1}, within a voltage range of 1.0 to 2.5 V. For the LTO-CeF3//carbon black capacitor measurements, the experiments were performed at different current densities, specifically 1.0, 1.5, 2.5, and 5.0 Ag^{-1}, within a voltage range of 1.0–3.0 V.

3.5 References

[1] Li, W., Li, X., Chen, M., Xie, Z., Zhang, J., Dong, S. & Qu, M. 2014. AlF3 modification to suppress the gas generation of Li4Ti5O12 anode battery. *Electrochimica Acta,* 139**,** 104-110.

[2] Sun, Y.K., Han, J.M., Myung, S.T., Lee, S.W. & Amine, K. 2006. Significant improvement of high voltage cycling behavior AlF3-coated LiCoO2 cathode. *Electrochemistry communications,* 8**,** 821-826.

[3] Zhuo, Y. 2021. *Investigation of nanostructured lithium-ion battery materials.* Friedrich-Alexander-Universitaet Erlangen-Nuernberg (Germany).

Chapter 4

Defect-engineered lithium titanate oxide (LTO) anode materials for lithium-ion batteries

4.1 Introduction

The continuous growth of energy demand and supply always highlights a grave need for efficient energy storage systems (ESSs) and power sources. Lithium-ion batteries (LIBs) have secured a huge traction as power sources of many electronic applications. And this is due to their high working potential, high energy density, long life and high safety [1].

Carbonaceous materials are usually employed as anode materials in a full cell configuration of LIBs utilized in commercial applications, but the safety hazards such as fire and explosions posed by these materials hinder further usage of LIBs in future applications [2]. Carbon materials are likely to develop dendrite growth caused by low intercalation potential (0.1 V vs. Li/Li^+) when cycled in long charge-discharge cycles, resulting in capacity fading and unwanted side reactions [3, 4]. This raises safety concerns in utilising LIBs in future applications including electric vehicles (EVs), and large-scale storage systems of renewable energy that require high power output.

Lithium titanium oxide ($Li_4Ti_5O_{12}$), is considered a good replacement for carbon materials in large-scale LIB anodes, this is based on its merit of high working voltage (~ 1.55 V vs. Li/Li^+), which can suppress the generation of the solid-electrolyte interface layer and avoid dendrite formation for improved safety [5, 6]. Furthermore, LTO experiences a minor volume change during the course of the lithium insertion and extraction, which leads the material to exhibit long cyclability

[7-9]. However, LTO is not widely used in practical applications due to sluggish kinetics caused by low electrical conductivity of $<10^{-13}$ S cm^{-1} and diffusion coefficient of 10^{-16} cm^2s^1, resulting in poor rate capability [10-12]. The slow kinetics of LTO leads to low theoretical capacity of 175 mAh g^{-1} [13]. Excellent safety in LTO anode based LIBs is hampered by evolutions of gaseous species such as H_2, CO, CO_2, CH_4 at elevated temperatures, which causes battery swelling and side reactions [14, 15].

There have been extensive research and development (R&D) efforts and strategies to mitigate these problems, which include morphology and size control of electroactive materials to nanometer scale for improved lithium pathways [16-18], improving electrochemical performance by doping with ions such as Cr^{3+}, Al^{3+}, Ca^{2+}, Mg [19-22] and introduction of conductive/stable surface coating [23-25]. This work seeks to explore the modification of a commercial LTO using surface coat of CeF_3 with the aim of enhancing its electrochemical performance by leveraging on the high ionic conductivity and chemically inertness of CeF_3 at high-temperatures [26-28].

4.2 Results and discussion

4.2.1 Material characterization

4.2.1.1 Powder X-ray diffraction (PXRD)

Crystallographic structures of the materials were evaluated using X-ray powder diffraction, as displayed in Figure 4.1 (a). The diffraction peaks of the materials are ascribed to index (111), (311), (400), (331), (333), (440), (531) and (533) of standard spinel $Li_4Ti_5O_{12}$ (JCPDS Card No. 49–0207) with the Fd3m space group [29-31]. There were no additional reflection peaks observed, suggesting the absence of impurities and diffraction peaks associated with CeF_3 on the coated samples, which may be because of the relatively low CeF_3 content (2wt. %) [32].

Figure 4.1 (b) shows magnified (111) plane peaks. There is an indication of slight peak shifts to higher angles in LTO-md, LTO-mw and LTO-CeF_3 compared to LTO-p (111) peak, which means a decrease in lattice parameters might have occurred [33]. The LTO-CeF_3-md and LTO-CeF_3-mw (111) peaks have shifted to lower angles which may suggest microscopic lattice expansion [34]. For the coated materials, the deviation may have occurred as a result of some portion of CeF_3 being co-doped into the LTO structure, where larger sized Ce^{3+} (0.114 nm) might have entered the smaller sized Ti^{4+} (0.061 nm) sites [35], and F^- (0.136 nm) have been inserted to the 0^{2-} (0.140) sites [36]. The LTO-CeF_3 deviation to higher angle region may be because of higher octahedral site preference energies of Ce–O , which subjected its bond length to diminution when compared to Ti–O [37]. The coated materials may lead to the production of a composite $Li_{4+x-y}Ti_{5x}Ce_xO_{12-y}F_y$ and an anatase TiO_2, as shown in equation 4.1, during 400 °C calcination of the coated materials [38].

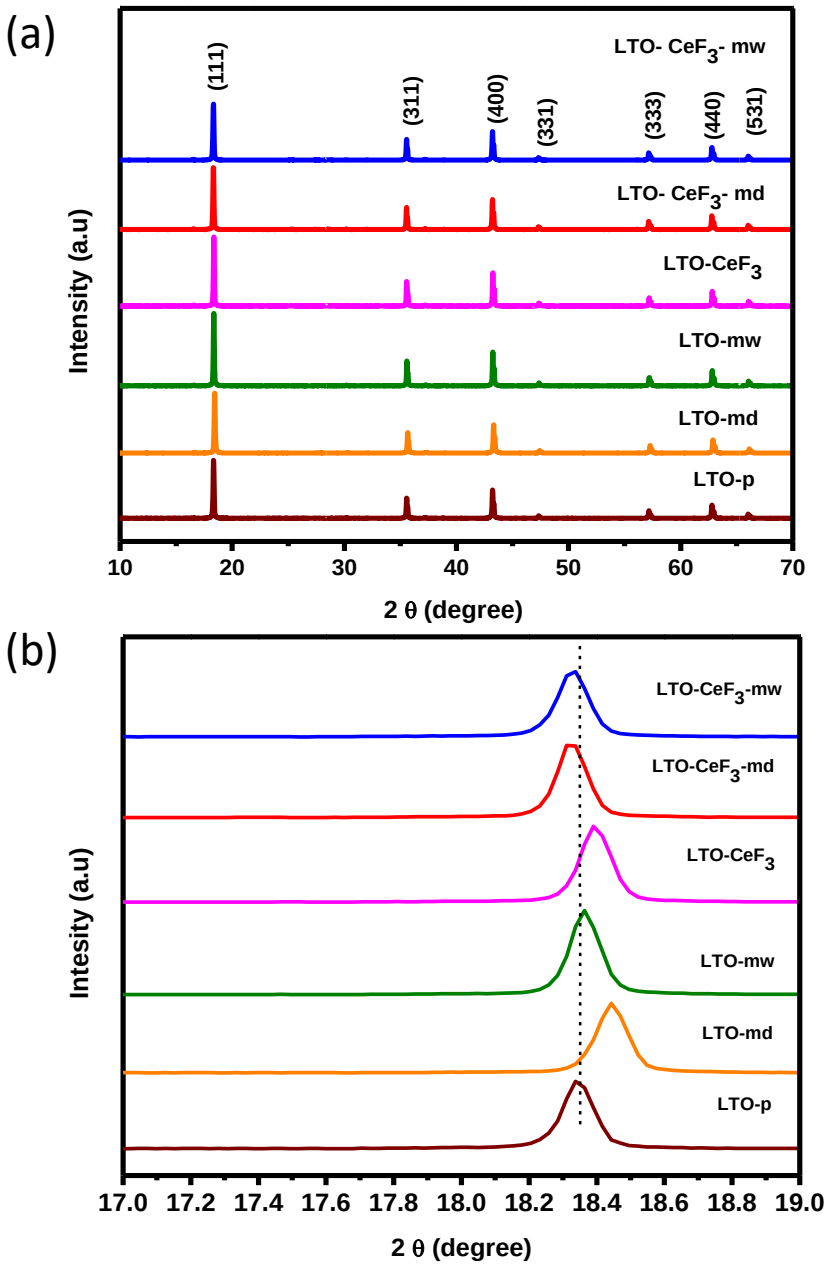


Figure 4.1: (a) XRD patterns, (b) 111 peaks of LTO-p, LTO-md, LTO-mw, LTO-CeF_3, LTO-CeF_3-md, and LTO-CeF_3-mw

$$Li_4Ti_5O_{12} + CeF_3 \rightarrow TiO_2 + Li_{4+x-y}Ti_{5x}Ce_xO_{12-y}F_y \quad (4.1)$$

Table 4.1: Comparison of peak intensity ratios.

Material	1_{111}	I_{311}	$1_{111}/I_{311}$	I_{311}/I_{400}
LTO-p	307.39	110.83	2.77	0.735
LTO-md	259.67	90.16	2.88	0.726
LTO-mw	314.76	109.90	2.86	0.752
LTO-Ce$\mathbf{F_3}$	279.49	94.60	2.95	0.701
LTO-Ce$\mathbf{F_3}$-md	279.18	98.44	2.74	0.746
LTO-Ce$\mathbf{F_3}$-mw	243.54	91.12	2.67	0.733
JCPDS #49–0207	3507.00	1585.00	2.21	0.728

The $1_{111}/I_{311}$ peak intensity ratios of the materials (computed using the XRD patterns) are listed in Table 4.1 and compared with standard JCPDS data. The $1_{111}/I_{311}$ measures the degree of confusion between lithium ions and transition metals in spinel structures, offering insights into the lithium-ion pathway of spinel structures and expected electrochemical performance [39]. Comparing the intensity ratios of the materials with the standard JCPDS No. 49–0207 data, LTO-CeF_3-mw has a lower deviation which means the materials possess a smoother Li-ion path than all other materials; hence a higher rate capability can be expected. The higher confusion of LTO-CeF_3 means the Li-ion path has been altered in materials and might lead to poor or lower electrochemical performance at high rates. These results proved that a combination of CeF_3 coating, microwave irradiation and water modification on LTO yields a lower degree of confusion and might promote a higher rate capability.

4.2.1.2 Raman spectroscopy

Figure 4.2 displays Raman spectra of the materials. All the materials contain Raman vibrations modes at 236, 343, 429, 674, 755 cm^{-1} which conform to the A_{1g} + E_g +3F_{2g} feature of the spinel structure [40]. The major vibration at 674 cm^{-1} (A_{1g} mode) is originated from the symmetric Ti–O stretch of TiO_6 octahedra. The band at 429 cm^{-1} (E_g mode) is linked to the asymmetric Li–O stretch of LiO_4 tetrahedral and the 236 cm^{-1} peak (F_{2g} mode) originates from δ(Ti–O) [41]. The vibrational mode at 236 cm^{-1} and other weak bands are ascribed to the F_{2g} mode. On all the coated materials, there is an observation of extra vibration peak at 143 cm^{-1} , which is a peak of an anatase TiO_2 [42]. The anatase formation outlined by equation 4.1 substantiate the anatase found by the Raman spectroscopy.

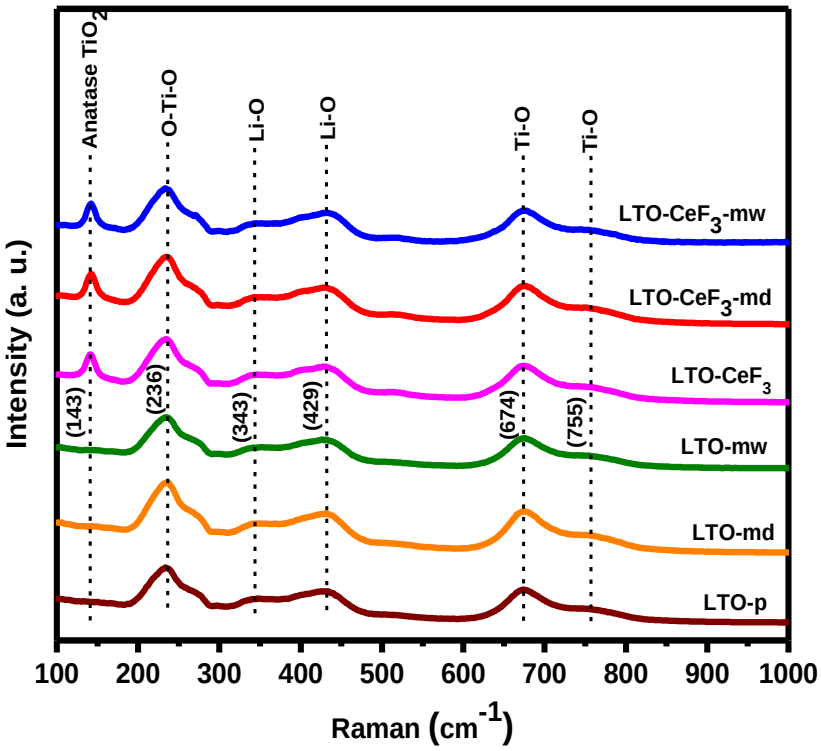


Figure 4.2: Raman spectra of the materials.

4.2.1.3 Transmission electron microscopy (TEM)

In order to substantiate the effects of CeF3 coating and microwave irradiation on LTO-p, transmission electron microscopy (TEM) was employed to analyze the microstructure of the LTO-p, LTO-mw, LTO-CeF_3 and LTO-CeF_3-mw. The TEM micrographs of the microstructures are presented in Figure 4.3. The TEM image of LTO-p in Figure 4.3 (a) indicate that the LTO-p exhibit a cubic morphology of a uniform particle size distribution [43]. The same observation is seen on Figure 4.3 (b) for LTO-mw. It can be observed that the coated materials (LTO-CeF_3 and LTO-CeF_3-mw) in Figure 4.3 (c-d) have CeF_3 distributed on the surface. LTO-CeF_3 in Figure 4.3 (c) has CeF_3 dispersed on the surface and LTO-CeF_3-mw in Figure 4.3 (d) possess a uniformly distributed CeF_3 on the surface [44].

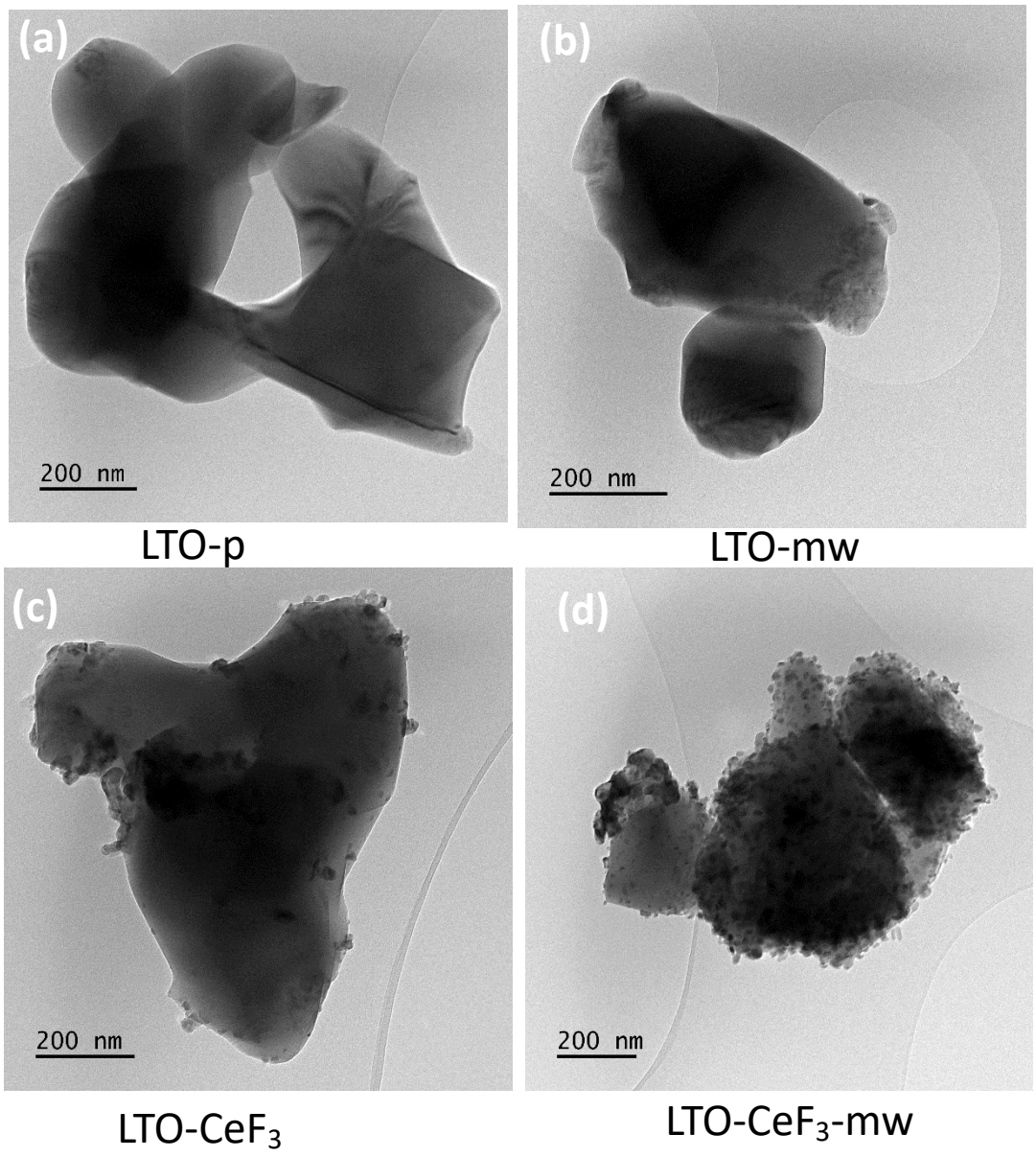


Figure 4.3**:** TEM micrographs of (a) LTO-p, (b) LTO-mw, (c) LTO-CeF_3 and (d) LTO-CeF_3-mw.

4.2.1.4 High-Resolution Transmission electron microscopy (HRTEM)

High-Resolution Transmission Electron Microscopy (HRTEM) was conducted to further analyze the morphologies of LTO-p, LTO-mw, LTO-CeF_3 and LTO-CeF_3-mw. Figure 4.4 shows the HRTEM micrograph of LTO-p. The Image-J software is used to calculate the *d*-spacing between the two bright fringes in the HRTEM image. The LTO-p image reveals lattice fringes with the spacing of 0.486 nm and 0.493 nm region (I) on Figure 4.4 (b) and (II) on Figure 4.4 (c). The observed spacing in these regions is ascribed to the (111) lattice plane from spinel $Li_4Ti_5O_{12}$ phase [31, 45], thereby confirming the existence of $Li_4Ti_5O_{12}$ in this sample. The selected area electron diffraction (SAED) patterns are shown for the regions (I) and (II), with all these regions being mono-crystalline as evident through their discrete bright spots [46].

The lattice fringe of (222), (311) and (220) lattice planes are observed to have spacing of 0.240, 0.238, 0267 and 0.280 nm on regions (I – IV) as shown on Figure 4.5 (a-d) for LTO-mw. The lattice planes correspond to the ones of LTO phase with the differences indicated by decrease in the lattice spacing from 0.241, 0.252 and 0.296 nm found in the LTO phase (JCPDF No. 49-0207) [31] for (222), (311) and (220) lattice planes, respectively. This observation agrees with the XRD analysis. The SAED images of all the regions indicate single crystalline nature of cubic spinel [47].

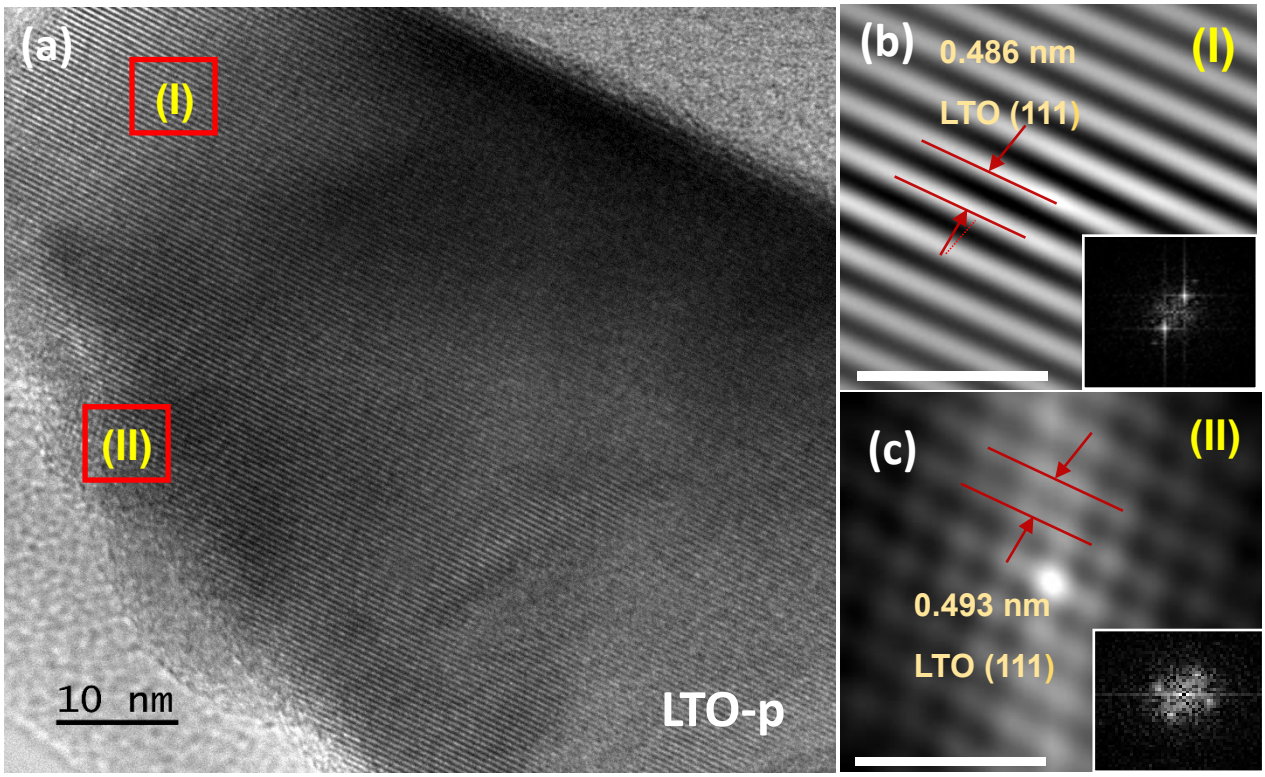


Figure 4.4: HRTEM image of (a) LTO-p, region and SAED image of (b) LTO (111) and (c) LTO (111) lattice plane on LTO-p.

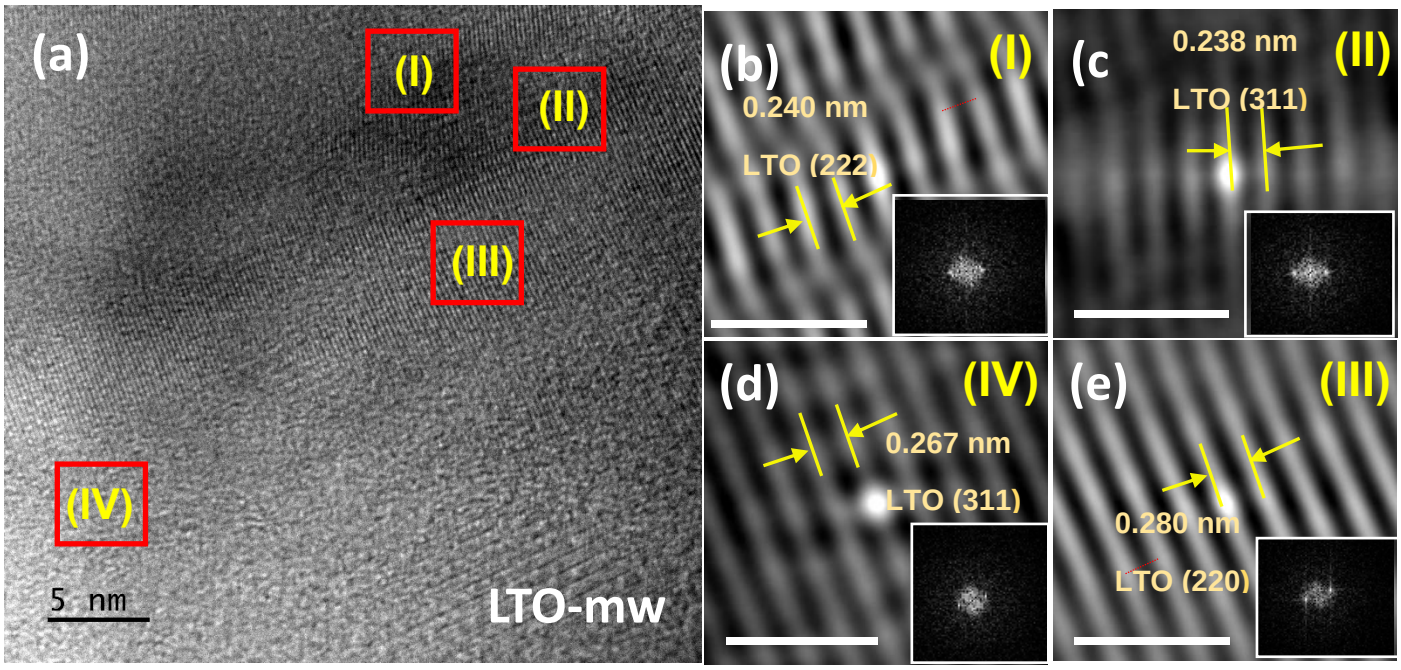


Figure 4.5: HRTEM image of (a) LTO-mw, region and SAED image of (b) LTO (222), (c) LTO (311), (d) LTO (311), and LTO (220) lattice plane on LTO-mw.

From Figure 4.6 containing HRTEM image of LTO-CeF_3, the co-existence of LTO, anatase TiO_2 and CeF_3 [48] is demonstrated by lattice fringes spacing of 0.416 nm LTO-p (111) lattice plane on region (IV), 0.312 and 0.321 nm on regions (II) and (III), respectively, for CeF_3 (111) lattice plane [49], and (101) anatase TiO_2 plane with 0.334 nm [50]. There is a decrease in lattice spacing in the (111) lattice plane of LTO-CeF3 when compared with the LTO-p (JPDS No. 49-0207 (111) lattice plane (0.482 nm), which substantiate the conclusions made in the XRD results. The observed SAED images indicates that anatase TiO_2 and CeF_3 have mono-crystalline nature.

Figure 4.7 shows the HRTEM image taken for LTO-CeF_3-mw. The LTO (311)/(220), Anatase TiO_2 (101) and CeF_3 (111) lattice fringes are observed with lattice spacing of 0.267 [51]/0.299 nm [52], 0.349 nm [53] and 0.317 nm [54], respectively. These observations indicate a co-existence of LTO, Anatase TiO_2 and CeF_3 on LTO-CeF_3-mw. There is increase in lattice spacing on LTO-CeF3-mw as opposed to 0.25 nm for (331) and 295 nm for (220) lattice plane found on LTO-p phase (JCPDF No. 49-0207), with this observation validating the XRD analysis. The image of LTO-CeF_3-mw indicates a dual-phase LTO-TiO_2 composite which will increase the specific capacity of LTO and the high grain boundary (GB) observed will enhance the kinetic of lithium insertion/extraction [55]. The SAED images of the regions on this sample are a single crystalline.

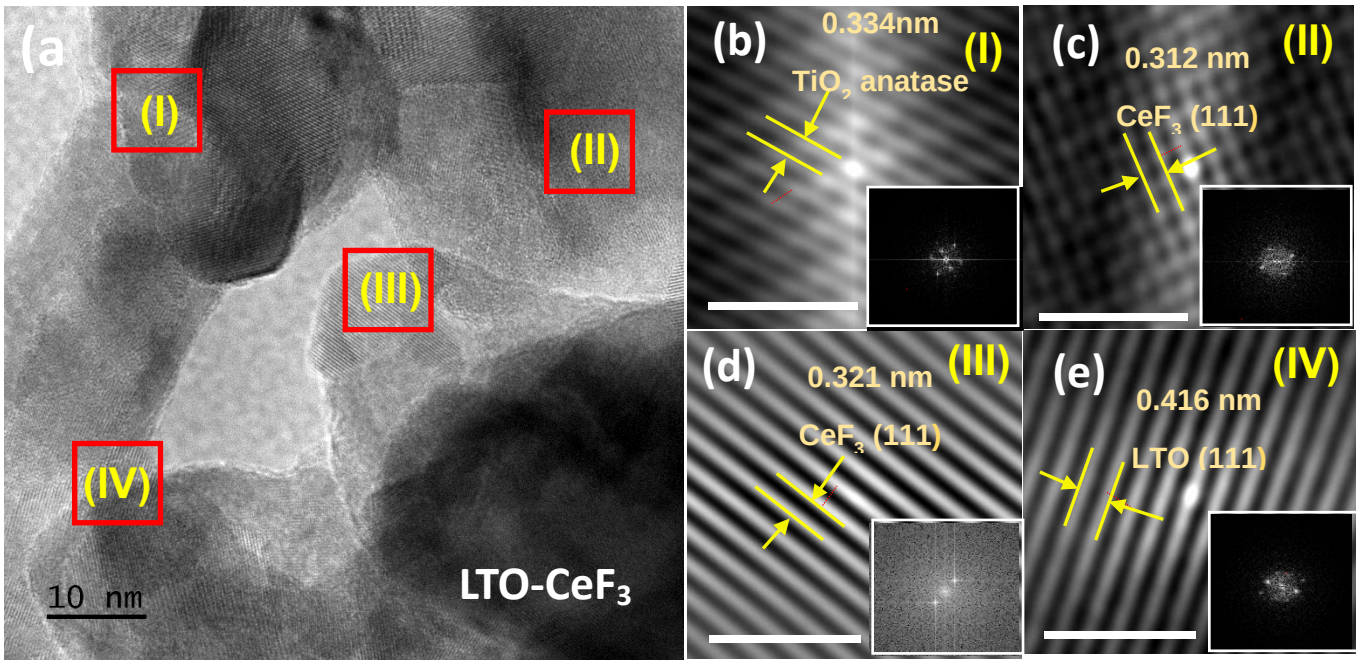


Figure 4.6**:** HRTEM image of (a) LTO-CeF_3, region and SAED image of (b) TiO_2 anatase (101), (c) CeF_3 (111), (d) CeF_3 (111), and (e) LTO (111) lattice plane on LTO- CeF_3.

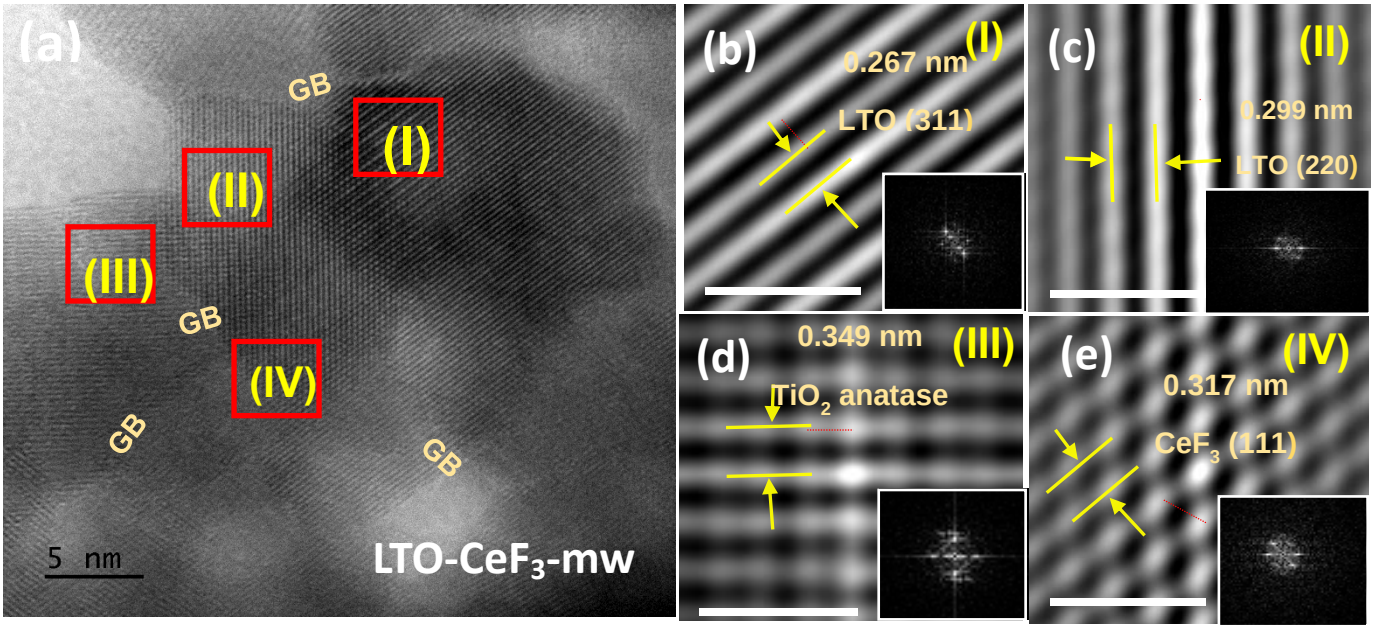


Figure 4.7**:** HRTEM image of (a) LTO-CeF3-mw, region and SAED image of (b) LTO (311), (c) LTO (220) (d) TiO_2 anatase (101), and (e) CeF_3 (111) lattice plane on LTO- CeF_3-mw.

4.2.1.5 Energy dispersive X-ray spectroscopy (EDS)

Energy dispersive X-ray spectroscopy (EDS) was conducted for studying the distribution of the elements on LTO-p, LTO-mw, LTO-CeF_3 and LTO-CeF_3-mw. On all the samples Li was not detected on the EDS spectra as a result of this element having atomic number less than that of beryllium [56]. Ti is homogeneous distributed on all the materials shown in Figure 4.8 (b) – 4.11(b), indicating its presence on all the materials. Elemental mappings of O shown in Figure 4.8 (c) – 4.11(c) demonstrate even distributions on all the materials, with O having 96.86 wt.% on LTO-p but it registered 0.00 wt.% on all the modified materials. This may be because of the oxygen X-rays emitted having low energy that the specimen or the detector can easily absorb [57].

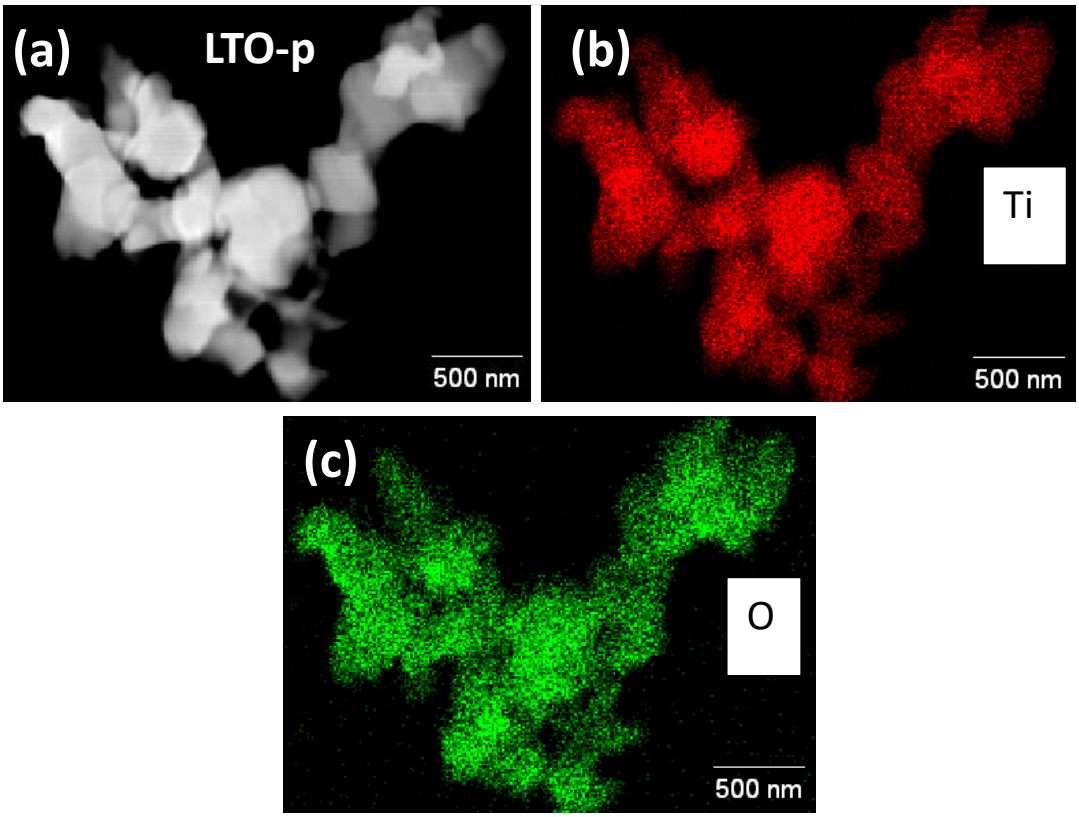


Figure 4.8: SEM micrographs of (a) LTO-p, with its associated (b) Ti and (c) O elemental mapping.

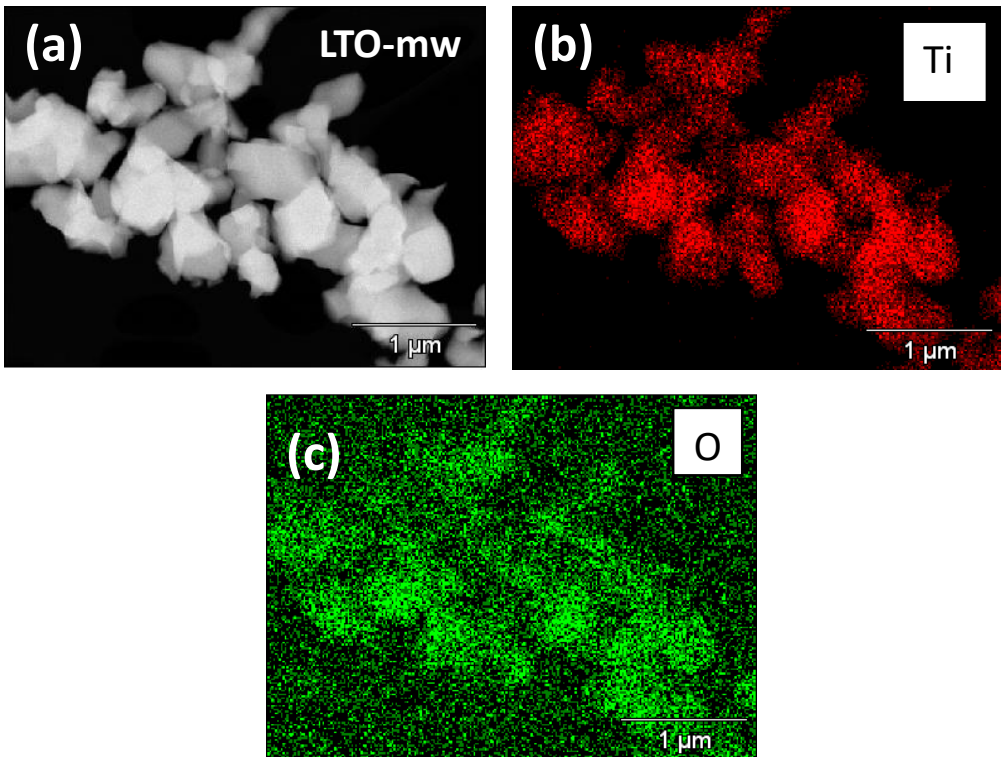


Figure 4.9**:** SEM micrographs of (a) LTO-mw, with its associated (b) Ti and (c) O elemental mapping.

Figure 4.10 (d-e) and Figure 4.11 (d-e) indicate that Ce and F are found on both LTO-CeF3 and LTO-CeF3-mw respectively. Their presence confirms their existence on these materials. The LTO-CeF_3 material has 1.25 wt.% of Ce and 0.74 wt.% of F, while LTO-CeF_3-mw contains 2.81 wt.% and 0.30 wt.% of Ce and F, respectively. The Ce is homogenously distributed on these materials while F possess a dispersed and even distribution. The species are distributed on the sample's surface as revealed on the TEM micrographs.

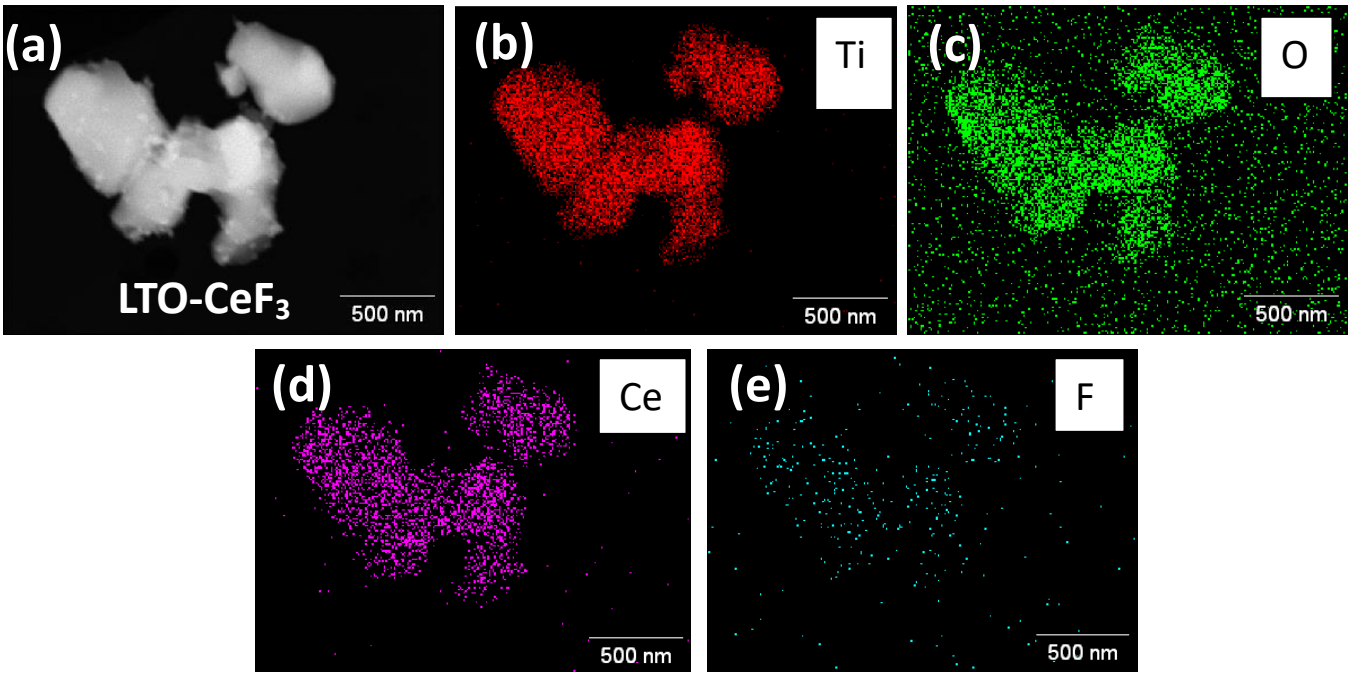


Figure 4.10**:** SEM micrograph of (a) LTO-CeF_3, with its associated (b) Ti, (c) O, (d) Ce, and (e) F elemental mapping.

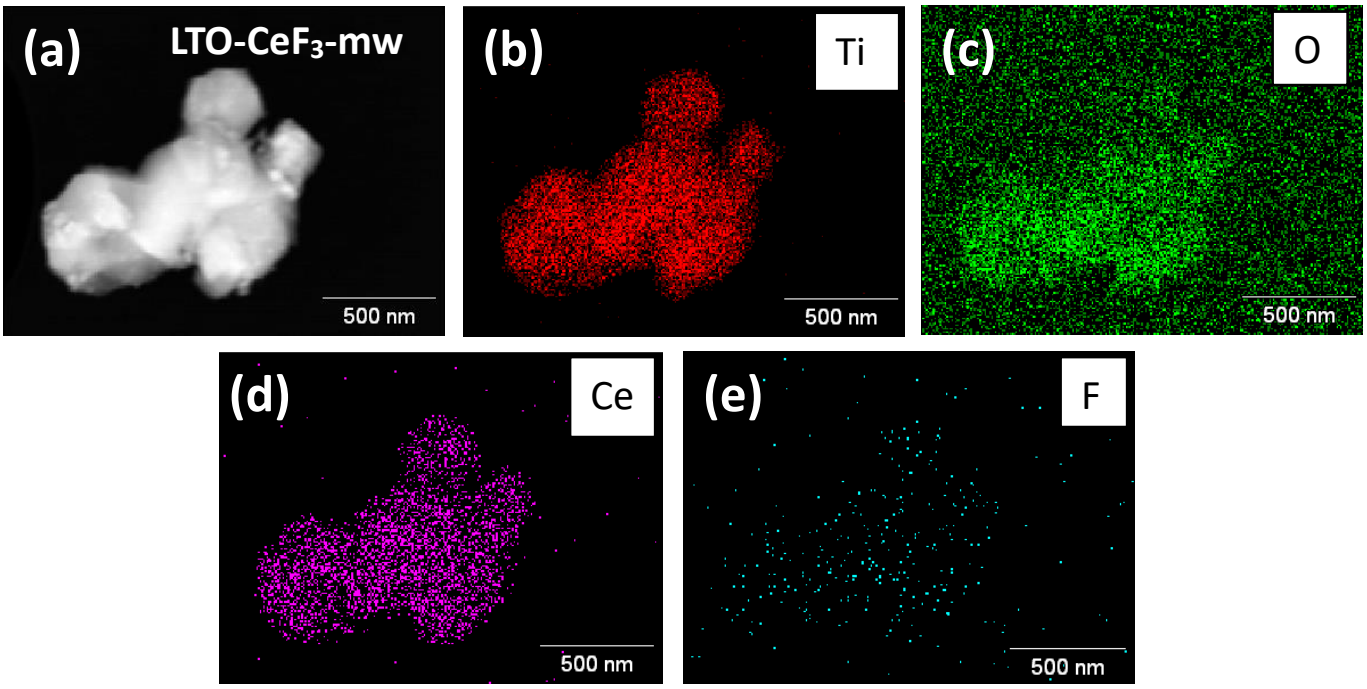


Figure 4.11: SEM micrographs of (a) LTO-CeF_3-mw , with its associated (b) Ti, (c) O, (d) Ce, and (e) F elemental mapping.

4.2.1.6 X-Ray photoelectron spectroscopy (XPS)

X-ray photoelectron spectroscopy (XPS) were carried out for elemental analyses and surface compositions of the materials. All the XPS spectra contained the characteristics peaks: Li1s, Ti2p, Ti2s, O1s and C1s corresponding to the existence of Li, Ti, O and C respectively, as shown in Figure 4.12. Clear Ce3d peaks indicating the presence of Ce on all the coated materials were found in 870-930 eV range. By magnifying the XPS spectra at the range of 660-700 eV as shown in Figure 4.13 (d), F1s peaks were observed at 685 eV on all the coated materials, thereby confirming the presence of F^- on the coated materials. The deconvolution of Ce3d on the coated materials shows Ce exists in Ce(III) and Ce(IV) oxidation states as revealed in Figure 4.13 (a-c).

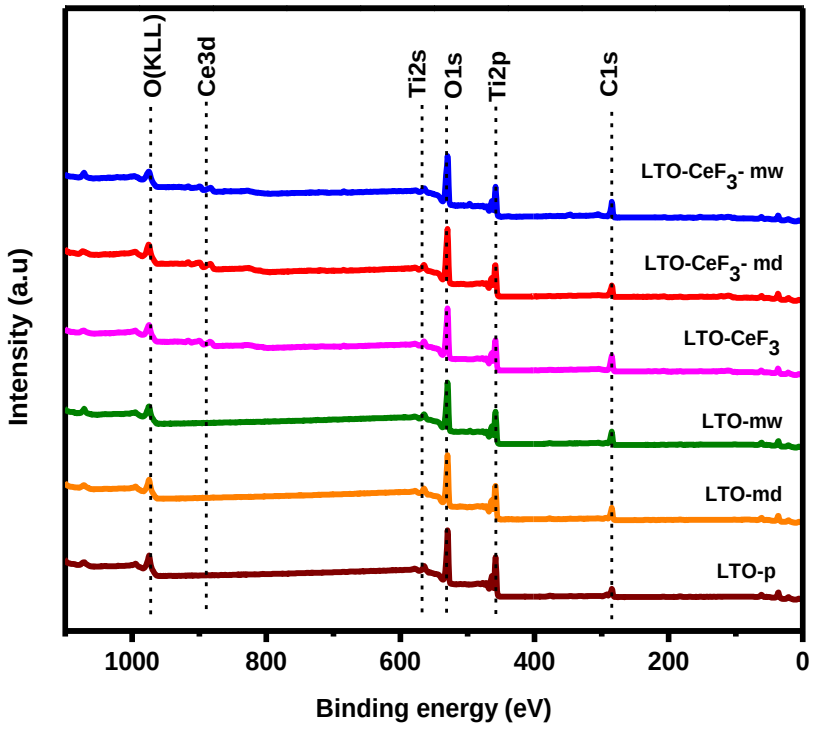


Figure 4.12: XPS spectra of the materials.

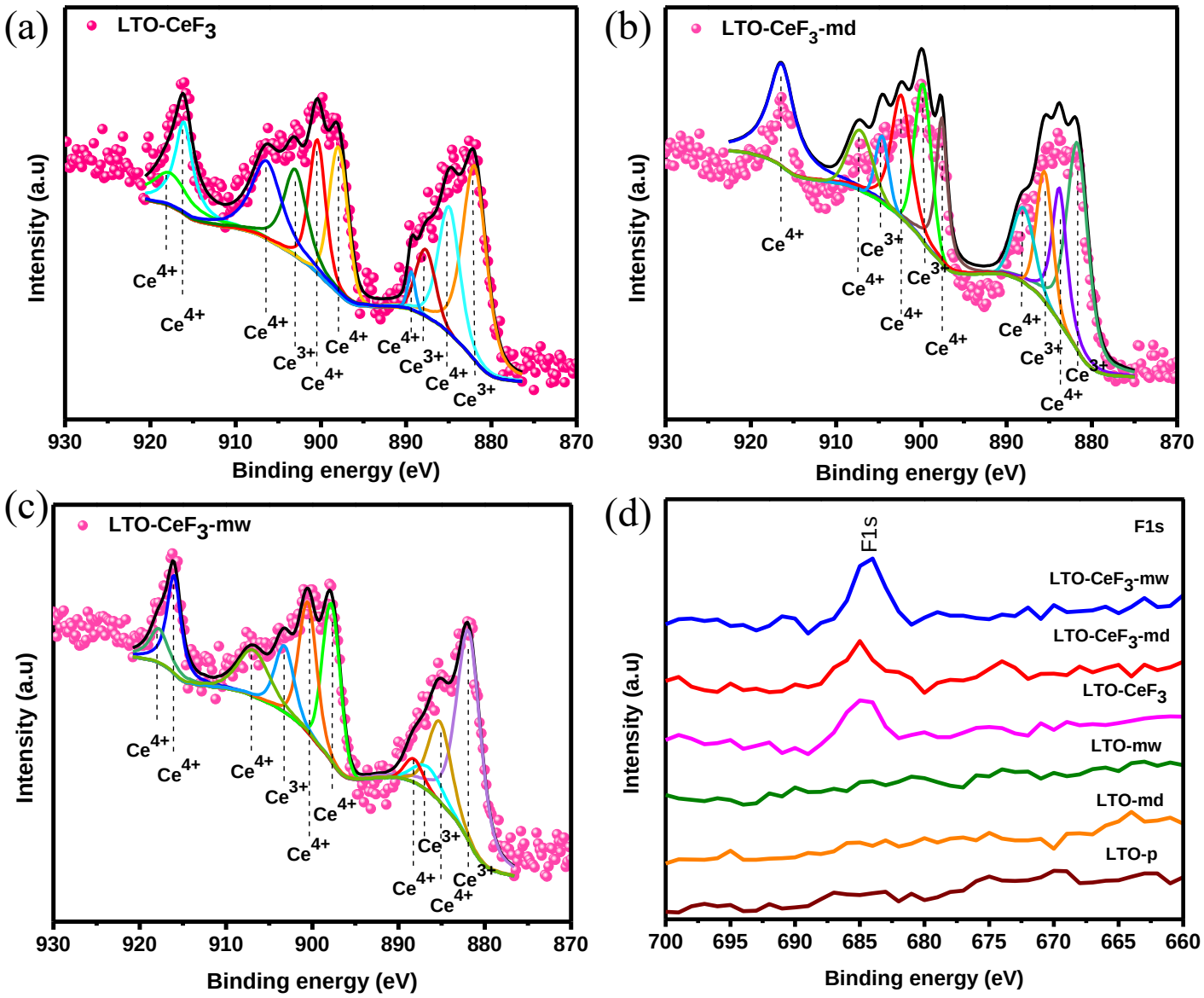


Figure 4.13: Deconvolution of Ce3d in (a) LTO-CeF_3, (b) LTO-CeF_3-md, (c) LTO-CeF_3-mw and (d) XPS spectra of the materials at 660-700 eV.

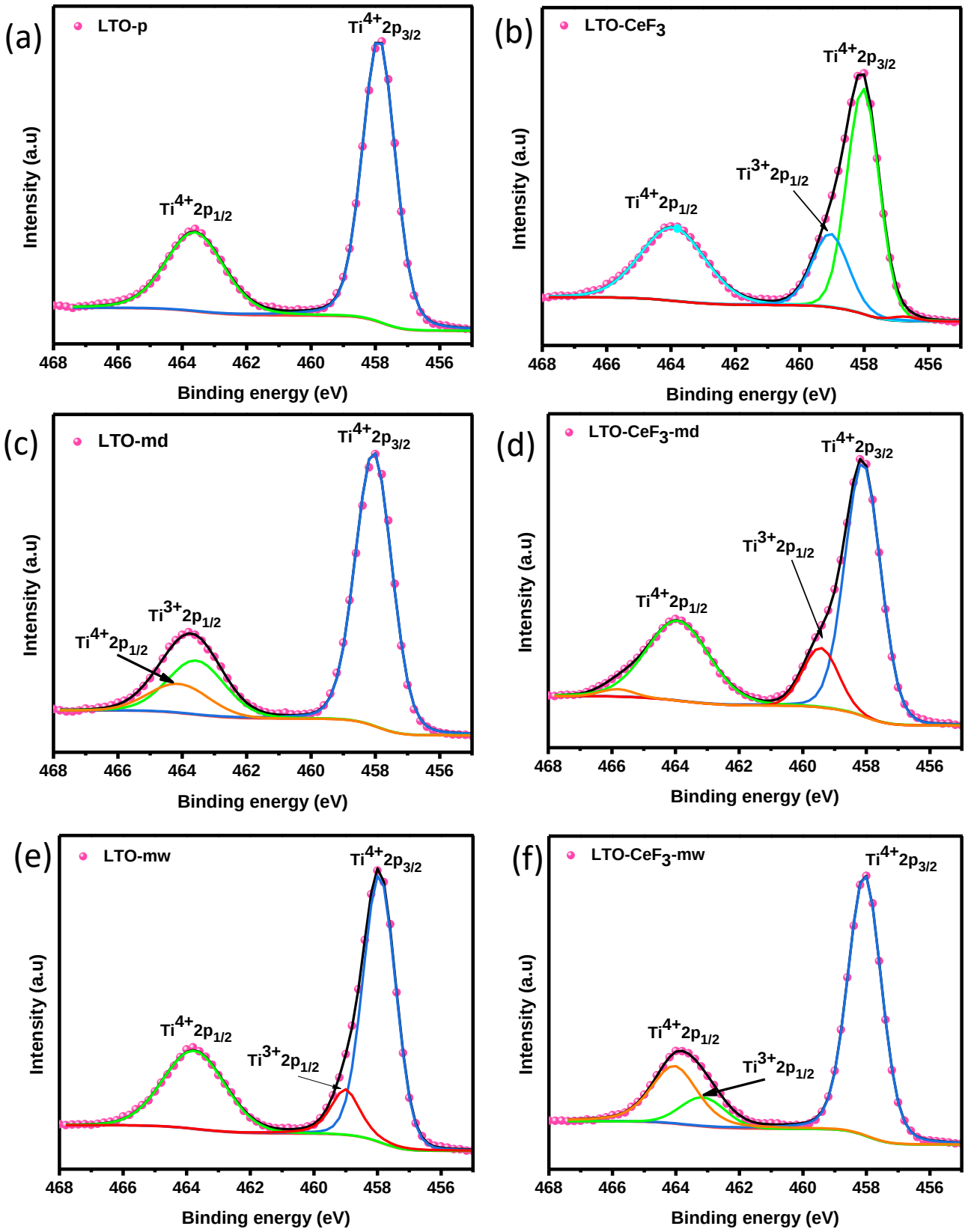


Figure 4.14**:** Deconvolution of Ti2p on (a) LTO-p, (b) LTO-CeF_3, (c) LTO-md, (d) LTO-CeF_3-md, (e) LTO-mw, and (d) LTO-CeF_3-mw material.

The electrochemical reaction and charge-discharge profile of spinel LTO involve a redox reaction of Ti^{4+}/Ti^{3+} couple [58], hence exploring titanium oxidation states in the materials will offer insights into redox behaviour and possible electrochemical performance of the materials. The high-resolution spectra of Ti2p of all the materials are compared in Figure 4.14 (a-f). In analyzing the oxidation state of Ti ions in the materials, $Ti2p_{1/2}$ and $Ti2p_{3/2}$ doublet representing the oxidation state of Ti^{4+} at the octahedral environment were detected at 463.8 and 458.0 eV on LTO-p [59]. In all other materials, $Ti2p_{1/2}$ and $Ti2p_{3/2}$ characteristic peaks were observed but with migration to higher binding energy, which means surface coating and microwave irradiation had changed the surface bonding of LTO. For coated materials, this may be as a result of interaction between the LTO surface and CeF_3 coating layer. Zhu *et al*. [60] reported the migration of these peaks to higher binding energies in LTO-TiO_2 composite compared to a pristine LTO, which indicates that anatase TiO_2 peaks observed on the Raman spectra of coated materials might be ascribed to this shift.

Further exploration of the Ti2p indicates mixed states Ti^{4+} and Ti^{3+} on all the modified LTO materials (both coated and uncoated) [61]. Partial reduction of Ti^{4+} to Ti^{3+} may have occurred as a result of oxygen-deficient defects, this is inferred from the report on reduction of Ti-ions due to charge compensation mechanism created by the presence of oxygen vacancies ($V_o^{\cdot\cdot}$) [62]. Oxygen vacancies can be created when heat-treatment of LTO is carried out in a reducing or a chemically inactive gas atmosphere [63]. This indicates that microwave irradiation and annealing may have created oxygen vacancies. The coated materials may have experienced this reduction from the charge compensation when Ce^{3+} ions entered the LTO structure to produce the composite material postulated in the XRD analysis. This process is seen in equation 4.2-4.3 [34]. Ti^{4+} is considered to be insulating compared to Ti^{3+}, which means that the modified materials were expected to exhibit higher rate capability than LTO-p since the electronic conductivity will be increased [34].

$$Ce^{3+} \rightarrow Ce_{Ti} + V_o'' + e^- + \frac{1}{2}O_2 \quad (4.2)$$

$$Ti^{4+} + e^- \rightarrow Ti^{3+} \quad (4.3)$$

4.2.1.7 Brunauer -Emmett-Teller analysis (BET)

Table 4.2: Nitrogen gas adsorption analysis of the materials.

Material	Surface area ($\mathbf{m^2/g}$)	Pore Volume ($\mathbf{cm^3/g}$)	Pore Size (nm)
LTO-p	1.782	0.032	70.992
LTO-md	3.051	0.042	55.352
LTO-mw	1.51	-	-
LTO-CeF_3	3.529	0.047	53.282
LTO-CeF_3-md	4.205	0.090	83.979
LTO-CeF_3-mw	3.888	0.036	37.768

The surface area, pore volume, and pore diameters of the materials are shown in the BET data in Table 4.2. The LTO-p has a surface area that is less than LTO-md but greater than LTO-mw. This allowed the microwaved LTO-md to have more contact with the electrolyte than the pristine LTO, which aided Li^+ flow and boost discharge capacity, but it also made it more vulnerable to side reactions, which could cause capacity fading. The LTO-p material had a larger pore size than LTO-md and LTO-mw, which means LTO-p favoured Li^+ insertion into its structure for better charge/discharge processes [64].

The same surface area effect caused by the microwave occurs on the coated materials, with LTO-mw having a greater surface area than LTO- CeF_3 and LTO-CeF_3-mw having the smaller surface area. All the coated materials with the same microwave status (md and mw) as the pristine materials possessed a higher surface area. LTO- CeF_3-md had the highest surface area and pore size out of all the materials. It possessed the capability of smooth Li^+ transport and its high surface area allowed likelihood of undesirable side reactions. The modified materials besides LTO-mw, had higher surface area than LTO-p, which bring expectation of increased capacity and conductivity when they are subjected to electrochemical tests [65]. LTO-CeF_3-md had the highest pore size of 83.979 nm followed by LTO-p, LTO-md, LTO-CeF_3 and LTO-CeF_3-mw with 70.992, 55.352, 53.282 and 37.768 nm, respectively. LTO-mw pore size could not be measured because of its very low surface area.

4.2.1.8 Thermogravimetric analysis (TGA)

Figure 4.15 shows TGA curves with three stages of weight loss in all materials in an argon atmosphere. All the materials were stable, still retaining more than 97% of their initial weights when heated to 900 °C. The samples had less weight loss in stage 1 (~ 32 °C to 200 °C), which may be as a result of water desorption [66, 67], a considerable weight loss in the second stage (~ 200 °C to 695 °C) which may have been caused by decomposition of carboxylic groups onto LTO surface [66, 68] and in stage 3, the materials were stabilized (~ 695 °C to 900 °C). The materials subjected to microwave radiation had slightly more loss which may have resulted from the structural changes that might have originated from the oxygen vacancies postulated on the Ti2p XPS analyses of microwave materials [68]. The overall weight losses were 1.41, 1.80, 2.12, 1.39, 1.46 and 1.96% for LTO-p, LTO-md, LTO-md, LTO- CeF_3, LTO- CeF_3-md and LTO- CeF_3-mw, respectively. The coated materials were slightly thermally stable.

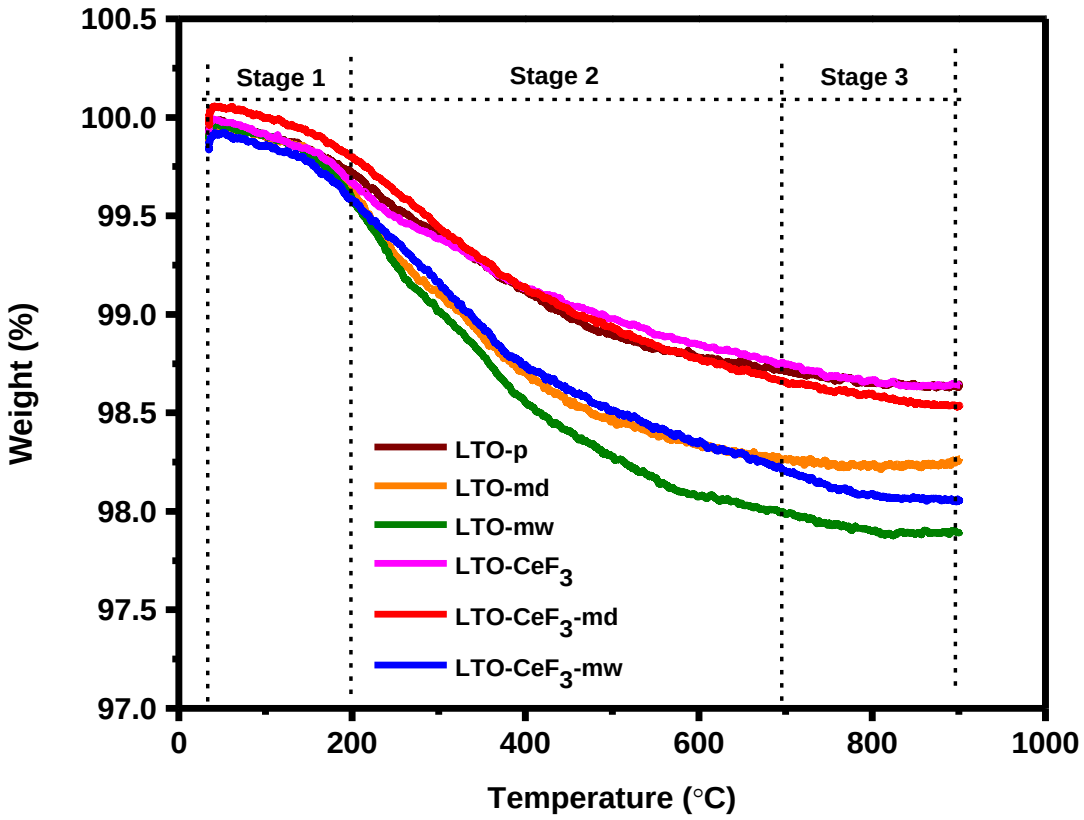


Figure 4.15**:** TGA curves of the samples.

4.2.1.9 Scanning electron microscopy (SEM)

The morphologies of the materials were evaluated using SEM images contained on Figure 4.16. The images showed LTO-p with block-shaped particles of homogeneous particle size distribution while LTO-CeF_3 particles had the same sharpness but with the particle agglomerated. The agglomeration disappeared in LTO-CeF_3-md. LTO-CeF_3-md and LTO-md possessed the same morphology as LTO-p but with clearer picture fields. LTO-mw and LTO-CeF_3-mw had blurred picture fields but with the same morphologies as LTO-md and LTO-CeF3-md.

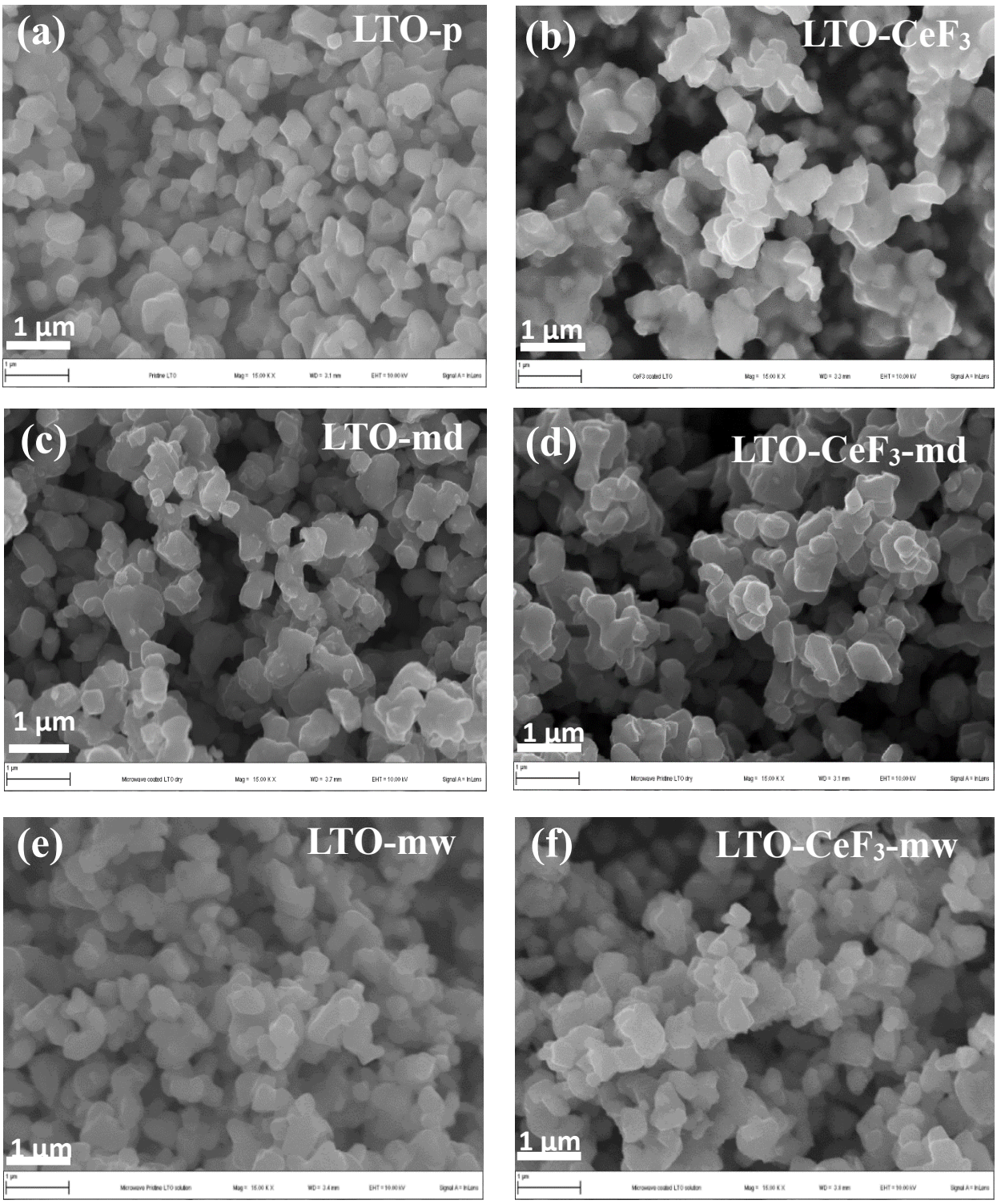


Figure 4.16: SEM image of (a) LTO-p, (b) LTO-CeF_3, (c) LTO-md, (d) LTO-CeF_3-md, (e) LTO-mw, and (d) LTO-CeF_3-mw.

4.2.2 Electrochemical measurements

4.2.2.1 Cyclic voltammetry (CV)

Figure 4.17 displays cyclic voltammograms (CV) of LTO-p, LTO-CeF_3, LTO-md, LTO-CeF_3 LTO-mw and LTO-CeF_3-mw on a voltage window of 1.0–2.5 V versus Li/Li^+ performed at 0.1 mVs^{-1} (room temperature). The materials were compared using uncoated material against coated material of the same microwave status. All the materials displayed a pair of redox peaks relating to the valence state conversion between Ti^{4+} and Ti^{3+} of spinel LTO [69]. To study the redox reactions of the materials closely, CV parameters obtained from Figure 4.17 are outlined in Table 4.3. The table focuses on the (i) peak-to-peak separation voltage (E_{pp} / V), indicating the electron transfer kinetics of the cells; (ii) the heights of the anodic (I_{pa} / mA) and cathodic (I_{pc}/mA) peak current, which represents the mass transport and redox dynamics, and (iii) the peak current ratio (I_{pa}/I_{pc}), which outlined the reversibility or Coulombic efficiency of the cells [64].

Three observations were made from CV parameters. Firstly, one can observe that the coated materials possessed lower peak-to-peak separation than the uncoated materials, indicating that coated materials had lower polarization effects and faster electronic transfer properties [70]. This electrochemical enhancement may be attributed to the good ionic conductivity of CeF_3. Microwave irradiated materials seem to have less to no effect on peak-to-peak separation. The second observation is that the coated materials exhibited high peak current or higher current response, which is linked to higher mass transport of electrolyte ions across and within their structures, and the ionic/electronic charge-transfer kinetics at the electrode-electrolyte interface. The coated materials have this property because of high ionic conductivity of CeF_3. LTO-CeF_3-mw had the highest mass transport and/or charge-transfer kinetics, which highlights the improved

electrochemical kinetics as a result of the combination of CeF_3 surface coating and microwave radiation.

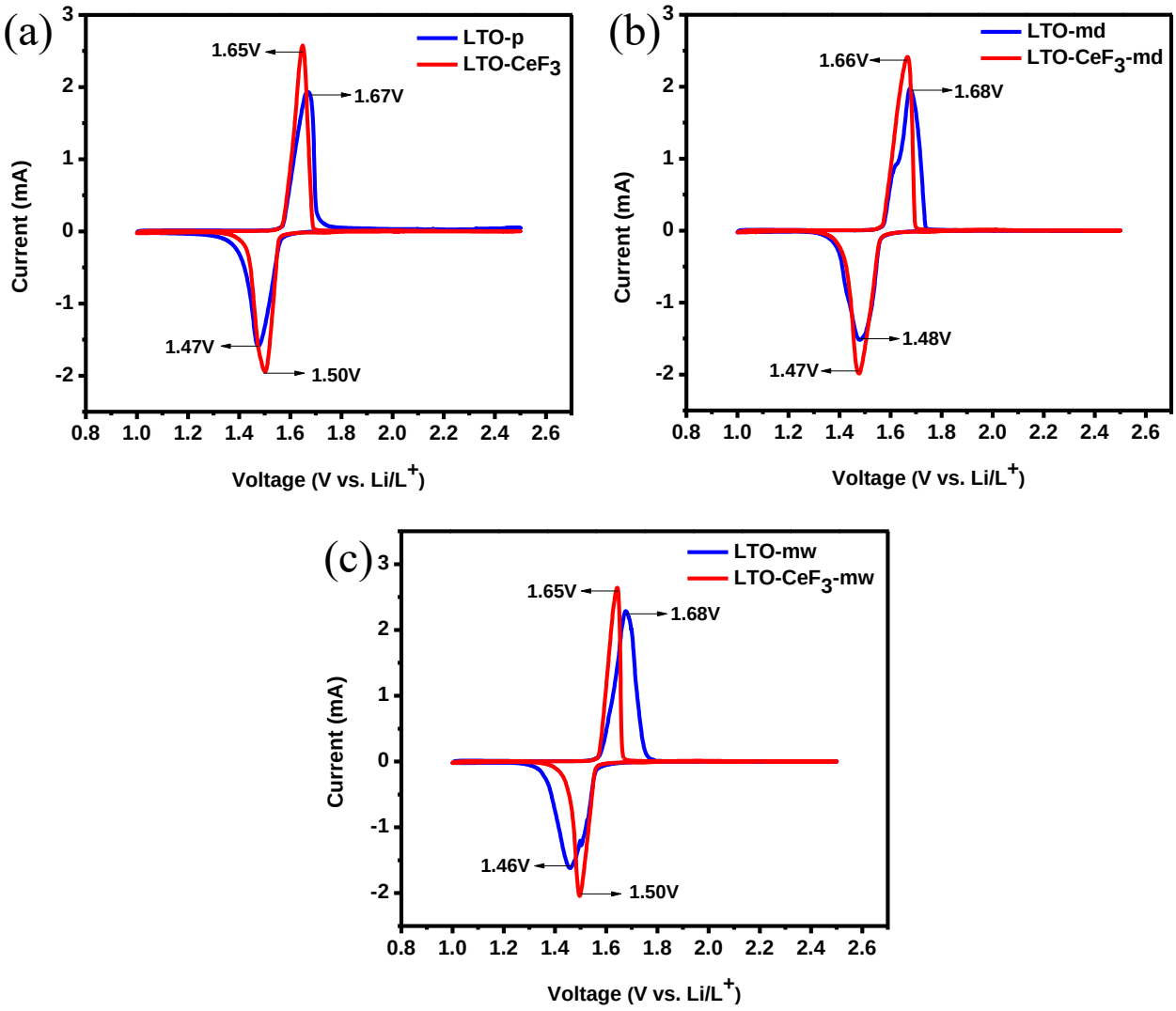


Figure 4.17**:** CV plots of the materials at 0.1 mVs^{-1} of (a) LTO-p, LTO-CeF_3, (b) LTO-md, LTO-CeF_3, and (c) LTO-mw, LTO-CeF_3-mw.

The last observation from peak current ratios of the materials in Table 4.3 Pristine LTO and LTO-CeF_3-md have lower ratio values close to the theoretical value of I_{pa}/I_{pc}=1.0. These indicate that

these two materials have higher Coulombic efficiency than all the materials followed by LTO-md and LTO-CeF_3, then by LTO-CeF_3-mw and lastly LTO-mw.

Table 4.3: CV redox reaction parameters for the samples.

Electrode	E_{pa}/V	E_{pc}/V	E /V	I_{pa}/Ma	I_{pc}/Ma	I_{pa}/ I_{pc}
LTO-p	1.67	1.47	0.20	1.91	1.57	1.22
LTO-md	1.68	1.48	0.20	1.97	1.52	1.30
LTO-mw	1.68	1.46	0.22	2.28	1.58	1.44
LTO-CeF_3	1.65	1.50	0.15	2.53	1.94	1.30
LTO-CeF_3-md	1.66	1.47	0.19	2.40	1.96	1.22
LTO-CeF_3-mw	1.65	1.50	0.15	2.59	1.98	1.31

4.2.2.2 Galvanostatic charge-discharge (GCD)

Figure 4.18 displays the charge-discharge curves of LTO-p, LTO-CeF_3, LTO-md, LTO-CeF_3 LTO-mw and LTO-CeF_3-mw. The materials were cycled at 1C and observed on the 1st and 100th cycles. All the materials revealed a relatively flat voltage plateau approximately at 1.60 V, which is linked to the working potential of LTO. The specific discharge capacity of the first and the 100th cycles are shown in Table 4.4. On the table, coated materials exhibit higher specific discharge capacity in 2 out of 3 pairs of the subclasses (coated against uncoated). At the first cycle, the LTO-p/LTO-CeF_3 pair produced 114.97/145.71 $mAhg^{-1}$ capacities while LTO-md/LTO-CeF_3-md produced 162.53/163.65 $mAhg^{-1}$. It was only in the LTO-mw/LTO-CeF_3-mw pair that the uncoated material had a higher capacity of 224.88/194.59 $mAhg^{-1}$. The capacity increased with the microwave status in each subclass of materials. For instance, on the first cycles, pristine LTO-p, LTO-md and LTO-mw exhibited 114.97, 162.53 and 224 $mAhg^{-1}$, respectively. These results show that surface coating and microwave radiation when combined or used separately, improved the specific capacity of LTO. Under these testing conditions, all materials had good capacity retention, with more than 98 % retention at the 100th cycle, as indicated in Figure 4.19. The samples also exhibited more than 98% coulombic efficiency even at the 100th cycle with LTO- CeF_3 and LTO-CeF_3-mw having the highest efficiencies of 99.34% and 99.42%, respectively, which from material characterizations studies, highlight the expected improved electrochemical performance by CeF_3 coating and microwave irradiation.

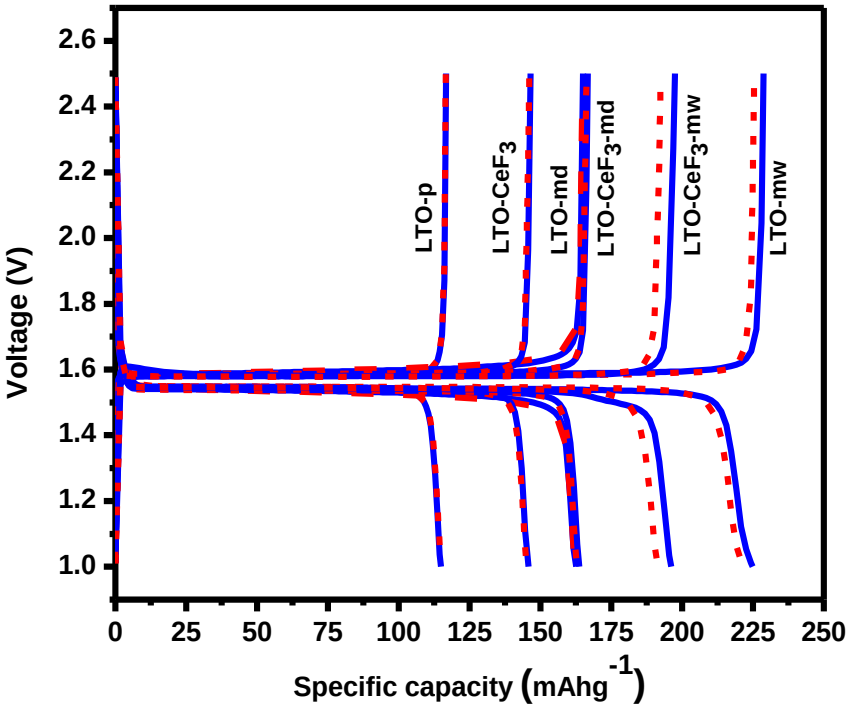


Figure 4.18**:** Charge/discharge of all materials at 1C for 100 cycles.

Table 4.4: Specific capacities at 1st and 100th cycles.

Electrode	1st cycle (mAh g^{-1})	100th cycle (mAh $g^{-1)}$
LTO-p	114.97	114.89
LTO-md	162.53	162.19
LTO-mw	224.88	221.37
LTO-Ce$\mathbf{F_3}$	145.71	145.06
LTO-Ce$\mathbf{F_3}$-md	163.65	162.82
LTO-Ce$\mathbf{F_3}$-mw	194.59	191.23

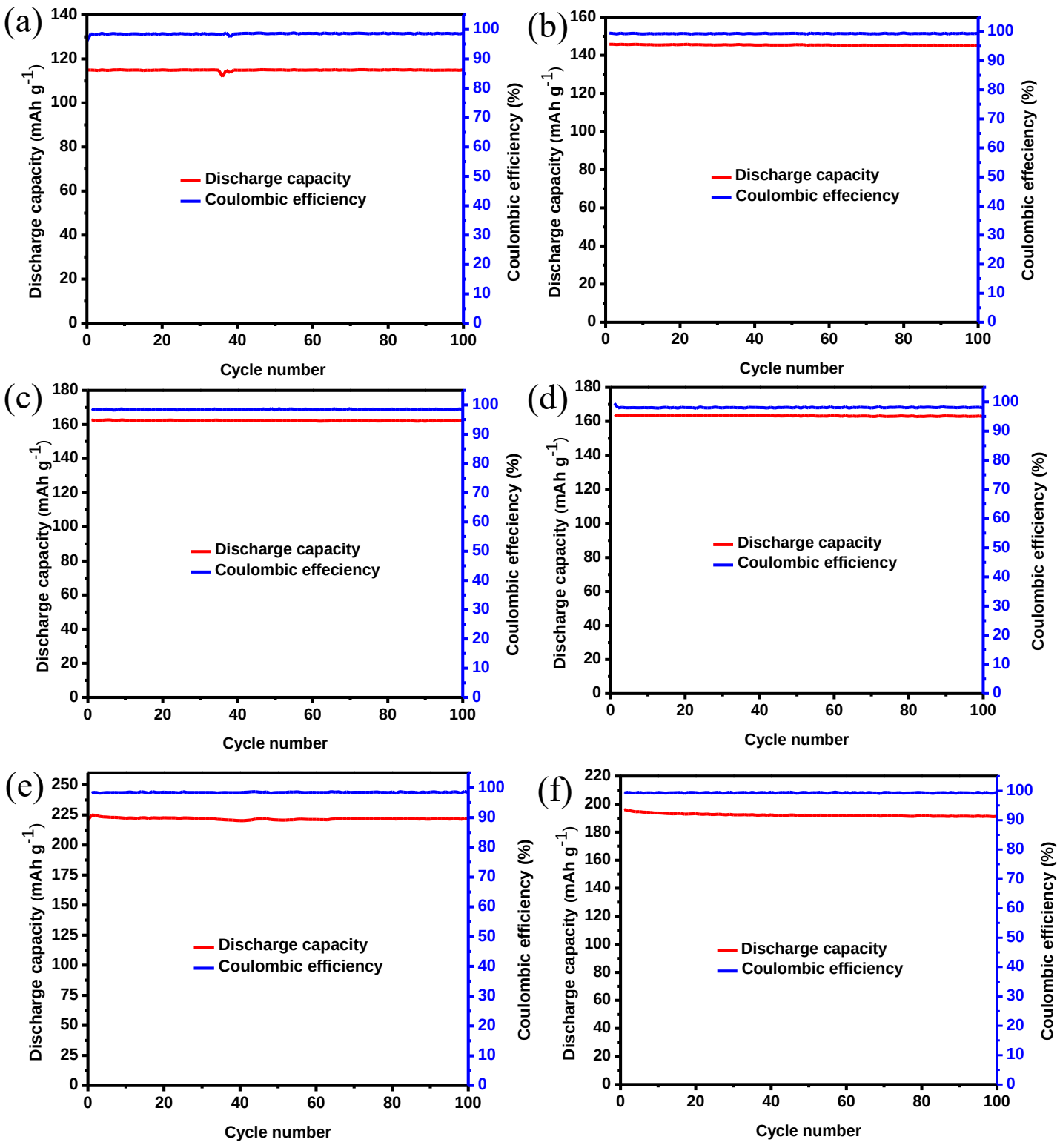


Figure 4.19**:** Discharge capacity and coulombic efficiency of (a) LTO-p, (b) LTO-CeF_3, (c) LTO-md, (d) LTO-CeF_3-md, (e) LTO-mw, and (f) LTO-CeF_3-mw at 1C for 100 cycles.

Since LTO is considered for future applications that require high-power outputs, the samples were further cycled at 5C and studied for 1000 cycles in Figure 4.20. The discharge capacities obtained under these testing conditions are shown in Figure 4.21 (together with Coulombic efficiencies) and tabulated in Table 4.5. Microwave irradiation alone increased the specific capacity of the LTO materials. For instance, the uncoated materials, LTO-p, LTO-md and LTO-mw, gave 128.90, 139.73 and 147.91 mAh g^{-1} capacities, respectively. But the microwave technique introduced high-capacity degradation after 600 cycles. Application of CeF_3 coating solely enhanced the LTO capacity but with a cost of high-capacity fade even before 500 cycles (after 400 cycles). The degradation offered by surface coating was compensated for by the positive microwave radiation effect.

A decline in capacity was observed after 500 cycles in LTO-CeF_3-md while LTO-CeF3-mw experienced no capacity fade even at the 1000th cycle. Combining surface coating and microwave treatment in water creates a stable material; this was seen in LTO-CeF_3-mw which possessed the highest capacity of 167.34 mAh g^{-1} at both 500 and 1000 cycles. The same capacity increase trend of dry irradiated materials (-md) having higher capacities than nonirradiated materials, and water treated irradiated materials (-mw) having the highest capacities at 1C for 100 cycles, occurred at 5C, but the difference was that LTO-CeF_3-mw had the highest capacity. Pristine LTO and LTO-CeF_3-mw had superior Coulombic efficiencies through cycling while other materials had fluctuating efficiencies with respect to their high-capacity losses.

Table 4.5: Specific capacities for 5C cycling.

Electrode	Cycle 1 (mAh g^{-1})	Cycle 500 (mAh g^{-1})	Cycle 1000 (mAh g^{-1})
LTO-p	128.90	109.37	114.47
LTO-md	139.74	132.81	7.39
LTO-mw	147.91	145.72	7.33
LTO-Ce$\mathbf{F_3}$	145.36	35.26	2.77
LTO-Ce$\mathbf{F_3}$-md	134.67	115.78	14.16
LTO-Ce$\mathbf{F_3}$-mw	162.49	167.34	167.34

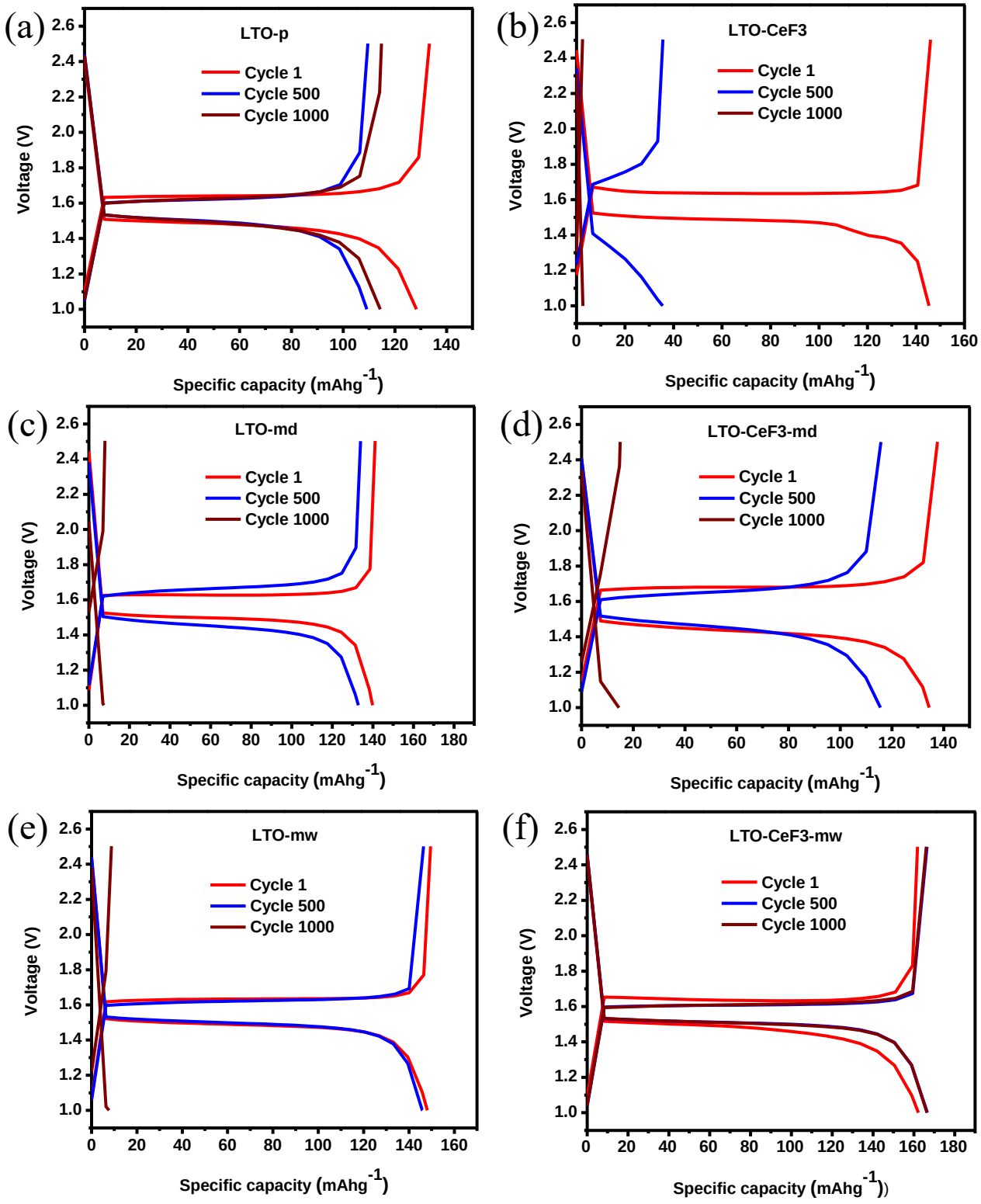


Figure 4.20**:** Charge/discharge plots of (a) LTO-p, (b) LTO-CeF_3, (c) LTO-md, (d) LTO-CeF_3-md, (e) LTO-mw, and (f) LTO-CeF_3-mw at 5C for 1000 Cycles.

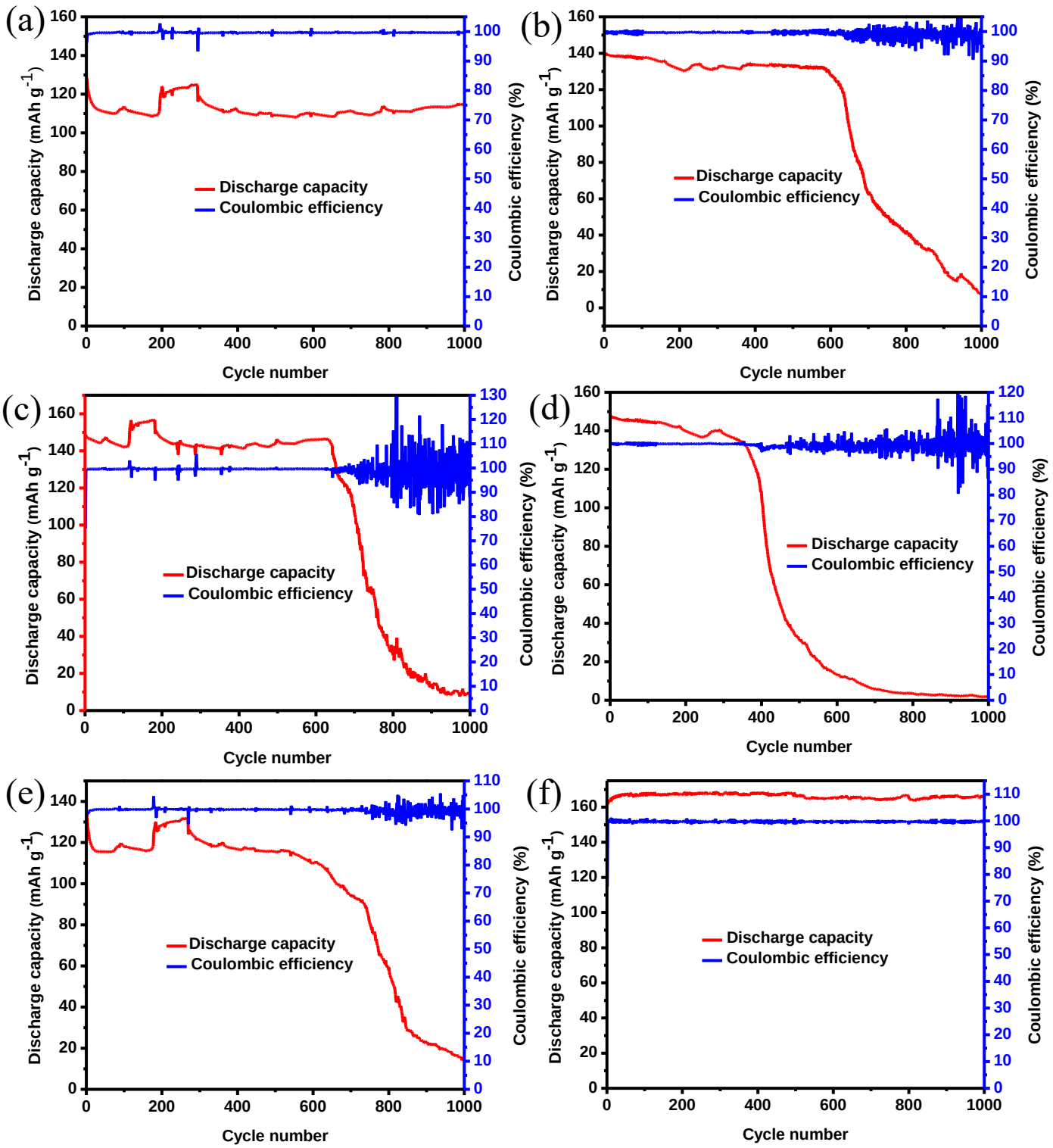


Figure 4.21**:** Discharge capacity and coulombic efficiency of (a) LTO-p, (b) LTO-CeF_3, (c) LTO-md, (d) LTO-CeF_3-md, (e) LTO-mw, and (f) LTO-CeF_3-mw at 5C for 1000 Cycles.

4.2.2.3 Rate capability

Rate capability of the materials is displayed in Figure 4.22 for 0.5C, 1.0C, 3C, 10C, 20C, 30C, 50C and again 0.5C. All the microwave irradiated materials and coated materials exhibited greater specific capacities than pristine LTO until 20C, with LTO-p having greater specific capacity than LTO-md, LTO-mw, LTO-CeF_3-md at a high rate 30C and 50C. LTO-CeF_3-mw has a higher and good rate capability at these C rates than all the materials. Microwave irradiation introduced capacity fade at higher rates for most of the materials namely: LTO-md, LTO-mw and LTO-CeF_3-md. However, the best results were recorded when combined with surface coating and in a wet environment with the presence of water. This performance corresponds to the one found on 5C cycling for 1000 circles, where LTO-CeF_3-mw performed best.

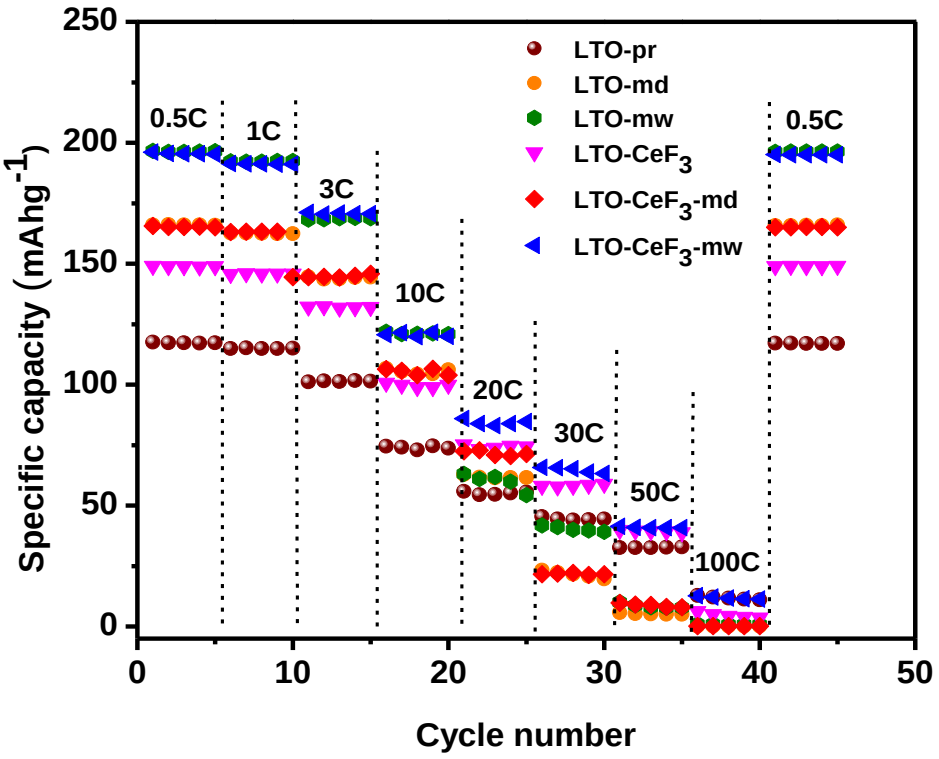


Figure 4.22**:** Rate capability of the LTO-p, LTO-CeF_3, LTO-md, LTO-CeF_3-md, LTO-mw, and LTO-CeF_3-mw.

4.2.2.4 Electrochemical impedance spectroscopy (EIS)

To further clarify the effects of CeF_3 and microwave irradiation on the electrochemistry of the materials, the resistance and kinetics at different parts of the battery systems were studied using EIS. Figure 4.23 contains the Nyquist plots of all the materials before and after cycling. Before cycling, all the materials had one high to medium frequency semicircle and one low frequency sloped line. After cycling, two partly overlapped and depressed semicircles were observed at the high to medium frequency regions for all the materials besides LTO-p, which had the same EIS curve shape as before cycling. Figure 4.24 show the equivalent circuits [71] utilized in fitting the

data. Table 4.6 presents the values of the EIS parameters that were obtained from equivalent circuits before cycling. The EIS parameters are made up of the solution resistance (R_s) attributed to the electrolyte's ohmic resistance and the charge-transfer resistance (R_{CT}) at the intermediate frequency regions, highlighting the Li^+ ions exchange dynamics at the electrode surface. The C_{dl} indicates the double-layer capacitances and Warburg impedance (W) offers insight on the impedance of Li^+ ion diffusion into the electrode materials. The R_{SEI} signifies the high-frequency resistance caused by the solid electrolyte interface (SEI) and the constant phase element (CPE) indicates the interfacial capacitance.

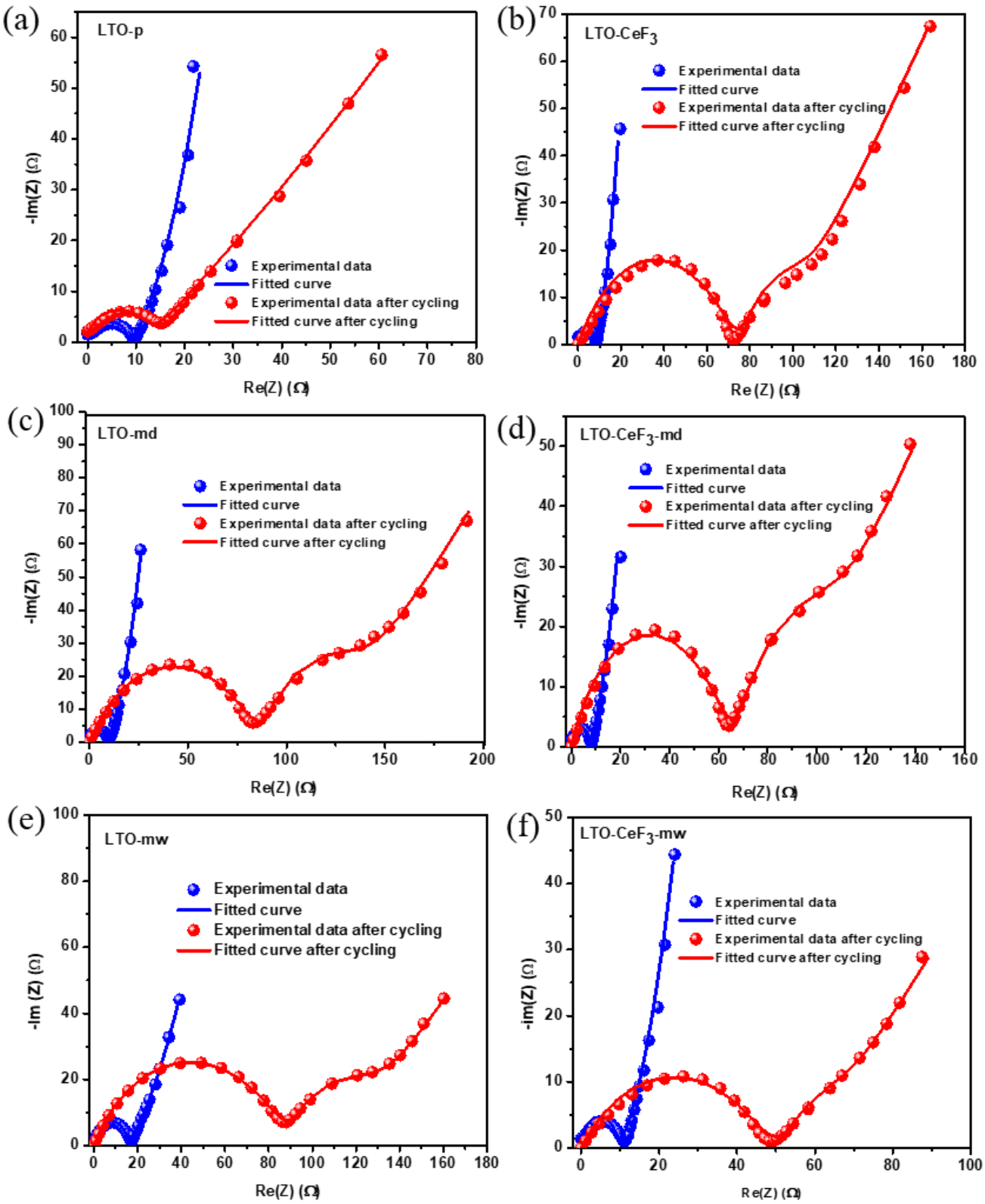


Figure 4.23: Nyquist plots before and after 1000 cycles of (a) LTO-p, (b) LTO-CeF_3, (c) LTO-md, (d) LTO-CeF_3-md, (e) LTO-mw, and (f) LTO-CeF_3-mw.

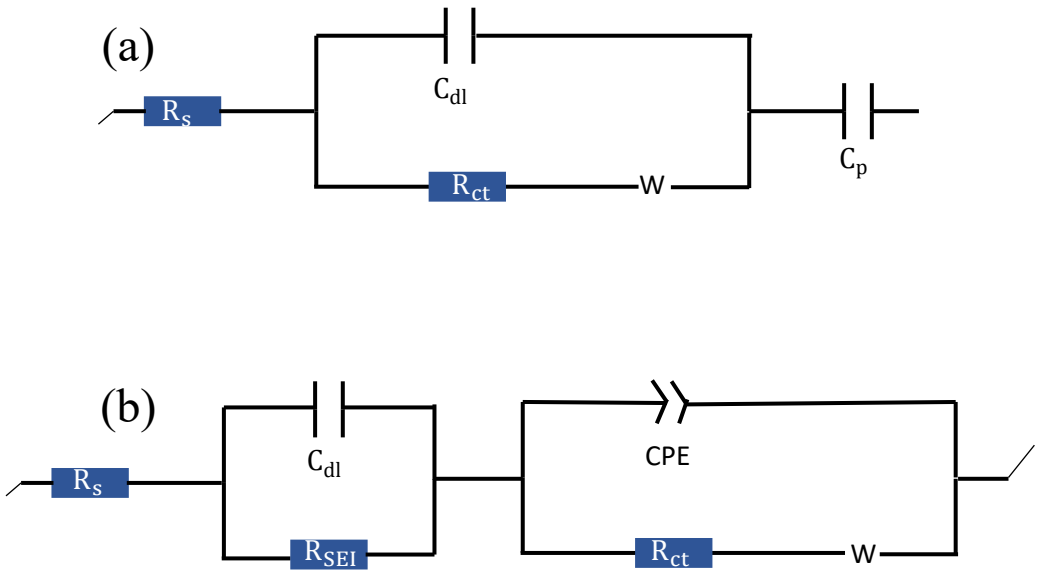


Figure 4.24**:** Equivalent circuit of the materials (a) before cycling and only after cycling for LTO-p, and (b) After cycling.

The solution resistance registered by the electrodes differ; meanwhile the same electrolyte was used, which indicates that the electrodes with lower solution resistance had better wettability [72]. LTO-CeF_3 had lower R_s values of 5.34 Ω, and LTO-CeF_3 offered the highest value of 17.08 Ω, before cycling. Since the cell impedance is primarly ascribed to charge transfer resistance, the study of this parameter was used to evaluate the overall impedance of the systems. The R_{ct} of the materials before cycling was LTO-p (8.35 Ω), LTO-md, (8.65 Ω), LTO-mw (15.15 Ω) and for CeF_3 coated materials was LTO- CeF_3 (7.07 Ω), LTO- CeF_3-md (6.94 Ω) and LTO- CeF_3-mw (9.38 Ω). The coated materials had less charge-transfer resistance than the uncoated materials, implying improved electrical conductivity by the coated CeF_3.

Table 4.6: EIS parameters for materials before 1000 electrochemical cycling experiments.

Parameter	LTO-p	LTO-md	LTO-mw	LTO-CeF_3	LTO-CeF_3-md	LTO-CeF_3-mw
R_s / Ω	6.586	6.831	8.782	5.342	17.08	10.46
	± 0.364 8	± 0.337 2	± 0.382 4	± 0.341 1	± 0.344 6	± 0.380 5
C1/ F	$32.98e^{-6}$	$25.69e^{-6}$	$26.95e^{-6}$	$32.32e^{-6}$	$33.27e^{-6}$	$38.65e^{-6}$
	± $9.699e^{-6}$	± $7.186e^{-6}$	± $4.311e^{-6}$	± $11.1e^{-6}$	± $11.69e^{-6}$	± $10.11e^{-6}$
R_{ct} / Ω	8.353	8.654	15.15	7.07	6.943	9.38
	± 0.491 1	± 0.384 2	± 0.444 7	± 0.389	± 0.394 2	± 0.443 2
Z_w /Ω $s^{-0.5}$	3.581	4.279	6.875	2.794	4.404	4.245
	± 0.246 3	± 0.179 9	± 0.205 1	± 0.180 6	± 0.237 7	± 0.262 1
S	0.453 3	0.426 8	0.563 4	0.541 3	0.388 2	0.393 7
	± 0.051 15	± 0.029 62	± 0.052 72	± 0.047 66	± 0.037 33	± 0.039 02

The impedance of the materials LTO-p, LTO-md, LTO-mw, LTO-CeF_3, LTO-CeF_3-md, and LTO-CeF_3-mw was observed after 1000 cycles. The obtained EIS parameters are presented in Table 4.7. The materials had LTO-p (12 Ω), LTO-md (89.7 Ω), LTO-mw (91.1 Ω), LTO-CeF_3 (77.88 Ω), LTO-CeF_3-md (66.5 Ω) and LTO-CeF_3-mw (53.39 Ω) charge transfer resistance. LTO-p had the lowest charge transfer resistance, signifying that the electrical conductivity of the modified materials decreased with cycling. Amongst the modified materials, LTO-CeF_3-mw possessed lower charge transfer resistance. Another interesting observation from the impedance studies was the observed resistance from the SEI layer on all the modified materials besides LTO-p after

cycling, which explains why LTO-p possess the same EIS shape and equivalent circuit even after cycling. LTO-CeF_3-mw offered a smaller SEI resistance of 6.68 Ω, than 32.1, 24.28,16.44 and 22.79 Ω of LTO-md, LTO-mw, LTO-CeF_3 and LTO-CeF3, respectively. This implies that this material can minimize the cell degradation effect caused by the build-up of charge carriers on the SEI layer. These impedance results corroborate the high-capacity retention observed for LTO-p and LTO-CeF_3-mw when charged and discharged for 1000 cycles.

Table 4.7: EIS parameters for materials after 1000 electrochemical cycling experiments.

Parameter	LTO-p	LTO-md	LTO-mw	LTO-CeF_3	LTO-CeF_3-md	LTO-CeF_3-mw
R_s / Ω	10.61 ± 0.340 9	17.21 ± 0.280 9	10.33 ± 0.316	29.12 ± 0.258 4	8.046 ± 0.051 61	14.86 ± 0.549 5
C_1/ F	$16.68e^{-6}$ ± $3.558e^{-6}$	$8.441e^{-3}$ ± $1.28e^{-3}$	$7.281e^{-3}$ ± $1.421e^{-3}$	0.016 54 ± $4.922e^{-3}$	0.011 9 ± $2.595e^{-3}$	0.037 28 ± 0.028 73
R_{SEI} / Ω		32.1 ± 0.846	24.28 ± 1.206	16.44 ± 1.16	22.79 ± 2.355	6.679 ± 1.806
Q / F.$s^{(a-1)}$		$50.9e^{-6}$ ± $11.6e^{-6}$	$46.08e^{-6}$ ± $9.934e^{-6}$	$65.02e^{-6}$ ± $17.43e^{-6}$	$42.9e^{-6}$ ± $12.98e^{-6}$	$0.110\ 3e^{-3}$ ± $44.91e^{-6}$
a		0.719 3	0.742 4	0.693 4	0.764 1	0.660 33
R_{ct} / Ω	12 ± 0.406 8	89.7 ± 2.068	91.1 ± 1.991	77.88 ± 2.13	66.5 ± 1.725	53.39 ± 2.304
Z_w / Ω $s^{-0.5}$	46.89 ± 1.383	26.99 ± 0.533 6	26.65 4 ± 1.096	21.5 ± 0.364 6	28.72 ± 1.218	17.72 ± 1.186
C_2 / F	0.154 5 ± 0.071 34					

4.3 Conclusion

This study modified a commercial LTO using CeF_3 coating and microwave irradiation. CeF_3 was found to be on the surface of LTO-CeF_3 and LTO-CeF_3-mw on the TEM micrographs. Some portion of the CeF_3 co-doped inside the LTO phase via substitution and formed composite of LTO and anatase TiO_2. The composite promoted high grain boundaries observed on the HRTEM image of LTO-CeF_3 which in turn promoted its high specific capacity. The coated materials and irradiated materials contained mixed states of Ti^{4+} and $Ti^{3+,}$ which granted these materials high electronic conductivity than LTO-p, which only included the titanium in Ti^{4+} form. Cyclic voltammograms indicated that the coated materials have lower polarization and faster electronic transfer. Furthermore, the CV analyses demonstrated that the coated materials exhibited higher current responses. All the modified materials had higher specific capacity under rate capability and charge-discharge studies, regardless of the cycle numbers. LTO-p demonstrated an excellent capacity retention when studied at high rates for long cycles (1000 cycles), while the modified materials besides LTO-CeF_3-mw experienced huge degradation, especially after 500 cycles. LTO-CeF_3-mw had the highest capacity of 163 mAh g^{-1} at the 1000^{th} cycle. LTO-p possessed the lowest charge-transfer resistance with no SEI impedance observed. All the materials encountered SEI resistance, but LTO-CeF_3-mw gave the lowest resistance for both charge transfer and SEI on the modified samples. The results confirmed that CeF_3 coating was efficient in increasing the electronic conductivity of LTO and together with solution microwave irradiation, made LTO-CeF_3-mw to have superior aggregated electrochemical performance.

4.4 References

[1] Lu, L., Han, X., Li, J., Hua, J. & Ouyang, M.J.J.O.P.S. 2013. A review on the key issues for lithium-ion battery management in electric vehicles. 226**,** 272-288.

[2] Jiang, X., Chen, Y., Meng, X., Cao, W., Liu, C., Huang, Q., Naik, N., Murugadoss, V., Huang, M. & Guo, Z. 2022. The impact of electrode with carbon materials on safety performance of lithium-ion batteries: A review. *Carbon*.

[3] Chen, Z., Yan, Y., Xin, S., Li, W., Qu, J., Guo, Y.G. & Song, W.G. 2013. Copper germanate nanowire/reduced graphene oxide anode materials for high energy lithium-ion batteries. *Journal of Materials Chemistry A*, 1**,** 11404-11409.

[4] Gauthier, N., Courrèges, C., Demeaux, J., Tessier, C. & Martinez, H. 2020. Probing the in-depth distribution of organic/inorganic molecular species within the SEI of LTO/NMC and LTO/LMO batteries: A complementary ToF-SIMS and XPS study. *Applied Surface Science*, 501**,** 144266.

[5] Yan, B., Li, M., Li, X., Bai, Z., Yang, J., Xiong, D. & Li, D. 2015. Novel understanding of carbothermal reduction enhancing electronic and ionic conductivity of Li 4 Ti 5 O 12 anode. *Journal of Materials Chemistry A*, 3**,** 11773-11781.

[6] Yu, A., Gong, D., Zhang, M. & Tang, Y. 2020. In-situ implanted carbon nanofilms into lithium titanate with 3D porous structure as fast kinetics anode for high-performance dual-ion battery. *Chemical Engineering Journal*, 401**,** 125834.

[7] Amine, K., Belharouak, I., Chen, Z., Tran, T., Yumoto, H., Ota, N., Myung, S.T. & Sun, Y.K. 2010. Nanostructured anode material for high-power battery system in electric vehicles. *Advanced Materials*, 22**,** 3052-3057.

[8] Ohzuku, T., Ueda, A. & Yamamoto, N. 1995. Zero-strain insertion material of Li [Li1/3Ti5/3] O 4 for rechargeable lithium cells. *Journal of the Electrochemical Society,* 142**,** 1431.

[9] Nakahara, K., Nakajima, R., Matsushima, T. & Majima, H. 2003. Preparation of particulate Li4Ti5O12 having excellent characteristics as an electrode active material for power storage cells. *Journal of Power Sources,* 117**,** 131-136.

[10] Shen, L., Uchaker, E., Zhang, X. & Cao, G. 2012. Hydrogenated Li4Ti5O12 nanowire arrays for high rate lithium ion batteries. *Advanced Materials,* 24**,** 6502-6506.

[11] Zhu, G.N., Liu, H.J., Zhuang, J.H., Wang, C.X., Wang, Y.G. & Xia, Y.Y. 2011. Carbon-coated nano-sized Li 4 Ti 5 O 12 nanoporous micro-sphere as anode material for high-rate lithium-ion batteries. *Energy Environmental Science,* 4**,** 4016-4022.

[12] Chaturvedi, P., Kanagaraj, A.B., Al Nahyan, M.S., Al Shibli, H., Ashoor, A.A., Fadaq, H., Al Dahmani, S. & Choi, D.S. 2019. Electrical and electrochemical properties of carbon nanotube-based free standing LTO electrodes for current collector-free Li-ion batteries. *Current Applied Physics,* 19**,** 1150-1155.

[13] Mo, L. & Zheng, H. 2020. Solid coated Li4Ti5O12 (LTO) using polyaniline (PANI) as anode materials for improving thermal safety for lithium ion battery. *Energy Reports,* 6**,** 2913-2918.

[14] Bernhard, R., Meini, S. & Gasteiger, H.A. 2014. On-line electrochemical mass spectrometry investigations on the gassing behavior of Li4Ti5O12 electrodes and its origins. *Journal of the Electrochemical Society,* 161**,** A497.

[15] Qin, Y., Chen, Z., Belharouak, I. & Amine, K.J.a.N.L.P. 2011. Mechanism of LTO Gassing and potential solutions. 18.

[16] Jo, M.R., Nam, K.M., Lee, Y., Song, K., Park, J.T. & Kang, Y.M. 2011. Phosphidation of Li4Ti5O12 nanoparticles and their electrochemical and biocompatible superiority for lithium rechargeable batteries. *Chemical Communications,* 47**,** 11474-11476.

[17] Odziomek, M., Chaput, F., Rutkowska, A., Świerczek, K., Olszewska, D., Sitarz, M., Lerouge, F. & Parola, S. 2017. Hierarchically structured lithium titanate for ultrafast charging in long-life high capacity batteries. *Nature communications,* 8**,** 1-7.

[18] Ge, H., Hao, T., Zhang, B., Chen, L., Cui, L. & Song, X.-M. 2016. Nanoparticles-constructed spinel Li4Ti5O12 with extra surface lithium storage capability towards advanced lithium-ion batteries. *Electrochimica Acta,* 211**,** 119-125.

[19] Setiawan, D., Subhan, A. & Saptari, S. Ca-doped LTO using waste eggshells as Ca source to improve the discharge capacity of anode material for lithium-ion battery. AIP Conference Proceedings, 2017. AIP Publishing LLC, 030073.

[20] Wang, W., Jiang, B., Xiong, W., Wang, Z. & Jiao, S. 2013. A nanoparticle Mg-doped Li4Ti5O12 for high rate lithium-ion batteries. *Electrochimica acta,* 114**,** 198-204.

[21] Qian, D., Gu, Y., Chen, Y., Liu, H., Wang, J. & Zhou, H. 2019. Ultra-high specific capacity of Cr3+-doped Li4Ti5O12 at 1.55 V as anode material for lithium-ion batteries. *Materials letters,* 238**,** 102-106.

[22] Zou, S., Wang, G., Zhang, Y., Xue, C., Chen, H., Yang, G., Nan, H., Wei, H. & Lin, H. 2020. Nano-structure and characterization of carbon composite with Al3+ and Mn4+ co-doped Li4Ti5O12 as anodes for Li-ion batteries. *Journal of Alloys Compounds,* 816**,** 152609.

[23] Jung, H.G., Myung, S.T., Yoon, C.S., Son, S.B., Oh, K.H., Amine, K., Scrosati, B. & Sun, Y.K. 2011. Microscale spherical carbon-coated Li 4 Ti 5 O 12 as ultra high power anode material for lithium batteries. *Energy Environmental Science,* 4**,** 1345-1351.

[24] Kim, K.T., Yu, C.Y., Yoon, C.S., Kim, S.J., Sun, Y.K. & Myung, S.T. 2015. Carbon-coated Li4Ti5O12 nanowires showing high rate capability as an anode material for rechargeable sodium batteries. *Nano Energy,* 12**,** 725-734.

[25] Zhao, L., Hu, Y.S., Li, H., Wang, Z. & Chen, L. 2011. Porous Li4Ti5O12 coated with N-doped carbon from ionic liquids for Li-ion batteries. *Advanced Materials,* 23**,** 1385-1388.

[26] Han, B. & Lu, X. 2009. Effect of nano-sized CeF3 on microstructure, mechanical, high temperature friction and corrosion behavior of Ni–W composite coatings. *Surface Coatings Technology,* 203**,** 3656-3660.

[27] Dorai, A.K., Subramanian, S., Hellar, N. & Leiro, J. 2014. Influence of substrate temperature on CeF3 thin films prepared by thermal evaporation. *Materials Chemistry Physics,* 143**,** 765-772.

[28] Xie, Y., Gao, D., Zhang, L., Chen, J., Cheng, S. & Xiang, H. 2016. CeF3-modified LiNi1/3Co1/3Mn1/3O2 cathode material for high-voltage Li-ion batteries. *Ceramics International,* 42**,** 14587-14594.

[29] Wu, C., Wang, Y., Ma, G. & Zheng, X. 2021. Enhanced rate capability of Li4Ti5O12 anode material by a photo-assisted sol–gel route for lithium-ion batteries. *Electrochemistry Communications,* 131**,** 107119.

[30] Qin, W., Liu, H., An, J. & Wen, X.J.J.O.P.S. 2020. Enhanced Li-ion battery performance of TiO2 nanoparticle-loaded Li4Ti5O12 nanosheet anode using carbon coated copper as current collector. 479**,** 229090.

[31] Tsubone, D., Hashimoto, T., Igarashi, K. & Shimizu, T. 1994. Electrical characterization of phase changes in lithium titanate. *Journal of the Ceramic Society of Japan,* 102**,** 180-184.

[32] Cheng, L., Li, X.L., Liu, H.J., Xiong, H.M., Zhang, P.W. & Xia, Y.Y. 2007. Carbon-coated Li4Ti5O12 as a high rate electrode material for Li-ion intercalation. *Journal of the Electrochemical Society,* 154**,** A692.

[33] Gao, J., Gong, B., Zhang, Q., Wang, G., Dai, Y. & Fan, W. 2015. Study of the surface reaction mechanism of Li 4 Ti 5 O 12 anode for lithium-ion cells. *Ionics,* 21**,** 2409-2416.

[34] Zhang, Q., Liu, Y., Lu, H., Tang, D., Ouyang, C. & Zhang, L. 2016. Ce3+-doped Li4Ti5O12 with CeO2 surface modification by a sol-gel method for high-performance lithium-ion batteries. *Electrochimica acta,* 189**,** 147-157.

[35] Zhou, T., Feng, X., Guo, X., Wu, W., Cheng, S. & Xiang, H. 2015. Solid-state synthesis and electrochemical performance of Ce-doped Li4Ti5O12 anode materials for lithium-ion batteries. *Electrochimica acta,* 174**,** 369-375.

[36] Chung, Y., Shin, Y., Liu, Y., Park, J.S., Margez, C.L. & Greszler, T.A. 2019. Synergetic effect of carbon and AlF3 coatings on the lithium titanium oxide anode material for high power lithium-ion batteries. *Journal of Electroanalytical Chemistry,* 837**,** 240-245.

[37] Li, D., Liu, Y., Zhao, W., Gao, Y., Cao, L., Liu, Y., Wang, W., Yi, L. & Qi, T. 2019. Synthesis of Ce modified Li4Ti5O12 using biomass as carbon source. *Journal of Electroanalytical Chemistry,* 851**,** 113441.

[38] Li, W., Li, X., Chen, M., Xie, Z., Zhang, J., Dong, S. & Qu, M. 2014. AlF3 modification to suppress the gas generation of Li4Ti5O12 anode battery. *Electrochimica Acta,* 139**,** 104-110.

[39] Feng, J., Huang, Z., Guo, C., Chernova, N.A., Upreti, S. & Whittingham, M.S. 2013. An organic coprecipitation route to synthesize high voltage LiNi0. 5Mn1. 5O4. *ACS applied materials interfaces,* 5**,** 10227-10232.

[40] Ncube, N.M., Mhlongo, W.T., Mccrindle, R.I. & Zheng, H. 2018. The electrochemical effect of Al-doping on Li4Ti5O12 as anode material for lithium-ion batteries. *Materials Today: Proceedings,* 5**,** 10592-10601.

[41] Julien, C.M. & Mauger, A. 2018. In situ Raman analyses of electrode materials for Li-ion batteries. *AIMS Materials Science,* 5**,** 650-698.

[42] Liao, J.Y., Chabot, V., Gu, M., Wang, C., Xiao, X. & Chen, Z. 2014. Dual phase Li4Ti5O12–TiO2 nanowire arrays as integrated anodes for high-rate lithium-ion batteries. *Nano Energy,* 9**,** 383-391.

[43] Liu, Z., Zhang, N., Wang, Z. & Sun, K. 2012. Highly dispersed Ag nanoparticles (< 10 nm) deposited on nanocrystalline Li4Ti5O12 demonstrating high-rate charge/discharge capability for lithium-ion battery. *Journal of Power Sources,* 205**,** 479-482.

[44] Cheng, C., Liu, H., Xue, X., Cao, H. & Shi, L. 2014. Highly dispersed copper nanoparticle modified nano Li4Ti5O12 with high rate performance for lithium ion battery. *Electrochimica acta,* 120**,** 226-230.

[45] Yoon, J.K., Nam, S., Shim, H.C., Park, K., Yoon, T., Park, H.S. & Hyun, S. 2018. Highly-stable Li4Ti5O12 anodes obtained by atomic-layer-deposited Al2O3. *Materials,* 11**,** 803.

[46] Sun, X., Hegde, M., Zhang, Y., He, M., Gu, L., Wang, Y., Shu, J., Radovanovic, P.V. & Cui, B. 2014. Structure and electrochemical properties of spinel Li4Ti5O12 nanocomposites as anode for lithium-ion battery. *Int. J. Electrochem. Sci,* 9**,** 1583-1596.

[47] Qin, M., Li, Y. & Lv, X.J. 2017. Preparation of Ce-and La-doped Li4Ti5O12 nanosheets and their electrochemical performance in Li half cell and Li4Ti5O12/LiFePO4 full cell batteries. *Nanomaterials,* 7**,** 150.

[48] Jiang, Y.M., Wang, K.X., Zhang, H.J., Wang, J.F. & Chen, J.S. 2013. Hierarchical Li4Ti5O12/TiO2 composite tubes with regular structural imperfection for lithium ion storage. *Scientific reports,* 3**,** 1-5.

[49] Sanxi, L., Yu, H., Ling, Z., Xizhi, F., Binglin, Z. & Xueqiang, C. 2014. Synthesis and luminescence properties of CeF3: Tb3+ nanodisks via ultrasound assisted ionic liquid method. *Journal of Rare Earths,* 32**,** 508-513.

[50] Zhang, H., Liu, P., Li, F., Liu, H., Wang, Y., Zhang, S., Guo, M., Cheng, H. & Zhao, H. 2011. Facile fabrication of anatase TiO2 microspheres on solid substrates and surface crystal facet transformation from {001} to {101}. *Chemistry–A European Journal,* 17**,** 5949-5957.

[51] Li, J., Zhu, Y., Wang, L. & Cao, C. 2014. Lithium titanate epitaxial coating on spinel lithium manganese oxide surface for improving the performance of lithium storage capability. *ACS applied materials interfaces,* 6**,** 18742-18750.

[52] Chen, W., Jiang, H., Hu, Y., Dai, Y. & Li, C.J.C.C. 2014. Mesoporous single crystals Li 4 Ti 5 O 12 grown on rGO as high-rate anode materials for lithium-ion batteries. 50**,** 8856-8859.

[53] Wang, G., Zhu, X. & Yu, J. 2015. Bilayer hollow/spindle-like anatase TiO2 photoanode for high efficiency dye-sensitized solar cells. *Journal of Power Sources,* 278**,** 344-351.

[54] Gai, S., Yang, P., Li, X., Li, C., Wang, D., Dai, Y. & Lin, J. 2011. Monodisperse CeF 3, CeF 3: Tb 3+, and CeF 3: Tb 3+@ LaF 3 core/shell nanocrystals: synthesis and luminescent properties. *Journal of Materials Chemistry* 21**,** 14610-14615.

[55] Bon, C.Y., Isheunesu, P., Kim, S., Manasi, M., Kim, Y.I., Lee, Y.J. & Ko, J.M. 2018. High Capacity and Fast Charge-Discharge Li4Ti5O12 Nanoflakes/TiO2 Nanotubes Composite Anode Material for Lithium Ion Batteries. *Energy Technology,* 6**,** 2461-2468.

[56] Li, Y., Chen, Q., Meng, Q., Lei, S., Li, C., Li, X. & Ma, J. 2019. One-step synthesis of a nanosized cubic Li2TiO3-coated Br, C, and N Co-doped Li4Ti5O12 anode material for stable high-rate lithium-ion batteries. *ACS Applied Materials Interfaces,* 11**,** 25804-25816.

[57] Durdziński, P.T., Dunant, C.F., Haha, M.B. & Scrivener, K.L. 2015. A new quantification method based on SEM-EDS to assess fly ash composition and study the reaction of its individual components in hydrating cement paste. *Cement Concrete Research,* 73**,** 111-122.

[58] Ahn, D. & Xiao, X. 2011. Extended lithium titanate cycling potential window with near zero capacity loss. *Electrochemistry communications,* 13**,** 796-799.

[59] Liu, G., Liu, X., Wang, L., Ma, J., Xie, H., Ji, X., Guo, J. & Zhang, R. 2016. Hierarchical Li4Ti5O12-TiO2 microspheres assembled from nanoflakes with exposed Li4Ti5O12 (011) and anatase TiO2 (001) facets for high-performance lithium-ion batteries. *Electrochimica Acta,* 222**,** 1103-1111.

[60] Zhu, W., Yang, H., Zhang, W., Huang, H., Tao, X., Xia, Y., Gan, Y. & Guo, X. 2015. Synthesis and electrochemical performance of Li 4 Ti 5 O 12/TiO 2/C nanocrystallines for high-rate lithium ion batteries. *RSC Advances,* 5**,** 74774-74782.

[61] Bharti, B., Kumar, S., Lee, H.N. & Kumar, R. 2016. Formation of oxygen vacancies and Ti3+ state in TiO2 thin film and enhanced optical properties by air plasma treatment. *Scientific reports,* 6**,** 1-12.

[62] Lee, K.C., Chang-Jian, C.W., Ho, B.C., Ding, Y.R., Huang, J.H. & Hsiao, Y.S. 2019. Conductive PProDOT-Me2–capped Li4Ti5O12 microspheres with an optimized Ti3+/Ti4+ ratio for enhanced and rapid lithium-ion storage. *Ceramics International,* 45**,** 15252-15261.

[63] Xia, Q., Jabeen, N., Savilov, S.V., Aldoshin, S.M. & Xia, H. 2016. Black mesoporous Li 4 Ti 5 O 12− δ nanowall arrays with improved rate performance as advanced 3D anodes for microbatteries. *Journal of Materials Chemistry A,* 4**,** 17543-17551.

[64] Haruna, A.B. 2020. *Rational design synthesis and optimization of manganese-based cathode materials for lithium-ion batteries.*

[65] Annisa, N., Orlando, I. & Syahrial, A. Effect of Activated Carbon Addition on Electrochemical Performance of Li4Ti5O12/Nano Si Composite as Anode Material for LiB. IOP Conference Series: Materials Science and Engineering, 2019. IOP Publishing, 012057.

[66] Widmaier, M., Pfeifer, K., Bommer, L. & Presser, V. 2018. Valence-Tuned Lithium Titanate Nanopowder for High-Rate Electrochemical Energy Storage. *Batteries Supercaps,* 1**,** 11-26.

[67] Henderson, M.a.J.S.S. 1998. Evidence for bicarbonate formation on vacuum annealed TiO2 (110) resulting from a precursor-mediated interaction between CO2 and H2O. 400**,** 203-219.

[68] Su, Z., Liu, J., Li, M., Zhu, Y., Qian, S., Weng, M., Zheng, J., Zhong, Y., Pan, F. & Zhang, S. 2020. Defect engineering in titanium-based oxides for electrochemical energy storage devices. *Electrochemical Energy Reviews,* 3**,** 286-343.

[69] Ding, S., Jiang, Z., Gu, J., Zhang, H., Cai, J. & Wang, D. 2021. Carbon-coated lithium titanate: effect of carbon precursor addition processes on the electrochemical performance. *Frontiers of Chemical Science Engineering,* 15**,** 148-155.

[70] Xia, Q., Jabeen, N., Savilov, S.V., Aldoshin, S.M. & Xia, H.J.J.O.M.C.A. 2016. Black mesoporous Li 4 Ti 5 O 12− δ nanowall arrays with improved rate performance as advanced 3D anodes for microbatteries. 4**,** 17543-17551.

[71] Vijayakumar, A., Rajagopalan, R., Sushamakumariamma, A.S., Joseph, J., Ajay, A., Nair, S.V., Krishna, M.D. & Balakrishnan, A. 2015. Synergetic influence of ex-situ camphoric carbon

nano-grafting on lithium titanates for lithium ion capacitors. *Journal of Energy Chemistry*, 24**,** 337-345.

[72] Deng, W., Feng, X., Li, X., O'neill, S., Hu, L., Liu, L., Wong, W.Y., Hu, Y.Y. & Li, C.M.J.C.C. 2018. Improving the electrochemical performance of Li 4 Ti 5 O 12 anode by phosphorus reduction at a relatively low temperature. 54**,** 14120-14123.

Chapter 5

CeF_3-coated lithium titanate oxide ($Li_4Ti_5O_{12}$) anode for lithium-ion capacitors

5.1 Introduction

The speedy evolution of consumer electronic and electric vehicle industries introduces the need for energy storage devices that simultaneously have high energy and power densities. Lithium-ion batteries (LIBs) constantly capture researchers' enthusiasm on the type of storage technologies to be implemented on the booming applications with these requirements, but the required high-power component of LIBs storage systems is challenging to achieve because of the sluggish dynamic behaviour and unstable interface of the Faradaic energy storage mechanism [1]. This challenge of LIBs with rectified by the high power density of electric double-layer capacitors (EDLCs), which unfortunately comes with lower energy density than LIBs [2].

The combination of an anode electrode with lithium insertion/desertion capability and a cathode electrode consisting of surface adsorption/desorption storage mechanism allow the construction of hybrid capacitors called lithium-ion capacitors (LICs) [3]. With this merge of mechanisms, LICs can optimize the energy and power output more than most of their energy storage counterparts. The battery-type electrode usually employed as anodes in LICs offer high energy density and the capacitive cathode has the high power density [4]. Amongst anode materials, $Li_4Ti_5O_{12}$ (LTO) has gained a lot of traction as a favourable anode material due to its negligible structural change during lithium-ion insertion/desertion that give rise to higher reversibility, cycle life and safety [5].

Another desirable property of LTO in the LICs is its high-rate capability which originates from its three-dimensional lithium insertion path [6]. The low electronic conductivity and diffusion coefficient halt this material from being used in commercial applications [7]. A challenge in LICs is to balance the fast charge/discharge capability of the capacitive cathode with the sluggish kinetics of LTO. Herein we attempt to modify the properties of LTO as a better anode material for LIC by applying a layer of CeF_3 coating on a commercial LTO. This choice was motivated by the high ionic conductivity of CeF_3 and chemically inertness of CeF_3 which could prevent the possible gas evolutions that LTO usually undergo in energy storage systems (ESSs) [8].

Our study on the coated LTO (LTO-CeF_3) in defect-engineered LTO materials for Li-ion batteries (Chapter 4) indicated that the coated LTO had improved electrochemical performance revolving around the mixed state of the Ti^{3+} and T^{4+} promoted by the co-doping of some of the CeF_3 into the LTO structure. The detailed structural analysis of the pristine LTO (LTO-p) and LTO-CeF_3 can be found in chapter 4. Therefore, in this chapter the electrochemistry of these materials will solely be presented.

The results are presented with one subsection showing the comparison of half-cells of the two materials with the one having a better electrochemical performance being utilized in the LIC full cell. The choice of the material here is guided by how each material performed in the earlier LIBs study reported in chapter 4. This is because the half cells employed in the present chapter are equivalent to the LIB cells of chapter 4. Under the guidance of mass balancing, the chosen material is then used as an anode material and paired with carbon black (AB) cathode to assemble a LIC device.

5.2 Results and discussion

5.2.1 Half-cell electrochemistry comparison

5.2.1.1 Cyclic voltammetry (CV)

Figure 5.1 shows cycling voltammograms of (a) LTO-p and (b) LTO-CeF_3 carried at room temperature on several scan rates using a voltage window of 1.0-2.5 V. Pair of reversible redox peaks is detected in all the CV curves, indicating lithiation/delithiation of LTO [9]. Figure 5.1 (c) show comparison of LTO-p and LTO-CeF_3 CV curves run at 2.5 mVs^{-1} scan rate. LTO-p demonstrates high current response than LTO-CeF_3. To extract further insights from the CV comparison, specific capacity was calculated from the CV curves at 2.5 mVs^{-1}. LTO-CeF_3 had a specific capacity of 186 $mAhg^{-1}$ while LTO-p gave a capacity of 184 $mAhg^{-1}$ even when the active mass of the LTO-CeF_3 was twice the one of LTO-p.

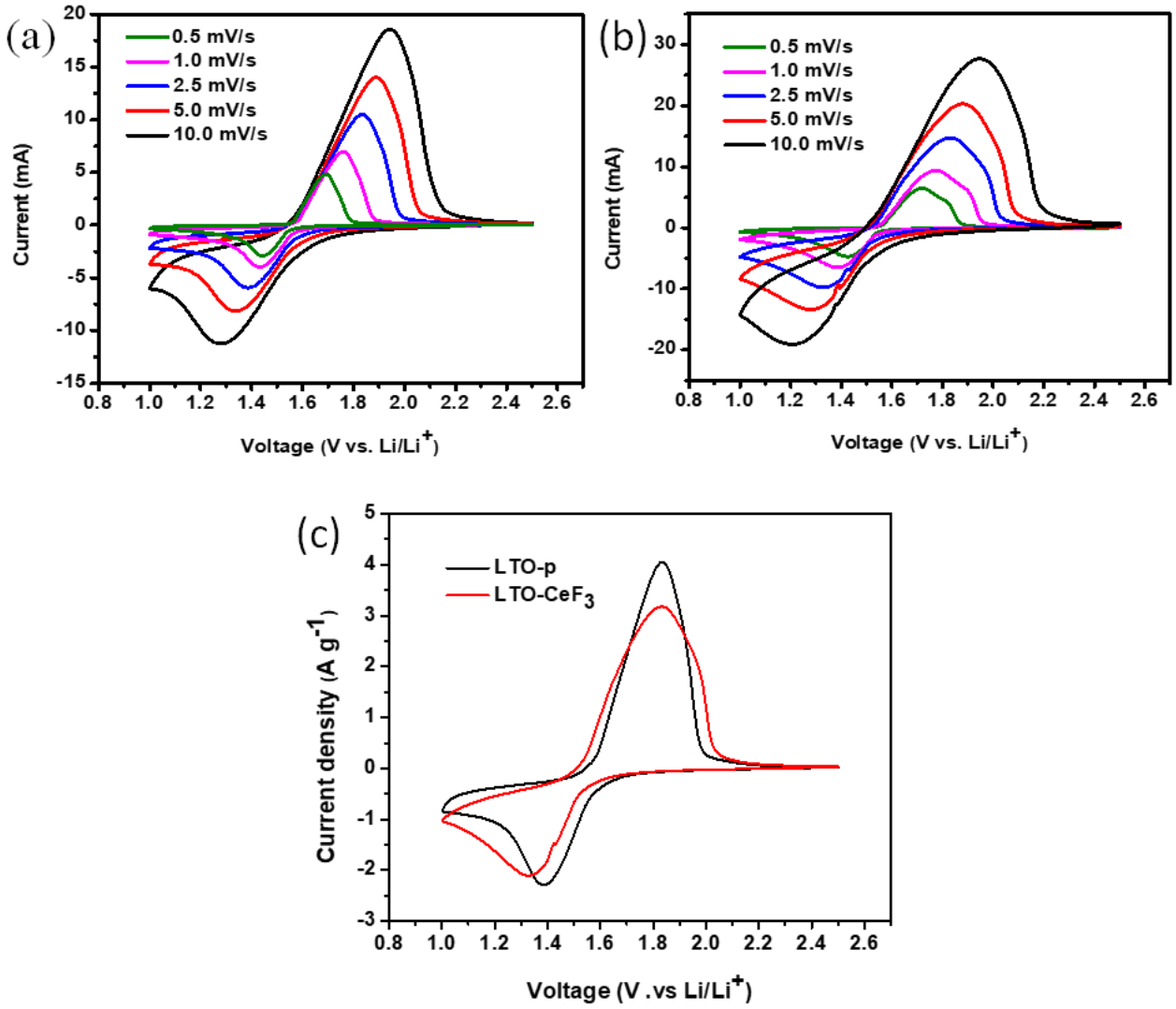


Figure 5.1: Half-cell CV plots at numerous scan rates: (a) LTO-p, (b) LTO-CeF_3, and (c) comparison of LTO-P and LTO-CeF_3 at 2.5 mVs^{-1}.

5.2.1.2 Galvanostatic charge-discharge (GCD)

Charge-discharge profiles of LTO-p and LTO-CeF_3 were explored at various current densities and are displayed in Figure 5.2 (a) and (b), respectively. The charge-discharge in this case represents lithiation/delithiation mechanism of Li^+ into the LTO materials at 1.0-3.0 V range [10]. The charge-discharge profile indicates that the charging-discharge time of each half-cell decreased with increasing current density during measurements. By comparing the materials at 1 Ag^{-1} as shown in Figure 5.2 (C), LTO-p possessed high specific capacity (103.3 $mAhg^{-1}$) during charging process and lower discharge specific capacity (84.2 $mAhg^{-1}$) when compared to LTO-CeF_3, which recorded the same specific capacity of 93.3 $mAhg^{-1}$ for both processes. This hint on LTO-CeF_3 having higher coulombic efficiency than LTO-p. The improved electrochemical activities could be ascribed to the layer of CeF_3 which has high ionic conductivity.

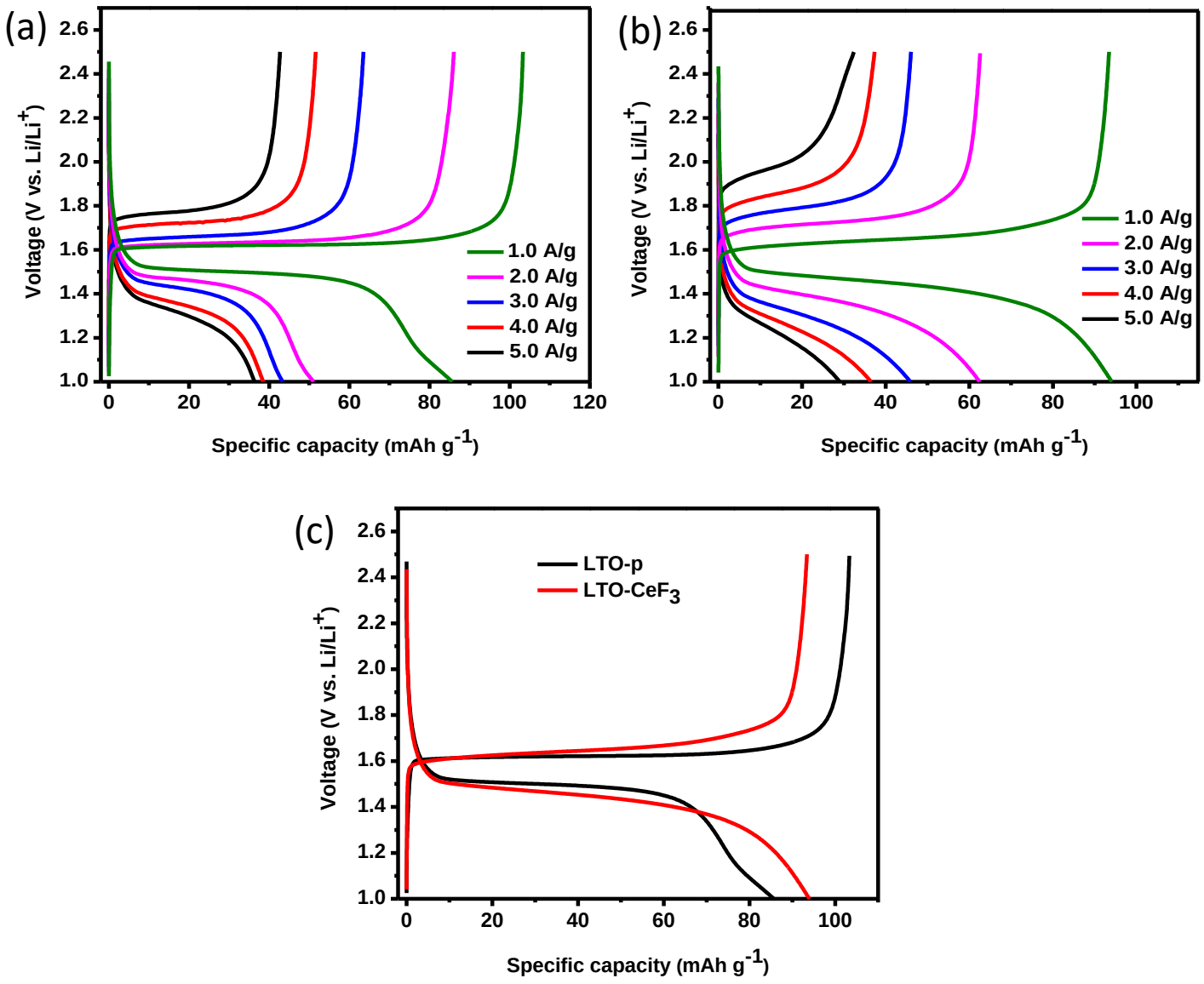


Figure 5.2: Charge-discharge plots of (a) LTO-p, (b) LTO-CeF_3 at several current densities, (c) LTO-p and LTO-CeF_3 capacities comparison at 1 Ag^{-1}.

5.2.1.3 Specific capacity and Coulombic efficiency

Specific capacity plots of LTO-p and LTO-CeF_3 on current density range 1-5 Ag^{-1} are shown on Figure 5.3 (a). LTO-CeF_3 exhibits high discharge capacity than LTO-p current densities 1.0, 2.0 and 3.0 Ag^{-1}. At 4.0 Ag^{-1}, the materials have the same specific capacity and LTO-p has a higher specific capacity at 5.0 Ag^{-1}. Coulombic efficiencies of the materials from 0 to 250 cycles are shown in Figure 5.3 (b) with LTO-p giving poor coulombic efficiency in the first 70 cycles and stabilizing after these cycles. This may occurred because of activation of the LTO-p electrode [11]. LTO-CeF_3 has better coulombic efficiency throughout the tested cycles.

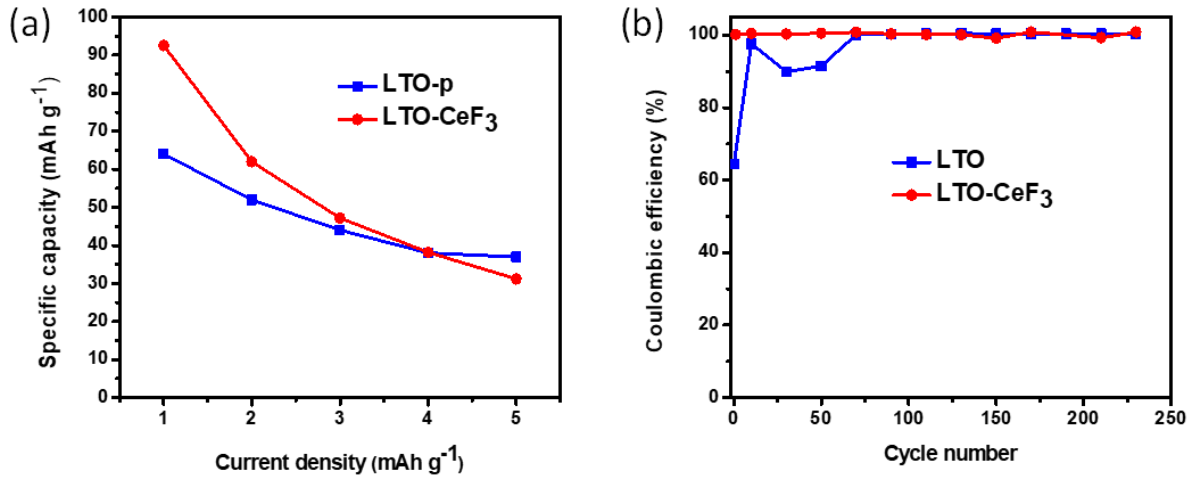


Figure 5.3: (a) Specific capacity at several current densities, (b) Coulombic efficiency of LTO-p and LTO-CeF_3.

5.2.1.4 Choosing the anode active material

With the electrochemical performance outline in the subsections above, LTO-CeF_3 has better performance than LTO-p, with better charge-discharge profile, high specific capacity and coulombic efficiency. These enhanced performance could be linked to the high ionic conductivity of CeF_3, the protective layer CeF_3 offers and the co-doping that occurred during synthesis (details found in chapter 4). On the impedance studies of these materials in LIBs, it was found that before cycling, LTO-CeF_3 had better charge transfer resistance R_{ct} and after cycling for 1000 cycles, LTO-p was found to have lower R_{ct} which is possibly because of the SEI formation that LTO-CeF_3 experienced on the EIS study covered in chapter 4. Based on the above electrochemical results, LTO-CeF_3 was chosen as an anode material for the LIC

5.2.2 Full cell electrochemistry

5.2.2.1 Cyclic voltammetry of LTO-CeF_3 and carbon black super C45

Figure 5.4 shows CV curves of LTO-CeF_3 and carbon black super C45. The CV analyses was conducted to obtain the potential window where each material was electroactive. LTO-CeF_3 was found to operate at a 1.0 – 2.5 V window with asymmetric (battery-type) anode and cathode peaks, respectively. The peaks revealed the lithium insertion and extraction on the material's bulk structure. The operating potential window of carbon black was discovered at 3.0 – 4.2 V, exhibiting quasi-rectangular shapes which is ascribed to the electrical double-layer (EDL) intrinsic property of carbon materials [12].

The measured electrochemical performance of carbon black (cathode) was used to calculate the mass ratio against the LTO anode, using equation 5.1[13]

$$\frac{m^+}{m^-} = \frac{c^-}{c^+} + \frac{\Delta V^-}{\Delta V^+} \tag{5.1}$$

where m^+, ΔV^+, and c^+ are the mass of the active material, potential window, and specific capacity of the cathode, respectively. The m^-, ΔV^-, and c^- indicate the mass of the active material, potential window, and specific capacity of the anode. The cathode (carbon black) to anode (LTO) mass ratio was 3:1.

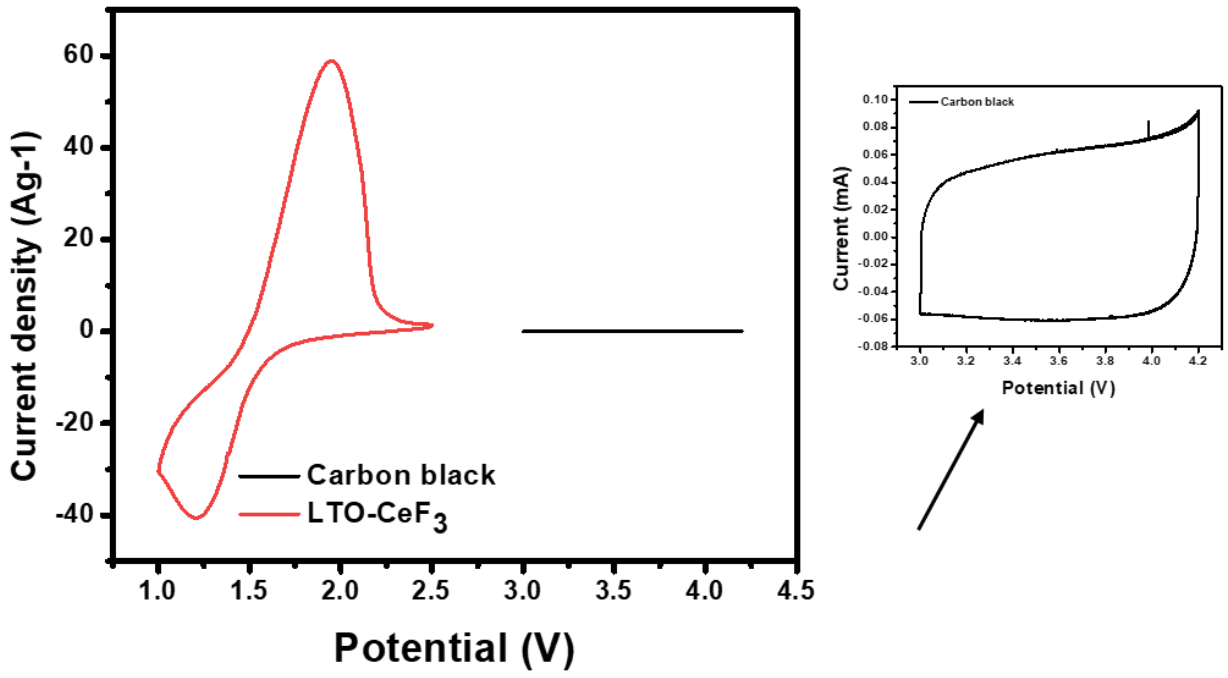


Figure 5.4: CV plots of carbon black and LTO-CeF_3.

5.2.2.2 Cyclic voltammetry (CV) of LTO-CeF_3//CB

Figure 5.5 presents CV plots of LTO-CeF_3//CB full cell along the range 1.0-3.0 V at various scan rates at room temperature. The mechanism behind the voltammogram has Li^+ ion insertion/desertion into the LTO-CeF_3 structure at the anode and PF_6^- ion adsorbed/desorbed at the CB surface [14]. This means that the redox reaction of the LIC is limited by the potential of lithiation/delithiation in the LTO-CeF_3 electrode. From the CV curves, it is observed that the current response increased with escalated scan rates. And this may be as a result of fast ions that reached the core structure of the electrode at low scan rates [15].

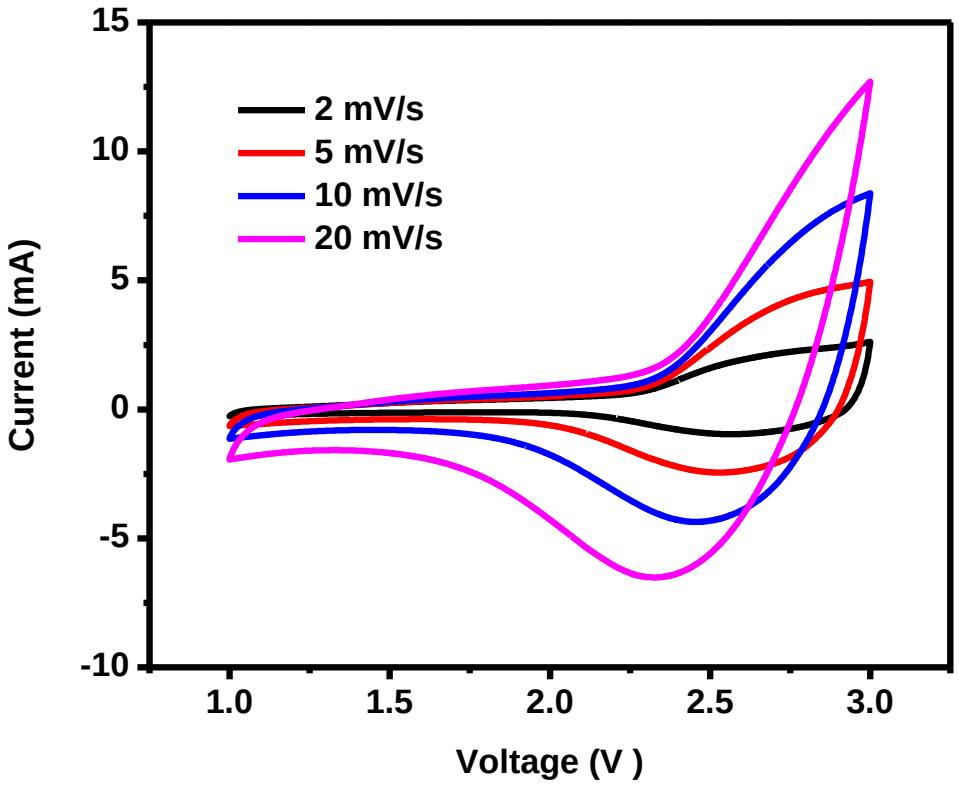


Figure 5.5: CV curves of LTO-CeF_3// CB full cell at various scan rates.

5.2.2.3 Galvanostatic charge-discharge (GCD) of LTO-CeF_3//CB

Charge-discharge profiles of CB and LTO-CeF_3 are presented in Figure 5.6 for 1.0, 1.5, 2.5 and 5.0 Ag^{-1} current densities, at 1.0 - 3.0 V potential. Upon charging, the electrolyte's Li^+ ions migrate to intercalate into the LTO-CeF_3 electrode and the PF_6^- ions present in the solution are adsorbed at the counter electrode (CB) surface [16]. During discharge, the ions migrate back to the electrolyte. Therefore, the voltage profile of charge-discharge can be used to check certain characteristics of reaction from within the cell.

From Figure 5.6 (a), a gradual sloping profile was observed at 1.0 - 2.7 V potential range (which decreased with a decline in current density) for charge and 1.0-2.3 for discharge. There is also a sharply sloped profile on 2.7-3.0 V and 2.3-3.0 V ascribed to charge and discharge, respectively. The increase in applied current density tends to lower the discharging time. The discharge rate performance of LIC full cell can be seen in Figure 5.6 (b). The cell delivered discharge capacities of 54.11, 50.38, 44.13 and 28.32 $mAhg^{-1}$ at 1.0, 1.5, 2.5 and 5.0 Ag^{-1}, respectively. All the GCD curves possessed flat plateau (~ 1.55 V), which is linked to two-phase lithiation/delithiation mechanism to transform $Li_4Ti_5O_{12}$ to $Li_7Ti_5O_{12}$ [17].

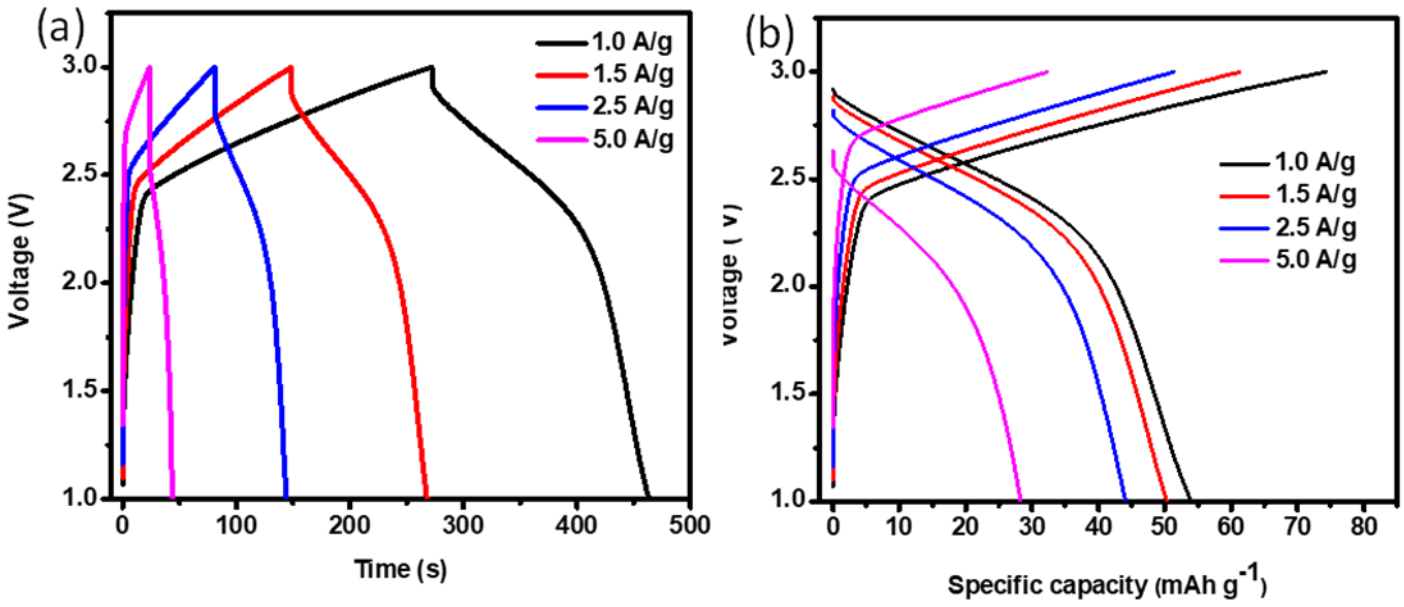


Figure 5.6: Charge-discharge of LTO-CeF_3//CB full cell at several current densities.

5.2.2.4 Specific capacitance

Figure 5.7 show specific capacitances corresponding to the charge-discharge recorded at current densities of 1.0 to 5 Ag^{-1}. The full cell specific capacitance is extracted from the charge/discharge plots using equation 5.2 below [18]:

$$C\ (F\ g^{-1}) = \frac{I\Delta t}{m\Delta V} \qquad (5.2)$$

where I (A) is the applied current, t (s) is the discharge time, m (g) is the total active mass of electrodes, and ΔV is the discharge voltage. The specific capacitance decreased from 96.3 to 55.4 Fg^{-1} when current density was increased from 1.0 to 5.0 Ag^{-1}. The cell retained 57.5% of its initial capacitance. The cell was further assessed for cycling performance as shown in Figure 5.8 at 5 Ag^{-1} and 1.0 – 3.0 V potential range. The cell had an initial capacitance of 63.1 Fg^{-1}, obtained 60.0,

58.9,58.4 and 57.4 Fg^{-1} at cycle 20, 40, 80 and 100, respectively. The cell maintained only 91.0% of its initial capacitance at cycle 100. The device achieved this with a coulombic efficiency of 92.2 %.

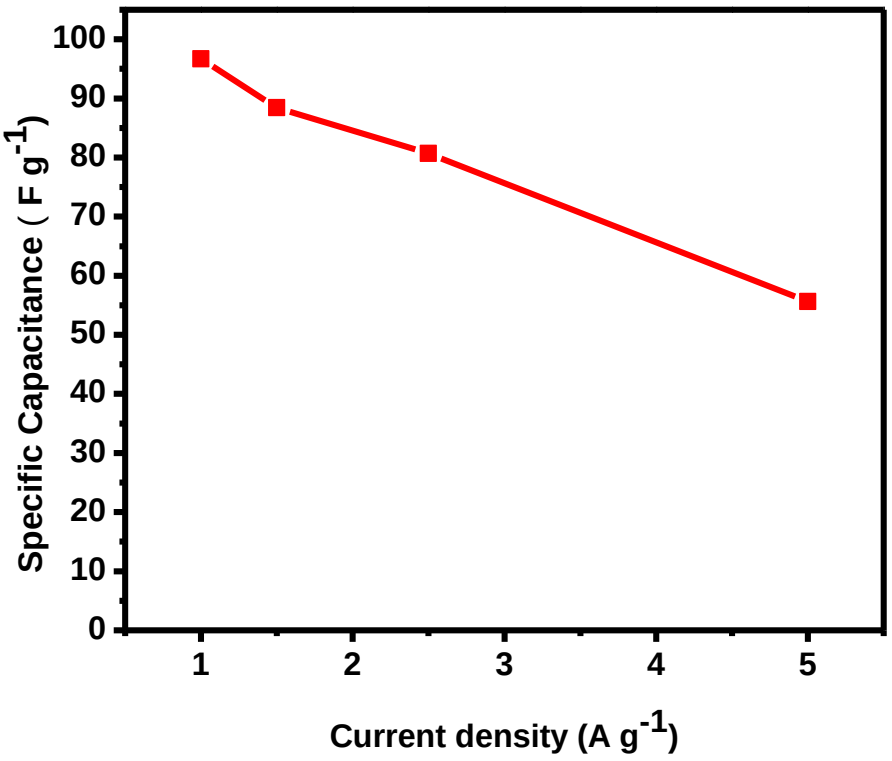


Figure 5.7: Specific capacitance at various current density.

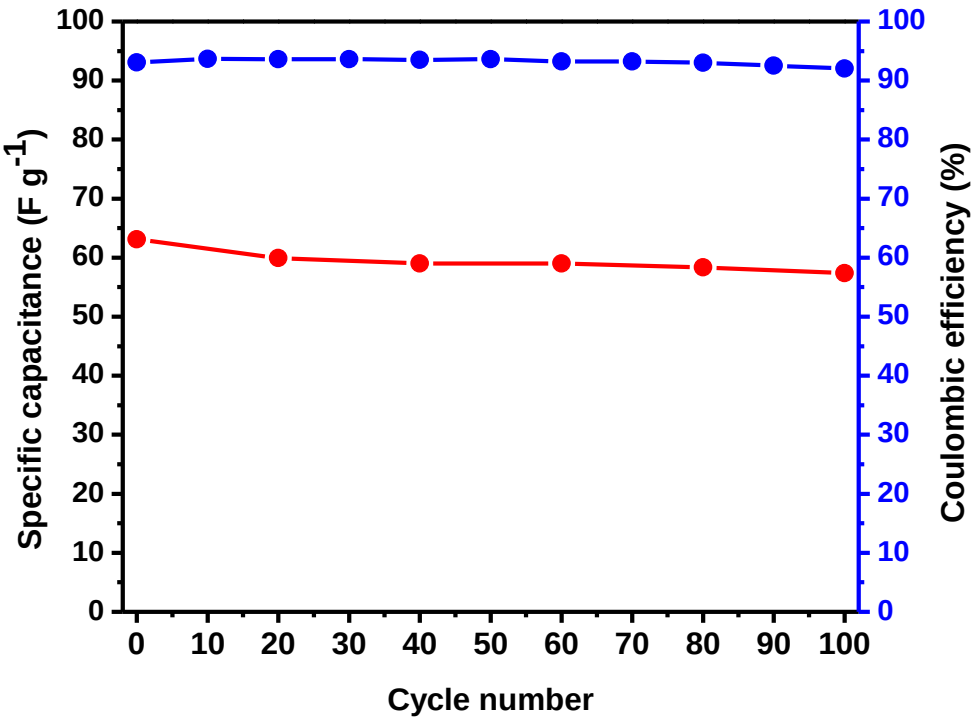


Figure 5.8: Specific capacitance and coulombic efficiency observed on 100 cycles.

5.2.2.5 Ragone plot

The relationship between the energy density (E, Wh Kg^{-1}) and power density (P, W kg^{-1}) in the under studied full LIC cell consisting of LTO anode and AB cathode, in relation to other full cells from literature, is presented in the Ragone plot in Figure 5.9. This relationship was determined from discharge curves using equation 5.3 – 5.5 [13]:

$$E = \Delta V \times \frac{I}{m} \times t \quad (5.3)$$

$$P = \Delta V \times \frac{I}{m} \quad (5.4)$$

$$\Delta V = \frac{E_{max}+E_{min}}{2} \quad (5.5)$$

where I (A) is the applied current, m (g) is the total active mass of the cathode and anode materials, t (s) is the discharge time, E_{max} and E_{min} (V) are the initial and final discharge times. The maximum energy density delivered by the cell is 107.4 Wh kg^{-1} at a power density of 2000 W kg^{-1} and it could deliver a power density of 10 000 W kg^{-1} with energy density 61.8 Wh Kg^{-1}. The energy and power density of this cell outperforms other reported LIC systems like as CNT@ *p* LTO//GF (101.8 Wh kg^{-1} and 436.1 W kg^{-1}) [19], LTO-AC//AC (38 Wh kg^{-1} and 7964 W kg^{-1}) [20], LTO-NR/CNT/rGO// AC/CNT/rGO (67 Wh kg^{-1} and 1589 W kg^{-1}) [21], CNTs/LTO//AC (35 Wh kg^{-1} and 7434 W kg^{-1}) [22], and LTO/Graphene//AC (44.0 Wh kg^{-1} and 7200 W kg^{-1}) [6].

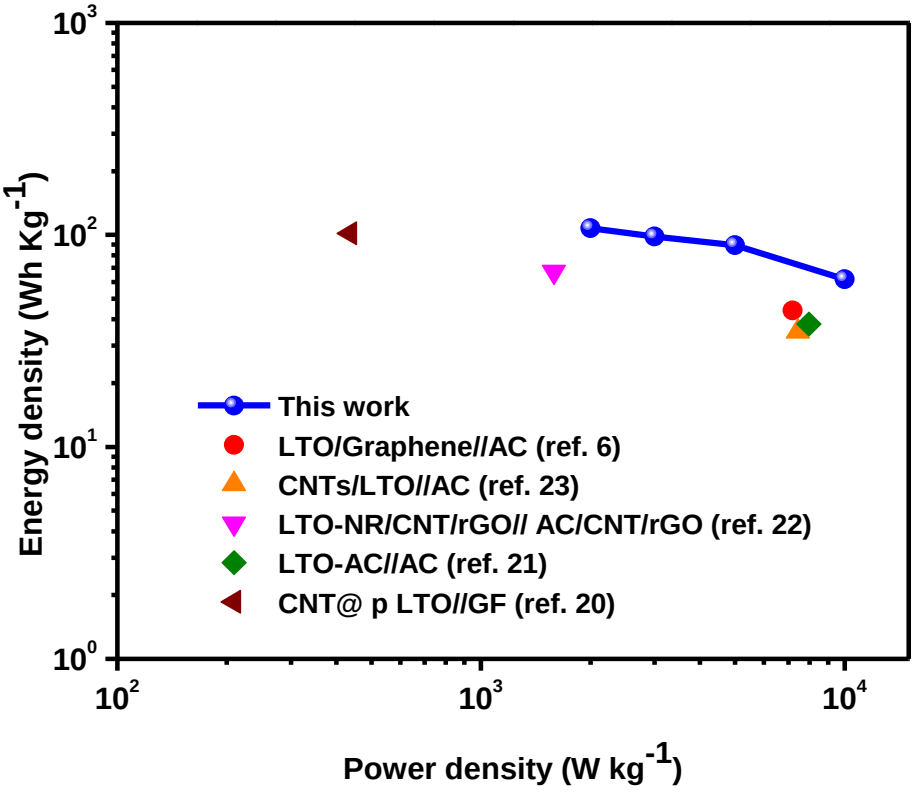


Figure 5.9: Ragone plot for LIC full cell made up of LTO anode and CB cathode, compared with the literature.

5.3 References

[1] Liu, Y., Wang, W., Chen, J., Li, X., Cheng, Q. & Wang, G.J.J.O.E.C. 2020. Fabrication of porous lithium titanate self-supporting anode for high performance lithium-ion capacitor. 50**,** 344-350.

[2] Morimoto, T., Hiratsuka, K., Sanada, Y. & Kurihara, K.J.J.O.P.S. 1996. Electric double-layer capacitor using organic electrolyte. 60**,** 239-247.

[3] Chen, W., Xu, C., Chen, M., Jiang, K. & Wang, K. 2021. A novel fusion model based online state of power estimation method for lithium-ion capacitor. *Journal of Energy Storage,* 36**,** 102387.

[4] Li, B., Dai, F., Xiao, Q., Yang, L., Shen, J., Zhang, C. & Cai, M. 2016. Activated carbon from biomass transfer for high-energy density lithium-ion supercapacitors. *Advanced Energy Materials,* 6**,** 1600802.

[5] Zheng, J., Xing, G., Zhang, L., Lu, Y., Jin, L. & Zheng, J.P. 2021. A Minireview on High-Performance Anodes for Lithium-Ion Capacitors. *Batteries & Supercaps,* 4**,** 897-908.

[6] Zhang, X., Lu, C., Peng, H., Wang, X., Zhang, Y., Wang, Z., Zhong, Y. & Wang, G. 2017. Influence of sintering temperature and graphene additives on the electrochemical performance of porous Li4Ti5O12 anode for lithium ion capacitor. *Electrochimica Acta,* 246**,** 1237-1247.

[7] Zhang, Z., Deng, X., Sunarso, J., Cai, R., Chu, S., Miao, J., Zhou, W. & Shao, Z. 2017. Two-step fabrication of Li4Ti5O12-coated carbon nanofibers as a flexible film electrode for high-power lithium-ion batteries. *ChemElectroChem,* 4**,** 2286-2292.

[8] Xie, Y., Gao, D., Zhang, L., Chen, J., Cheng, S. & Xiang, H. 2016. CeF3-modified LiNi1/3Co1/3Mn1/3O2 cathode material for high-voltage Li-ion batteries. *Ceramics International,* 42**,** 14587-14594.

[9] Lu, C., Wang, X., Zhang, X., Peng, H., Zhang, Y., Wang, G., Wang, Z., Cao, G., Umirov, N. & Bakenov, Z. 2017. Effect of graphene nanosheets on electrochemical performance of Li4Ti5O12 in lithium-ion capacitors. *Ceramics International,* 43**,** 6554-6562.

[10] Han, C., He, Y.B., Wang, S., Wang, C., Du, H., Qin, X., Lin, Z., Li, B. & Kang, F. 2016. Large polarization of Li4Ti5O12 lithiated to 0 V at large charge/discharge rates. *ACS Applied Materials Interfaces,* 8**,** 18788-18796.

[11] Ding, X., Zou, B., Li, Y., He, X., Liao, J., Tang, Z., Shao, Y. & Chen, C. 2017. A novel lithium-ion battery comprising Li-rich@ Cr2O5 composite cathode and Li4Ti5O12 anode with controllable coulombic efficiency. *Science China Materials,* 60**,** 839-848.

[12] Li, Y., Shen, J., Li, J., Sun, X., Shen, J., Han, W. & Wang, L. 2017. A protic salt-derived porous carbon for efficient capacitive deionization: Balance between porous structure and chemical composition. *Carbon,* 116**,** 21-32.

[13] Mofokeng, T.P., Ipadeola, A.K., Tetana, Z.N. & Ozoemena, K.I. 2020. Defect-engineered nanostructured Ni/MOF-derived carbons for an efficient aqueous battery-type energy storage device. *ACS omega,* 5**,** 20461-20472.

[14] Sohib, A., Subhan, A., Widayatno, W.B., Priyono, S., Hudaya, C., Nuroniah, I., Sari, S.N. & Prihandoko, B. 2020. Electrochemical Performance of Li4-xTi5CuxO12 for Lithium Ion Capacitor Applications. *Widyariset,* 6**,** 43-50.

[15] Zhao, E., Liu, X., Hu, Z., Sun, L. & Xiao, X. 2015. Facile synthesis and enhanced electrochemical performances of Li2TiO3-coated lithium-rich layered Li1. 13Ni0. 30Mn0. 57O2 cathode materials for lithium-ion batteries. *Journal of Power Sources,* 294**,** 141-149.

[16] Madabattula, G., Wu, B., Marinescu, M. & Offer, G.J.J.O.T.E.S. 2019. How to design lithium ion capacitors: modelling, mass ratio of electrodes and pre-lithiation. 167**,** 013527.

[17] Wagemaker, M., Simon, D.R., Kelder, E.M., Schoonman, J., Ringpfeil, C., Haake, U., Lützenkirchen-Hecht, D., Frahm, R. & Mulder, F.M.J.a.M. 2006. A kinetic two-phase and equilibrium solid solution in spinel Li4+ xTi5O12. 18**,** 3169-3173.

[18] Lin, Y.T., Chang-Jian, C.W., Hsieh, T.H., Huang, J.H., Weng, H.C., Hsiao, Y.S., Syu, W.L. & Chen, C.P.J.a.S.S. 2021. High-performance Li-ion capacitor constructed from biomass-derived porous carbon and high-rate Li4Ti5O12. 543**,** 148717.

[19] Liu, Y., Wang, W., Chen, J., Li, X., Cheng, Q. & Wang, G. 2020. Fabrication of porous lithium titanate self-supporting anode for high performance lithium-ion capacitor. *Journal of Energy Chemistry,* 50**,** 344-350.

[20] Jiang, C., Zhao, J., Wu, H., Zou, Z. & Huang, R. 2018. Li4Ti5O12/activated-carbon hybrid anodes prepared by in situ copolymerization and post-CO2 activation for high power Li-ion capacitors. *Journal of Power Sources*, 401**,** 135-141.

[21] Li, X., Tang, Y., Song, J., Wang, M., Huang, Y., Liu, L. & Zheng, J. 2019. Self-supporting lithium titanate nanorod/carbon nanotube/reduced graphene oxide flexible electrode for high performance hybrid lithium-ion capacitor. *Journal of Alloys Compounds,* 790**,** 1157-1166.

[22] Ye, Z., Zhong, F., Chen, Y., Zou, Z. & Jiang, C.J.C.I. 2022. Unique CNTs-chained Li4Ti5O12 nanoparticles as excellent high rate anode materials for Li-ion capacitors.

Chapter 6
General conclusion

6.1 Conclusion

In this work, we have achieved modification of a commercial LTO with CeF_3 and microwave irradiation. The structural analysis revealed the existence of CeF_3 on the surface of the coated materials via TEM analysis. Further analysis of the modified materials (when compared to LTO-p) revealed (111) plane peak shift on XRD patterns which may have been caused by co-doping of a portion of the CeF_3 layer into the LTO structure during annealing on the CeF_3 coated materials. The co-doping might have led to anatase TiO_2 observed on the CeF_3 modified materials. The shifting of these peaks on all the materials may have been caused by oxygen vacancies created by heat treatment applied to the materials, and the observed mixed state of Ti (Ti^{3+} /Ti^{4+}) on the modified materials may have resulted during this process. Since the presence of Ti^{3+} on spinel LTO increased its conductivity, better electrochemical performance was expected from the modified materials. The oxygen vacancies might have slightly altered the structure of LTO during the microwave irradiation and caused the slight increase in mass loss experienced by the microwave materials under the TGA studies.

Each material was utilized as an active anode paired with a lithium foil cathode for testing their eligibility in lithium-ion batteries. CeF_3 coated and the microwave modified materials possessed a high current response and high specific capacity than the LTO-p, which may have been a result of the high ionic conductivity of CeF_3 and/or because of the presence of Ti^{3+} on these materials. These materials had excellent rate capabilities than LTO-p. They also produced superior capacity

retention (more than 98% of their initial capacity) and excellent coulombic efficiency when charge/discharge tests were carried out for 100 cycles at 1C. By further investigating the electrochemistry of the materials at a high rate (5C) for many cycles (1000), the modified materials experienced a huge capacity degradation after 500 cycles; only LTO-CeF_3-mw achieved a superior capacity retention of 167.34 mAh g^{-1} at both 500 and 1000 cycles. LTO-CeF_3-mw had the best overall electrochemical performance and highest specific capacity, which resulted from the coated CeF_3, the microwave irradiation effect and highly observed grain boundaries on the HRTEM. These results proved that the combination of CeF_3 modification and microwave irradiation could be an effective method for improving the electrochemistry of LTO.

Anode materials for lithium-ion capacitor were also explored in this work. By comparing the three-electrode system of LTO-p and LTO-CeF_3, LTO-CeF_3 was chosen as a viable anode material for LIC. The decision was due to high specific capacity, better coulombic efficiency, and charge/discharge profile of this material demonstrated. Then the material was paired with acetylene black cathode to assemble a full LIC cell. The assembled device delivered a maximum energy density of 107.4 Wh kg^{-1} at a power density of 2000 W kg^{-1} and output energy density of 61.8 Wh Kg^{-1} at a maximum power density of 10 000 W kg^{-1}. Compared with some of the recent LICs employing an LTO anode, our device had higher power and energy densities.

6.2 Future work

Additional research is essential to further investigate the properties of the materials. These future investigations should encompass:

- Application of Rietveld refinement to analyze the (111) peak shift observed in the XRD data, providing detailed information, and substantiating the changes to the lattice parameters following modifications (such as coating and microwave irradiation).
- Utilization of TEM and HRTEM techniques to conduct a more in-depth study of the LTO-md and LTO-CeF_3 materials, enabling a finer examination of their structural characteristics.
- Calculations of the diffusion coefficient and electronic conductivity of the materials to better understand the extent to which the modifications have enhanced the movement of Li-ions and electrons within the LTO materials.
- Electrochemical testing of all the materials as anode active materials in the LIC (Lithium-Ion Capacitor) system to assess their performance.

These additional research efforts will contribute to a more comprehensive understanding of the materials and their potential applications.